Resonant Waveguide Gratings for Color-Selective Diffraction

Thèse N° 7527

Giorgio QUARANTA

2019

EPFL
ÉCOLE POLYTECHNIQUE
FÉDÉRALE DE LAUSANNE

There are two ways of spreading light:
to be the candle or the mirror that reflects it.
— Edith Wharton, 1902

To Chiara

Acknowledgements

First, I would like to express my sincere gratitude to Guillaume Basset, Dr. Sören Fricke followed by Dr. Marc Schnieper for welcoming me as a PhD candidate at CSEM in Muttenz. I especially thank Guillaume for introducing me to the application driven research, for his thesis contributions and for numerous and fruitful discussions, in particular regarding the fascinating field of resonant waveguide gratings. Sören has been invaluable for me for his enthusiasm, his confidence in me and his advice which allowed me to grow both professionally and as a person. I also thank Marc for inspiring discussions and his appreciations of my work which have been motivating for me until the end. Furthermore, I would like to thank Dr. Christian Bosshard for this great opportunity to carry out my thesis in the company and for his support. All of you have made this thesis possible.

I would also like to thank my thesis directors, Dr. Benjamin Gallinet and Prof. Olivier Martin, for their great supervision and guidance. Benjamin has shared essential technical advice with me, in particular concerning plasmonics and Fano resonances. I have also learned a lot from him about how to write scientific papers and to properly manage the planning of projects. Thank you for dedicating your time and patience to this work. Olivier has been for me an exceptional source of inspiring ideas and interesting topics and he helped to find the best directions for my research. Thank you for your work and support, for pushing me to do better and better and for your sensitivity.

Many thanks are due to the members of the thesis committee, Prof. Olivier Parriaux, Prof. Martina Gerken, Prof. Hans Peter Herzig and Prof. Christophe Moser for their time and involvement. Your questions and remarks have allowed me to improve the thesis and have been important food for thought.

To no lesser extent, I would strongly like to thank Dr. Zdenek Benes, for having initiated me into the electron beam lithography and for our fruitful collaboration. Thanks also to Rémy Juttin and Guy Clerc for all the times I had to make new recipes and settings for the electron beam evaporator machine. Thank you, without the three of you the fabrication would have not been possible.

In addition, I would like to thank the group of NAM EPFL, in particular Debdatta Ray, Dr. Christian Santschi, Sebastian Mader, Hsiang-Chu Wang and Dr. Kuang-Yu Yang. Thank you for the interesting and enriching talks of our weekly meetings!

Acknowledgements

Abstract

Resonant waveguide gratings (RWGs), also known as guided mode resonant (GMR) gratings or waveguide-mode resonant gratings, are dielectric structures where these resonant diffractive elements benefit from lateral leaky guided modes and can operate from UV to microwave frequencies, in many different configurations. Some of the guided light is diffracted out of the guide while propagating, coupled back to radiation and interferes with the non-coupled reflected or transmitted waves. This leads to a very high reflection or transmission, giving rise to a Fano or Lorentzian-like lineshape profile at the zeroth order. RWGs are intrinsically very sensitive to angle and wavelength variations, being therefore effective filtering structures, especially for collimated light. Thanks to their high degree of optical tunability (wavelength, phase, polarization, intensity) and the variety of fabrication processes and materials available, RWGs have been implemented in a broad scope of applications in research and industry, such as optical security features, refractive index and fluorescence biosensors, spectrometers and optical couplers.

This thesis describes the development and realization of color-selective diffraction devices using RWGs. The properties of paired impedance matched RWGs with finite size and different grating periods, but sharing the same substrate and coated waveguide, are first investigated. In particular, a specific wavelength range is in-coupled inside the waveguide by the first grating from a white incident light beam, and out-coupled from the second grating at a different angle. Periodic arrays of such paired RWGs allow achieving color-selective diffraction. Moreover, specific design methods based on confocal prolate spheroids are derived and used to generate surfaces with different grating periods and orientations, which can filter a specific spectral portion of a point source and to redirect and focus it to another point in space, viz. the observation point. This patterning is particularly beneficial in applications where light re-focusing is required, such as optical security or optical combiners for near-eye displays. Realizations as optical security labels through smartphone-based authentication are presented and discussed.

Since the fabrication of such devices is extremely demanding, a fabrication method is developed to reduce the exposure time for the electron beam lithography. This method is beneficial to efficiently fabricate gratings with different periods and oriented at different angles. In particular, a pre-fracturing of the grating lines in one or more smaller stripes, depending on the grating period, is first implemented, followed by the fracturing using a beam step size smaller than the beam diameter. This fracturing technique enables the exposure of complex surfaces with a larger electron beam than with standard grating fracturing approaches in less

than 5 hours per cm^2, while a conventional electron beam writing would have taken more than 20 hours per cm^2 to achieve the same quality.

In the last part, optical structures comprising a metallic layer and a dielectric layer on a corrugated glass substrate are described. In essence, the hybridization of plasmon and waveguide modes is studied and used to design a color-selective optical coupler where the hybridized modes are leaking into the substrate at the first diffraction order and are coupled as guided mode. Such coupler may be used as dispersive element when the white light source is divergent allowing, for example, the realization of inexpensive, compact and robust spectrometers.

Keywords: optics, nanophotonics, resonant waveguide grating, coupled-mode resonant grating, diffraction gratings, color-selective diffraction, beam redirection, refocusing, focusing, visible light, white light source, ellipsoidal mirror, up-scalable fabrication, nanoimprint lithography, electron beam lithography, smartphone authentication, optical document security, optical combiner, near-eye displays, spectrometer, optical coupler.

Sommario

I reticoli di guide d'onda risonanti sono strutture dielettriche in cui gli elementi diffrattivi di risonanza beneficiano dei modi laterali guidati con perdite e possono operare dalle frequenze UV alle microonde in molteplici configurazioni. Una parte della luce guidata è diffratta in radiazione al di fuori della guida d'onda durante la propagazione e interferisce con le onde riflesse o trasmesse non guidate. Questo produce una riflessione o una trasmissione molto alta, dando origine a un profilo di tipo Fano o Lorentz nell'ordine zero di diffrazione. I reticoli di guide d'onda risonanti sono intrinsecamente molto sensibili alle variazioni angolari o di lunghezza d'onda, essendo pertanto strutture efficaci nel filtrare, specialmente utilizzando della luce collimata. Grazie al loro alto grado di guidabilità (in termini di fase, polarizzazione ed intensità) e grazie alla varietà di processi e materiali disponibili, i reticoli di guida d'onda risonanti sono stati utilizzati in un'ampia gamma di applicazioni, sia in ricerca che in industria, come elementi di sicurezza ottica, bio-sensori attraverso l'indice di rifrazione e la fluorescenza, spettrometri e accoppiatori ottici.

Questa tesi descrive lo sviluppo e la realizzazione di dispositivi di diffrazione selettivi al colore mediante reticoli di guide d'onda risonanti. Sono investigate le proprietà di coppie di reticoli di guide d'onda risonanti aventi la stessa impedenza, una grandezza finita e diversi periodi del reticolo, che condividono lo stesso substrato rivestito dalla stessa guida d'onda. In particolare, uno specifico intervallo di lunghezze d'onda e accoppiato nella guida d'onda per mezzo del primo reticolo diffrattivo da un fascio incidente di luce bianca e disaccoppiato tramite il secondo reticolo diffrattivo ad un angolo diverso. Una serie periodica di queste coppie di reticoli di guide d'onda risonante permette di ottenere una diffrazione selettiva al colore. Inoltre, specifici metodi di progettazione basati su sferoidi prolati confocali sono derivati ed utilizzati per generare superfici con diversi periodi e orientamenti dei reticoli diffrattivi. Tali superfici possono filtrare una specifica porzione di una sorgente puntuale e posso redirezionarla e concentrarla in un altro punto nello spazio, ossia nel punto di osservazione. Queste superfici sono particolarmente utili in applicazioni in cui è richiesto di riconcentrare la luce, come l'ottica per la sicurezza, gli accoppiatori ottici per gli schermi oculari. Alcune realizzazioni di etichette per la sicurezza ottica attraverso autenticazione tramite smartphone sono presentate e discusse.

Dato che la fabbricazione di questi dispositivi è estremamente impegnativa, è stato sviluppato un metodo di fabbricazione che riduce il tempo di esposizione tramite litografia a fasci elettronici. Questo metodo è vantaggioso per fabbricare efficacemente i reticoli diffrattivi con diversi periodi e orientati ad angoli diversi. In particolare, viene inizialmente implementata

Acknowledgements

una pre-frattura delle linee del reticolo in una o più strisce più piccole dipendenti dal periodo del reticolo, e successivamente si frattura con un passo del fascio elettronico più piccolo del diametro del fascio stesso. Questa tecnica di frattura permette di esporre superfici complesse con un fascio di elettroni più largo di quello utilizzato con metodi standard di frattura in meno di 5 ore per cm^2, mentre una scrittura tradizionale col fascio di elettroni impiegherebbe più di 20 ore per cm^2 per ottenere la stessa qualità.

Nell'ultima parte sono descritte strutture ottiche che comprendono uno strato metallico e uno strato dielettrico su un un substrato di vetro ondulato. In sostanza viene studiata l'ibridizzazione dei plasmoni e dei modi della guida d'onda che è utilizzata per progettare un accoppiatore ottico selettivo al colore, dove i modi ibridi rilasciano energia nel substrato nel primo ordine diffrattivo dove diventano modi guidati. Questo accoppiatore può essere usato come elemento dispersivo quando la sorgente di luce bianca è divergente, permettendo ad esempio di realizzare spettrometri poco costosi, compatti e robusti.

Parole chiave: ottica, nanofotonica, reticolo di guida d'onda risonante, reticolo di diffrazione, diffrazione selettiva al colore, riorientamento del fascio ottico, ri-concentrazione, concentrazione, luce visibile, sorgente di luce bianca, specchio ellissoidale, fabbricazione scalabile, litografia tramite nanoimprinting, litografia tramite fascio elettronico, autenticazione mediante smartphone, sicurezza ottica dei documenti, combinatore ottico, accoppiatore ottico, schermo oculare, spettrometro.

Contents

Contents

Introduction

General Context

Resonant waveguide gratings (RWGs), also known as guided mode resonant (GMR) gratings, are optical structures based on dielectric corrugated waveguides, which can be used as coupler in thin film waveguides or as zeros order transmission or reflection devices [1].

The observations of Wood's anomalies in 1902 [2], complemented by Rayleigh in 1907 [3], paved the way for the development of a theoretical model by Fano in 1941, who could differentiate between two kinds of anomalies [4]. One is related to an abrupt variation of energy distribution between diffraction orders at the rising of a new order (i.e. the Rayleigh anomalies) and the other anomaly is due to a spectrally diffuse resonance, consisting of a leaky wave supportable by a metallic grating (i.e. the surface plasmon polaritons SPPs). Further works on gratings with dielectric coatings made by Maystre in 1972 [5] and by Neviere at al. in 1973 [6] set the basis for the theoretical analysis and the modeling of RWGs.

The field of RWGs boomed in 1990s: thanks to their high degree of tunability in terms of optical properties and the diversity of fabrication processes and materials involved, RWGs have been implemented in many different applications. For example, they can be implemented as refractive index and fluorescence biosensors [7, 8], or to enhance the light absorption of thin-film solar cells [9] and photodetectors [10], or in signal processing for photonic integrated circuits and optical communication [11]. Other applications may include polarizers [12] and wave plates designed with RWGs [13], passive RWG filters spectroscopic applications [14], active RWG filters as electro-optic [15] or thermo-optic tunable filters [16]. Their use as narrowband reflectors has also enabled the design of efficient mirrors for laser cavities [17]. Finally, their use in optical security devices represents an established and widespread industrial application [18].

In recent years the development of fabrication techniques, particularly involving the lithography of the master structure, has brought new opportunities: instead of fully periodic corrugations such as 1D or 2D gratings, it is now possible to fabricate non-homogeneous patterns [19]. Moreover the emerging of new applications such as near-eye displays [20] and the industrial demand to improve technologies for consolidated fields such as more modern optical security devices [21] or more compact and less costly spectrometers [22] have given a boost to the

study of RWGs.

Thesis Objectives

This thesis aims to study the properties of RWGs and to develop readily up-scalable devices potentially relevant for very high-volume production that could achieve color-selective diffraction and beam redirection.

One possible approach is to use a pair of finite size RWGs having different grating periods, but sharing the same substrate and waveguide, and being impedance matched. Another optical structure comprises metallic and dielectric corrugated layers to achieve hybrid plasmon waveguide modes. The latter structure is particularly interesting to achieve narrowband optical couplers to multimode waveguides.

Applications of the structures developed in this thesis are foreseen in a variety of fields where color-filtering and beam redirection are required, such as optical document security, see-through optical combiners for near-eye displays, spectrometers and biosensors, to name a few.

Organization

This thesis contains material published in several peer-reviewed publications and is organized as follows. Chapter 1 is dedicated to the review of the recent advances in RWGs. A brief historical introduction, as well the physics and modeling of RWGs is discussed. Some effects, which are the most relevant to the scope of this thesis, are also described, and some industrial applications of RWGs are reviewed. In Chapter 2, an overview of the numerical modeling and fabrication techniques used in this thesis is provided. Then, a description of the improvements I have achieved for both the simulation and fabrication is reported. In Chapter 3 the study of paired impedance matched RWG is detailed, and realizations for optical security are shown. In Chapter 4, the hybrid plasmon waveguide modes realized using a metallic and a dielectric layer are presented with the aim to develop a color-selective optical coupler. A general conclusion is provided in Chapter 5, along with an outlook for future opportunities of research and development.

1 Recent advances in resonant waveguide gratings (RWGs)

This chapter is based on the review paper: G. Quaranta, G. Basset, O. J. F. Martin, and B. Gallinet, "Recent Advances in Resonant Waveguide Gratings", Laser & Photonics Reviews **12**, 1800017 (2018). My contributions were in the literature review and the writing of Sections 1.1.2, 1.2.1, 1.2.3 and 1.3.1 to 1.3.3, as well as preparing the figures. The co-authors edited the manuscript and contributed to the discussion of the results together.

Resonant waveguide gratings (RWGs), also known as guided mode resonant (GMR) gratings or waveguide-mode resonant gratings, are dielectric structures supporting lateral leaky guided modes. They can operate from UV to microwave frequencies and exist in many different configurations. A broad range of optical effects are obtained using RWGs, such as waveguide coupling [23], filtering [24–26], focusing [27], field enhancement [28] and non-linear effects [29], magneto-optical Kerr effect [30] or electromagnetically induced transparency [31]. Thanks to their high degree of optical tunability (wavelength, phase, polarization, intensity) and the variety of fabrication processes and materials available, RWGs have been implemented in a broad scope of applications in research and industry: refractive index and fluorescence biosensors [7, 8], solar cells [9] and photodetectors [10], signal processing [11], polarizers [12] and wave plates [13], spectrometers [14], active tunable filters [15], mirrors for lasers [17] and optical security features [18]. This chapter is devoted to the historical context and to the fundamental physics and modeling of RWGs (Section 1.1), as well as to make an appropriate review of the most relevant effects (Section 1.2) and applications (Section 1.3) of RWGs to the scope of this thesis.

1.1 Fundamentals of RWGs

The aim of this section is to provide an historical introduction (Section 1.1.1) and to discuss the physics and modeling of RWGs (Section 1.1.2).

1.1.1 Historical perspectives and reviews of RWGs

Wood's observation of rapid variations in the reflected diffraction orders from ruled gratings has prompted an extensive amount of research [2]: Rayleigh gave the first interpretation of part of those anomalies five years later in terms of appearance or disappearance of diffracted orders from or into evanescent modes, respectively [3]. In 1941, Fano proposed that some anomalies may be created by the excitation of surface waves on the grating surface [4]. Hessel and Oliner employed an original theoretical approach based on guided waves rather than on scattering and could explain anomalies of deep grating grooves geometries using numerical tools, corroborating the explanation proposed by Fano [32]. Maystre developed in 1972 a rigorous vector theory able to accurately compute the properties of metallic gratings with any profile for any wavelength [5]. Experimental results used along this investigation exhibited variations associated with the metal used for the grating or the manufacturing method – especially with the presence of a metal oxide layer or a dielectric coating on the metal grating – thus supporting the existence of leaky guided surface waves with variable intensities [33]. Later, such gratings supporting quasi guided modes have been referred to as resonant waveguide gratings (RWGs) and are also known as guided mode resonant (GMR) gratings or devices, leaky mode resonant gratings, grating slab waveguides, resonant diffraction gratings, (resonant) grating waveguide structures, resonant subwavelength gratings, resonance grating couplers, or waveguide-mode resonances (WMRs). Cross sections examples of RWGs are shown in Fig. 1.1. They differ from high contrast gratings (HCGs), in which there are multiple vertical Bloch modes between the upper and lower grating boundaries [34]. The main difference is that RWGs rely on resonances with waves propagating along the grating, the so called leaky-modes. In HCGs there are also leaky modes, however their dispersion relation is largely altered by the interference of those vertical Bloch modes. HCGs have been reviewed by Chang-Hasnain and Yang [35]. A comparison of RWGs with other high-contrast metastructures, especially HCGs, has also been reported [36, 37]. RWGs can have geometries consisting of high contrast dielectric stripes surrounded by lower refractive index geometries, which are similar to HCGs (Fig. 1.1d). 1D photonic crystals slabs can also support guided mode resonances [38, 39]. We define here RWGs based on their physical behavior, relying on a leaky guided mode propagating over several grating grooves and ridges, rather than on a particular geometry. This definition of RWG based on their physical behavior is necessary due to the similarities between corrugated waveguide geometries and discrete ribbon geometries such as illustrated in Fig. 1.1b,d, as already computed by Knop using rigorous computations in 1981 [40].

The very high bandwidth provided by thin film dielectric waveguides has been investigated from the 1960s for light transport, especially for on-chip optical interconnects. Dakss et al. have experimentally replaced the conventional prism coupler with a grating coupler for thin dielectric films under laser illumination, using the leaky mode in-coupling of a RWG [41]. A few weeks later Kogelnik demonstrated a similar light-coupling using a gelatin volume hologram [42]. These two early demonstrations gave rise in the 1970s to intense research aiming at fully understanding the properties of these grating couplers in parallel to the development of distributed feedback mode selectors in laser media [43, 44]. Ostrowsky and Jacques measured
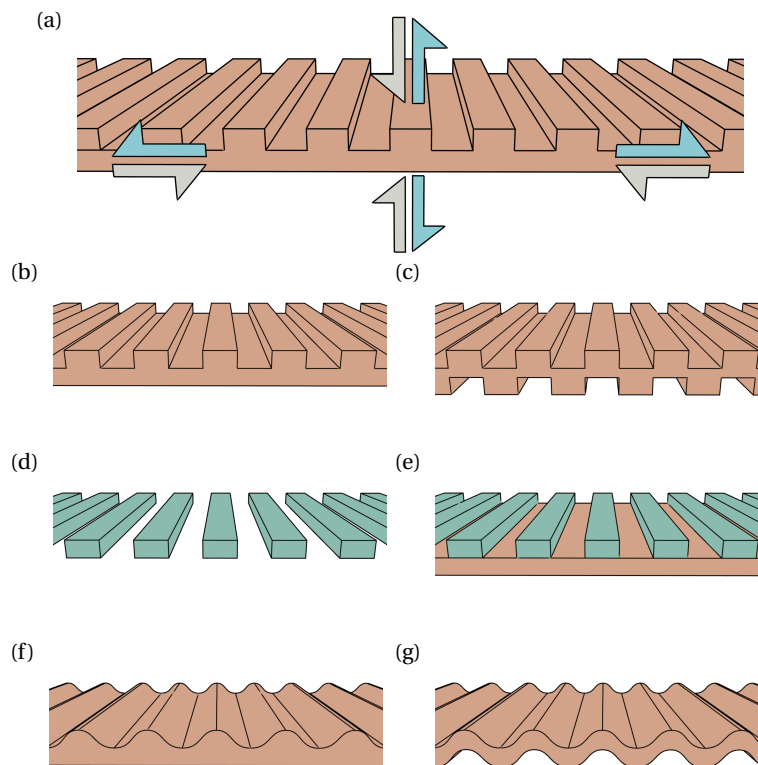
Figure 1.1 – Examples of common geometries of resonant waveguide gratings (RWGs). (a) Schematic of the four-port propagation channels, as input (white arrows) or as output (light blue arrows) which are typically used in RWGs. For example, light can be incident from free-space, coupled into a waveguide mode and outcoupled resonantly in specular reflection or transmission. The substrate and superstrate, not represented here, act as a cladding. (b) Single-sided rectangular corrugation of a waveguiding layer. (c) Double-sided rectangular corrugation with a thin film waveguide. (d) Waveguiding layer corrugated over its full thickness, providing an array of discrete ribbons. (e) Array of ribbons on a waveguiding layer. (f) Single and (g) double-sided sinusoidal corrugation of a waveguiding layer.

on a photoresist waveguide-grating coupler the TE/TM wavelength splitting of the resonance for the fundamental waveguide mode [45]. In 1973, Nevière, Petit and co-workers developed a rigorous model for the resonances of sinusoidal waveguide-grating couplers in photoresist for transverse electric (TE) polarized light [6], transverse magnetic (TM) polarized light [46] and the computation of the coupling coefficient for finite beams [47], which were confirmed with a high accuracy with experimental data provided by Jacques and Ostrowsky [48].

RWGs have also been extensively investigated for their response in the zeroth order of reflection and transmission. Knop provided a first rigorous model for binary structures such a grating lamellas made of high refractive index dielectrics [40], setting the basis of the rigorous coupled wave analysis (RCWA) modal method; he used this model to compute the zeroth order resonances and reflective spectra for a large number of more complex geometries of
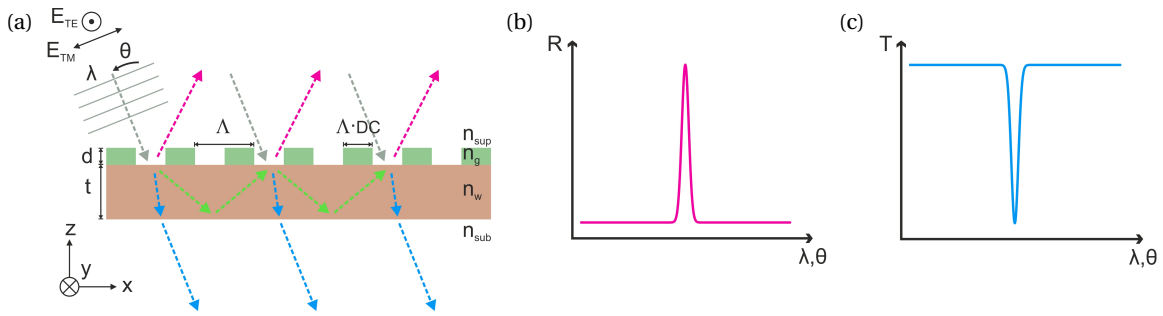
Figure 1.2 – Illustration of a standard RWG. (a) Propagation of light-rays in the RWG: a complete destructive interference happens in transmission at a specific angle and wavelength of incidence, resulting in a narrowband reflection. An example of reflection (b) and transmission (c) spectra for polarized light incident at normal at resonance of a monomode RWG.

RWGs [49]. In order to allow affordable and high throughput manufacturing, he proposed a thin-film coating of a waveguiding layer on a subwavelength-period grating, creating a double-corrugated interfaces geometry such as sketched in Figs. 1.1c and 1.1g. Sychugov and Tishchenko demonstrated the TE to TM polarization conversion of light using conical (non-collinear) incidence orientation [50, 51]. Gobulenko and Avrutsky observed the same resonances using a thin deposited ZnO corrugated waveguide [52, 53], achieving much narrower reflection wavelength-band in zero-order configuration, thanks to a much lower refractive index contrast of the waveguide. After having studied the first diffracted order resonant anomalies of a multiple dielectric layers coated aluminum diffraction grating, Mashev and Popov demonstrated experimentally similar results with a corrugated waveguide manufactured by ions exchanged from molten $AgNO_3$ [54, 55]. Avrutsky, Golubenko and their colleagues computed the zeroth order reflection and transmission behavior of RWGs and demonstrated their usefulness to stabilize laser emission [56–58].

After a review of the state of the art by Tamir in 1975 [59] and by Petit in 1980 [60], Rosenblatt et al. reviewed some analytical and numerical models for RWGs that had been developed in the 80s and 90s and compared such tools with a series of experimental results in 1997 [61]. Further conference proceedings were later written by Magnusson et al., presenting properties, applications and examples of RWGs [62–66]. Several reviews, book chapters and perspectives specifically focused on the application of RWGs in biosensing have also been written [7, 67–79].

1.1.2 Analytical model of shallow RWGs

A resonant waveguide grating (RWG) can be defined as a thin waveguiding film in optical contact, or merged, with a grating. The waveguiding film operates usually by having a higher refractive index than its surrounding media (the cladding), and because of its thin dimension it supports a discrete number of guided modes. These waveguide modes can be limited to the fundamental (zeroth mode) in very thin waveguides or comprise a few modes with different mode index for TE and TM polarization. In the latter case, for a given polarization

and wavelength, a RWG can support various guided modes having a different mode index and therefore transversal propagation speed and momentum. Light can be coupled into the waveguide modes by different grating diffraction orders, depending on the incidence angle and the wavelength (Fig. 1.2a). Some of this guided light is diffracted out of the guide while propagating, coupled back to radiation and interferes with the non-coupled reflected or transmitted waves, as illustrated with blue and magenta arrows in Fig. 1.2a. Depending on the wavelengths, this leads to a very high reflection or transmission, giving rise to a Fano or a Lorentzian-like lineshape profile at the zeroth order reflection (Figs. 1.2b and 1.2c). Those efficient resonances can be as narrow as 0.1 nm linewidth [61] and are very sensitive to angle and wavelength, with a typical angular to spectral linewidth ratio of $0.1\,°\mathrm{nm}^{-1}$ [80]. Depending on the wavelength and phase delay accumulated during propagation in the waveguide, the destructive interference can occur either in reflection or in transmission [56, 81, 82]. RWGs are therefore effective filtering structures, especially for collimated light. Further, RWGs can be designed to be extremely efficient diffraction elements off the Littrow configuration, as demonstrated experimentally by Destouches et al. [83]. Additionally, because the structure consists usually of dielectric materials only, it can be highly transparent and therefore used either in transmission or in reflection. RWGs do not suffer from thermal heating as in the case for metallic structures [84], which enables their use in a variety of high optical power applications such as mirrors and diffractive elements [85]. Each ridge and groove corrugating the waveguiding layer (Figs. 1.1b, 1.1c and 1.1e to 1.1g), or each of the discrete ribbons (Fig. 1.1d) of RWG can be considered a scattering element connected to a thin-film waveguide, building a periodic array of scattering elements in which quasi guided-modes, or leaky modes, can propagate. RWGs can therefore be considered as temporal or spatial optical integrators [86] as well as being used to enhance local electromagnetic field, for sensing [7] as drug discovery devices [73] or absorption sensors [87], and non-linear optics for second (SHG) of third (THG) harmonic generation [29, 88].

In case of a shallow grating depth d or when the grating is separated from the waveguide by a low-index separation layer, the waveguide mode is weakly perturbed by the grating because of the weak scattering by grating ridges and grooves, and it can be approximated to the one of a pure slab waveguide. Under this assumption, the equation describing modes in a slab waveguide can be coupled with the diffraction grating equation by setting the propagation wavevector of the mode in the slab waveguide to be equal to the wavevector of the light diffracted by the grating [89]:

$$\begin{cases} \tan\left(k_i t\right) = \dfrac{k_i\left(\gamma_i + \delta_i\right)}{k_i^2 - \gamma_i \delta_i} & \text{for TE Modes} \\[4mm] \tan\left(k_i t\right) = \dfrac{n_w^2 k_i \left(n_{\mathrm{sub}}^2 \gamma_i + n_{\mathrm{sup}}^2 \delta_i\right)}{n_{\mathrm{sup}}^2 n_{\mathrm{sub}}^2 k_i^2 - n_w^2 \gamma_i \delta_i} & \text{for TM Modes} \end{cases}, \tag{1.1}$$

where:

$$\begin{cases} k_i = \sqrt{n_w^2 k^2 - \beta_i^2} \\ \gamma_i = \sqrt{\beta_i^2 - n_{\text{sup}}^2 k^2} \\ \delta_i = \sqrt{\beta_i^2 - n_{\text{sub}}^2 k^2} \\ \beta_i = k\left(n_{\text{sup}}\sin\theta - m\dfrac{\lambda}{\Lambda}\right) \\ k = \dfrac{2\pi}{\lambda} \end{cases} \quad , \tag{1.2}$$

where λ is the wavelength in vacuum, θ is the polar angle of illumination, Λ is the grating period, m is the grating diffraction order, t is the waveguide thickness and n_{sup}, n_w, n_{sub} are the refractive index of the superstrate, waveguide and substrate, respectively. Equation (1.1) can also be derived considering the boundary conditions of the electric and magnetic fields at the two interfaces of a weakly corrugated slab waveguide, as analogously shown in Appendix C.2 of a four layer system.

Using this model, it is possible to derive a first approximation of the waveguide thickness and of the grating period to obtain a resonance peak for a specific geometrical configuration of the incidence light. An example of a weakly corrugated RWG studied using Eq. (1.1) is shown in Fig. 1.3: the agreement between numerical simulations made with rigorous coupled wave analysis (RCWA) in Fig. 1.3a and Eq. (1.1) in Fig. 1.3b is very good. Evaluated reflection spectra are shown in Fig. 1.3c at different waveguide thicknesses: when the waveguide is very thin, only the fundamental waveguide mode propagates and gives rise to a single peak in reflection at normal incidence. Conversely, when a thicker waveguide is used, multiple modes can be excited simultaneously at different frequencies. Furthermore, plots of field profiles of the RWGs at different waveguide thicknesses but at the same wavelength and polarizations are shown in Fig. 1.3d-f: their profiles are very similar to those of slab waveguides.

A shallower grating depth is used to make higher quality factor Q and narrowband resonances: a deeper grating height causes larger coupling and larger scattering losses leading therefore to a lower quality factor and broader resonances (see Section 1.2.1). For binary gratings, the duty-cycle DC, corresponding to the fill factor of the ridges, is also an important parameter which affects the dielectric perturbation. When the grating depth is deeper and has more influence on the profile of the waveguide mode, it is possible to define an equivalent homogeneous layer using the effective-medium theory (EMT) [90–92] to compute the effective refractive index n_{eff} to be used in Eqs. (1.1) and (1.2) in place of the refractive index of the waveguide n_w. For example, in a 1D grating with $t = 0$, n_{eff} for TE and TM polarization can be defined as [93]:

$$\begin{cases} \left(n_{\text{eff}_{TE}}^{(0)}\right)^2 = DC \cdot n_g^2 + (1 - DC) \cdot n_{\text{sup}}^2 \\ \left(n_{\text{eff}_{TM}}^{(0)}\right)^2 = \dfrac{n_{\text{sup}}^2 n_g^2}{n_{\text{sup}}^2 \cdot DC + n_g^2 \cdot (1 - DC)} \end{cases} \quad . \tag{1.3}$$

This equation provides the zeroth order approximation (i.e. indicated with the superscript (0)) with respect to the profile period-to wavelength ratio Λ/λ [92]. For higher orders approximations, it is necessary to analyze the field distributions in a non-static manner. The second order expressions in terms of the ratio Λ/λ are provided, for example, in [94]. Other common effective medium approximations are the Maxwell-Garnett model, the Bruggeman model and the Lorentz-Lorentz model [92, 95]. In the rigorous coupled wave analysis (RCWA), the refractive index in each layer is expanded into Fourier harmonics, as in Eq. (2.1). The EMT provides a more accurate evaluation of the mode indices for both significantly corrugated waveguides and discrete ribbon geometries, however is only valid for subwavelength structures (i.e. $\Lambda/\lambda < 0.5$).

The Rayleigh approximation is another model to solve wave coupling problems [96, 97]. It is based on the Rayleigh hypothesis, which implies that field can be expanded inside the grooves on the same bases as the outside modulated region [98]. Its validity is limited by the grating depth to period ratio [99]:

$$\frac{d}{\Lambda} < 0.144. \tag{1.4}$$

Under this assumption, the model delivers very reliable results and permits to define phenomenological parameters, such as free space wave - guided mode coupling coefficients, intra-guide coupling coefficients between guided modes and radiation coefficients. Such phenomenological parameters, which cannot be derived by EMT, are especially useful to the understanding of such optical structures even in the case of deep structures and can be utilized to design functional RWG elements.
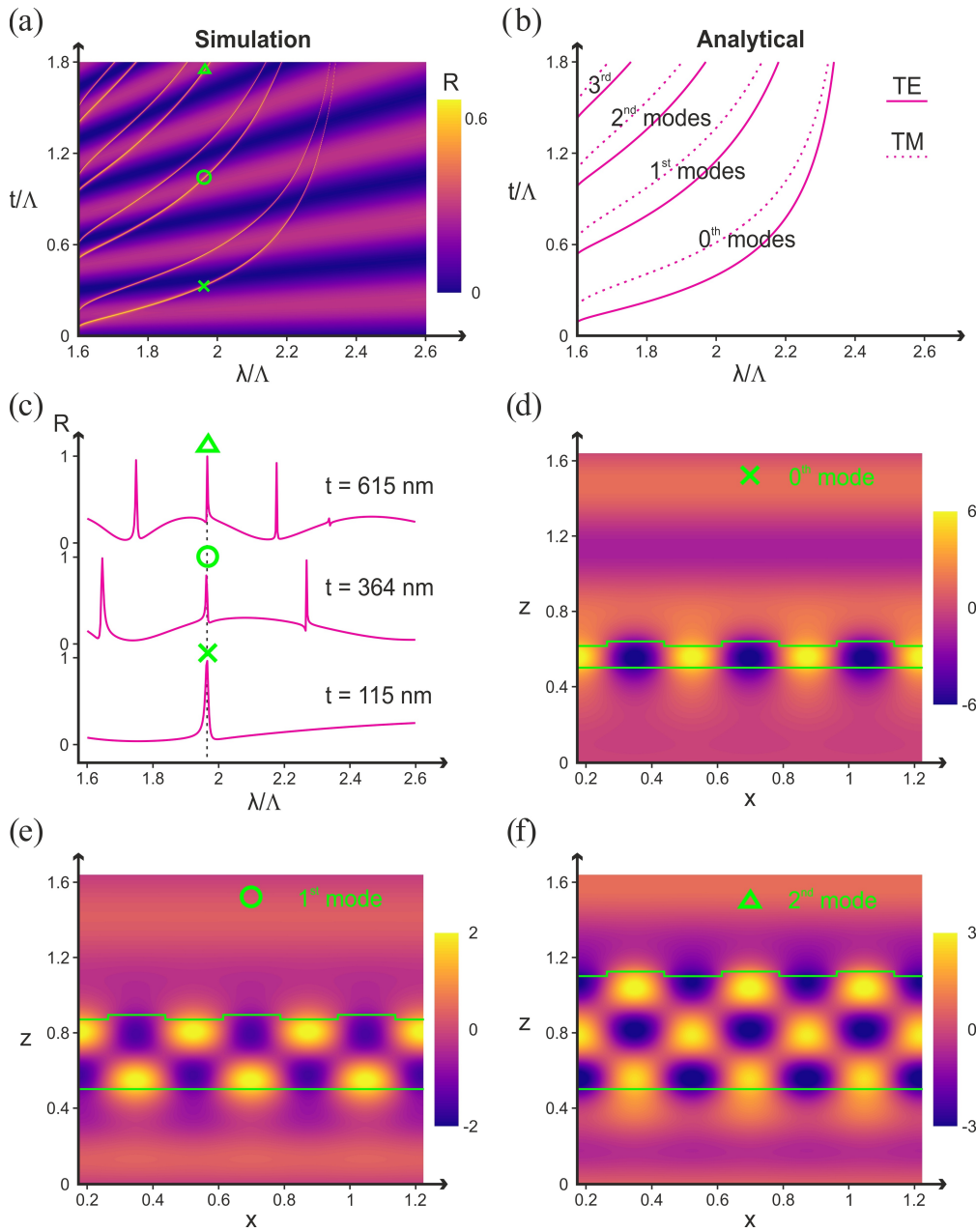
Figure 1.3 – Example of RWG with the following parameters: $\theta = 0°$, $\Lambda = 350\,\text{nm}$, DC = 0.5, $d = 25\,\text{nm}$, $n_{\text{sub}} = 1.6$, $n_w = n_g = 2.4$, $n_{\text{sup}} = 1$. (a) RCWA simulations of the reflectance at different wavelengths λ and waveguide thicknesses t for both polarizations TE and TM averaged. (b) Equation (1.1) implemented for this example in reflection for $m = \pm 1$, showing an excellent agreement with the simulations for the prediction of the resonant peaks. (c) Reflectance under TE polarized incidence at three different waveguide thicknesses: $t = 115\,\text{nm}$, $t = 364\,\text{nm}$, $t = 615\,\text{nm}$. (d-f) Steady-states field profiles Re $[E_y/E_0]$ under TE polarized incidence at the three waveguide thickness values previously listed at the same resonance wavelength $\lambda = 687\,\text{nm}$, corresponding to the resonance of the fundamental, 1st excited and 2nd excited modes, respectively.

1.2 Versatily of RWGs: a review of some effects

RWGs make use of a grating to couple light in and out of a thin waveguide. As already briefly outlined in the introduction, RWGs have been designed in a variety of operation modes, beyond the functionality of a mere grating coupler. In this section we include the description of the effect which are the most relevant to the scope of this thesis, in particular: narrowband or broadband filtering in the zeroth order of transmission and reflection (Section 1.2.1), combination with surface plasmon resonances (SPRs, Section 1.2.2), focusing (Section 1.2.3), field enhancement and nonlinear effects as well as other effects such as magneto-optical Kerr effect or electromagnetically induced transparency. The design rules for RWGs, materials and the parameter range generally depend on the targeted optical effect and the fabrication constraints.

1.2.1 Narrowband and broadband filters

The bandwidth of the filtered spectrum can be made particularly narrow using a weak in-coupling and out-coupling efficiency with e.g. shallow gratings (Fig. 1.4a) [61]. When used as narrow bandpass spectral filters in either transmission or reflection, RWGs are characterized by a spectral response which can be identified with a Fano lineshape [82, 100–102]. RWGs can theoretically reach 100% reflection efficiency when their profile is vertically or horizontally symmetric [103] or when integrated with quarter-wave Bragg stacks [82]. Recently, a high efficient narrowband transmission filter has been demonstrated with two crossed and strongly modulated RWGs [104] and at normal incidence with partially etched single-layer RWG [105, 106]. RWGs can also be utilized to make efficient wideband reflectors using a periodic array of high index scatterers on a low index layer (Fig. 1.4b,c) [24, 107]. The bandwidth and the efficiency of the broadband reflectors with partially etched RWGs can be tuned with the grating depth, fill factor, the thickness of the homogeneous layer or with tapered sidewalls [108–110]. Efficient wideband reflectors with steep sidewalls can be obtained by operating RWGs at the proximity of the Rayleigh angle [111]. When a RWG resonates at an angle corresponding to the Rayleigh anomaly, the zeroth order reflection energy is almost completely transferred into a first order transmitted mode with a sharp transition, as shown in Fig. 1.5 [112]. The Rayleigh anomaly is related to the rapid efficiency variations of diffraction orders by a variation of the wavelength or the incident angle [3, 113]. It occurs for a specific angle (θ) and wavelength (λ) value: $n_{\mathrm{sup}} \times \sin\theta = \pm n_{\mathrm{sub,sup}} - m\frac{\lambda}{\Lambda}$, where Λ is the grating period and m is the diffraction order ($m = \pm1, \pm2, ...$) for reflection and transmission. This interaction is helpful for designing transmission filters with sharp peaks [112]. Rahman et al. demonstrated a system of metallic-dielectric grating structures that significantly improves the transmission efficiency by tuning the waveguide thickness to satisfy both the guided-mode and the Fabry-Perot resonances at the same wavelength [114]. We would like also to report the fabrication of wedged RWG used as tunable filers, whose resonance spans over 40 nm in the visible range for a 50 nm increment of the waveguide thickness [115]. Other implementations include the patterning of RWG on suspended membranes for improved quality factor and flattened sidebands [116–118], i.e. for
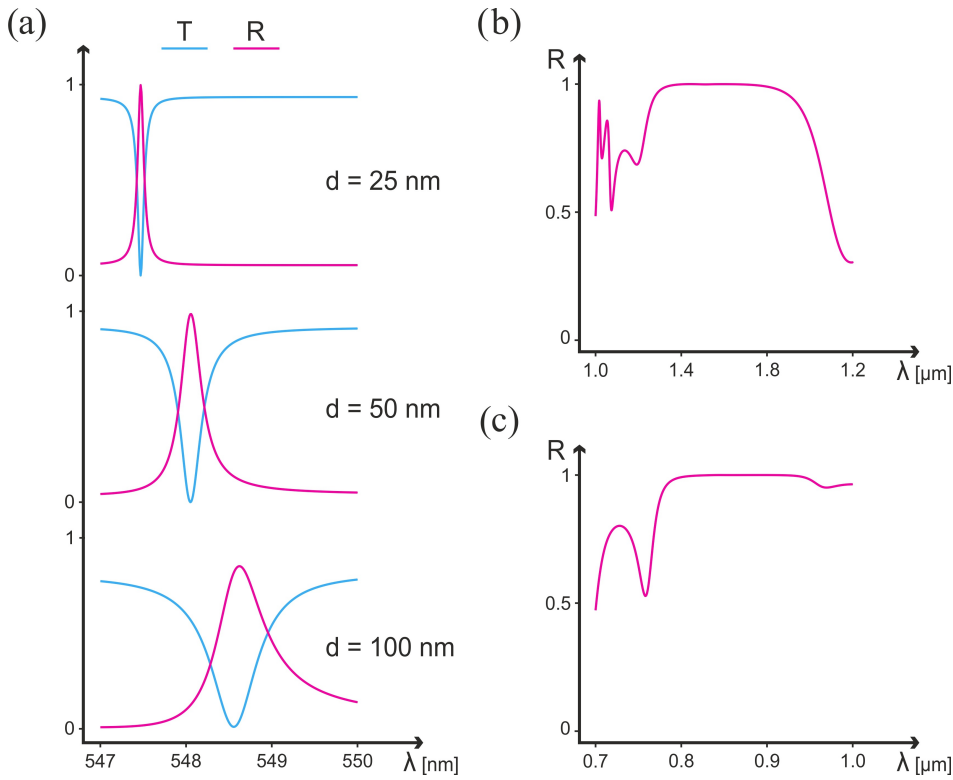
Figure 1.4 – (a) RCWA simulations of the grating depth (d) variation to tune the reflection/transmission bandwidth in TM polarization. Parameters: $\theta = 15°$, $\Lambda = 400\,\text{nm}$, $DC = 0.5$, $t = 300\,\text{nm}$, $n_{\text{sub}} = 1.6$, $n_w = n_g = 1.7$, $n_{\text{sup}} = 1$. (b,c) RCWA simulations of TM polarized broadband RWG reflectors in different IR wavelength ranges. (b) Parameters: $\theta = 0°$, $\Lambda = 700\,\text{nm}$, $DC = 0.75$, $d = 460\,\text{nm}$, $t = 840\,\text{nm}$, $n_{\text{sub}} = 3.48$, $n_w = 1.47$, $n_g = 3.48$, $n_{\text{sup}} = 1$. (c) Parameters: $\theta = 0°$, $\Lambda = 340\,\text{nm}$, $DC = 0.68$, $d = 220\,\text{nm}$, $t = 2\,\mu\text{m}$, $n_{\text{sub}} = 3.72$, $n_w = 1.454$, $n_g = 3.72$, $n_{\text{sup}} = 1$. Data from [24].

laser cavities [119], and RWGs on concave lenses to increase the resonance wavelength and decrease the linewidth [120]. Finally, RWGs made with antireflective coating have also been studied [121, 122].

1.2.2 RWGs coupled with surface plasmon polaritons

Plasmon materials are metals with a very high electron mobility, in excess of $10^{22}\,\text{cm}^{-3}$, such that when light impinges on a nanostructure made from such a material it excites a collective oscillation of the free electrons in the metal, called a plasmon resonance [123]. Consequently, the interaction of light with plasmonic nanostructure is extremely strong, leading to very large scattering cross-sections in the far-field and enhancement of the near-field intensity by several orders of magnitudes. Combining plasmonic nanostructures with RWGs has been proposed as early as the 90s by Parriaux and Voirin, to take advantage of low-loss propagation and high near-field enhancement for sensing applications [124]. Over the last decade, progress
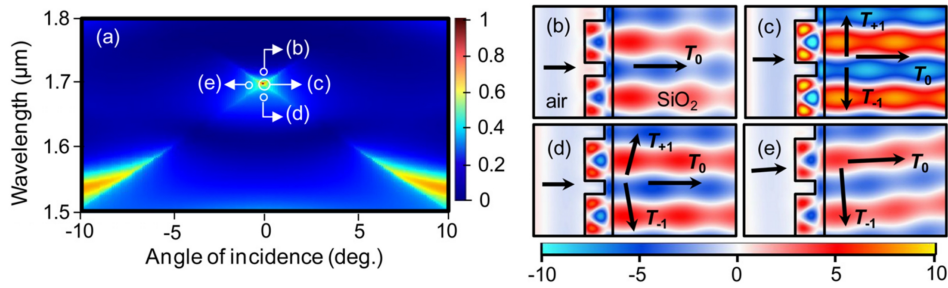
Figure 1.5 – (a) Simulated transmittance of a RWG optical filter coupled with Rayleigh anomaly in TM polarization. Parameters: $\Lambda = 1130\,\text{nm}$, $DC = 0.723$, $d = 405\,\text{nm}$, $t = 160\,\text{nm}$, $n_{\text{sub}} = 1.5$, $n_w = n_g = 3.48$, $n_{\text{sup}} = 1$. (b) Field distributions for several cases of angle and wavelength as indicated in (a): the case (c) is at the exact resonance condition, and in the case (e) there is a strong transmitted first order that causes a decrease of the zeroth order transmission. Reproduced with permission from [112]. Copyright 2013, AIP Publishing LLC.

in nanotechnology has enabled the seamless integration of plasmonic metals with RWG to take advantage of these features [125]. Metallic RWGs can combine coupled-mode resonances and plasmonic resonances near the Rayleigh anomaly [126], thus exhibiting extremely narrow spectral features with high efficiency [127]. This approach can be used to produce an extremely broad range of colors [128]. It is worth mentioning that these two examples rely on aluminum as plasmonic material less common than gold, that is usually the material of choice for plasmonics, since it is easy for nanofabrication [129]. Nguyen-Huu et al. have used silver to produce broadband and high transmission efficiency color filters [130]; interestingly, these authors also consider an additional dielectric layer on top of the RWG structure, which appears to improve the overall performances. Other authors have taken a different approach and fabricated a device with similar performances using an aluminum grating on an ultra-thin 100 nm silicon nitride membrane [131]. Recently, metasurfaces – optical surfaces that exhibit useful and often uncommon functionalities – have emerged as a strong field of research [132], which has prompted revisiting many classical photonics devices. RWGs also follow that trend and interesting reports have been published on the combination of gradient metasurfaces with a waveguiding layer [133]. Whilst a conventional grating provides a constant phase gradient to the incoming light, a metasurface has the potential to engineer the phase in a more versatile manner. This phase can also be engineered in two dimensions, contrary to a conventional grating, which is intrinsically one-dimensional. Two-dimensional plasmonic RWG devices can exhibit, for example, a useful polarization-sensitive behavior that produces a dichroic response and can be used to engineer electrically-tunable filters [134]. Traditionally, plasmonic nanostructures have been successfully used for sensing [135]. Magnusson and colleagues have reviewed how such nanostructures can be combined with RWG to produce even more efficient and versatile sensors [136]. Chien et al. have shown how coupled waveguide–surface plasmon resonance biosensor can be useful to overcome the limitations associated with Kretschmann attenuated total reflection used on conventional biosensors [137]; as a matter of fact, RWGs maintain their performances, even under normal illumination. The strong
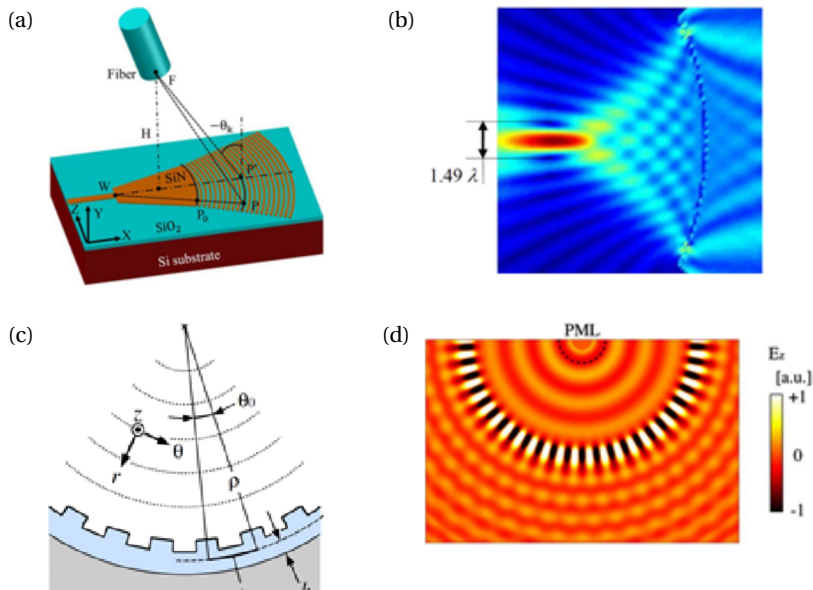
Figure 1.6 – Schematics of a self-imaging chip-fiber grating coupler. Reproduced with permission from [23]. Copyright 2012, OSA. (b) Electric field around a RWG used as focusing reflector. Reproduced with permission from [27]. Copyright 2011, CC BY 3.0. (c) Schematic of a curved RWG and (d) the electric field at resonance wavelength. Reproduced with permission from [142]. Copyright 2011, OSA.

near-field produced by a plasmonic nanostructure can induce interesting optical effects that go beyond light scattering. This has been used by Zeng et al. in a RWG device to boost the photoinduced charge-transfer rate of hot electrons into a semiconductor material [138]. So far, we have presented some examples of RWGs that incorporate plasmonic elements and rely on the optical resonances that are localized on them (so-called localized plasmon resonances). There exists another family of plasmonic effects, so-called propagating plasmon resonances, that are associated with extended surfaces [139]. Many experiments on propagating plasmon resonances use a grating to excite this optical mode that propagates then on a thin metal film [140]. Sometimes, the mode is out-coupled using a second grating [141], thus representing a device very similar to a RWG, albeit with an extremely thin metal waveguiding layer.

1.2.3 RWGs as focusing elements

Advanced patterning enables creating beam shaping devices with more freedom in the manipulation of the wavefront, such as for beam steering or focusing. Concentric-circular focusing grating couplers have been known since a long time [143–145] and they have been implemented in optical routing, e.g., for wavelength division multiplexing [146, 147], for cavity resonators [148, 149], or for quantum information processing [150, 151]. Recent optimizations include circular RWGs on a membrane [152], apodized focusing grating couplers (sketched in Fig. 1.6a) [23] and long working distance gratings [153]. A focusing spatial bandpass transmis-

sion filter based on a periodic RWG was also reported with a multilayer geometry allowing broadband reflection sidebands [106]. Instead of curving the grating lines on flat substrates, GMRs can also be created on curved surfaces, such as on parabolic reflectors to create wideband focusing devices (see Fig. 1.6b) [27] or on cylindrical surfaces (see Figs. 1.6c and 1.6d) [142] to enhance the quality factor of the related cylindrical cavities [154] by hybrid resonant modes coupled to whispering gallery modes [155]. Fattal et al. demonstrated the possibility of using 1D subwavelength grating (SWG) with varying duty-cycle or varying period to achieve local control over the phase of the reflected beam, realizing very long focal/small angles beam redirection reflective lenses [156, 157]. Given the distributed nature of the resonance in waveguide-gratings, thus achieving large phase shift at a very small scale, enabling large angle redirection, appears intrinsically difficult with such approaches. More localized resonances such as vertical GMRs present in HCGs and some dielectric metasurfaces appear better adapted. Such approach was for example demonstrated with 2D non-periodic SWGs, while additional optical functionalities can be obtained by combining finite-size SWGs with different dimensions [158].

1.3 Some industrial applications of RWGs

RWGs can be used as coupling and waveguiding elements, near-field enhancers, zeroth or higher orders diffraction elements and filters with a tailored control of the intensity and phase of the diffracted optical fields. Thanks to their high degree of tunability in terms of optical properties and the diversity of fabrication processes and materials involved, RWGs have been implemented in many different applications. For example, they can be used as refractive index and fluorescence biosensors [7, 8], or to enhance the light absorption of thin-film solar cells [9] and photodetectors [10], or in signal processing for photonic integrated circuits and optical communication [11]. Other applications may include polarizers [12] and wave plates designed with RWGs [13], passive RWG filters spectroscopic applications [14], active RWG filters as electro-optic [15] or thermo-optic tunable filters [16]. Their use as narrowband reflectors has also enabled the design of efficient mirrors for laser cavities [17]. In this section we review their use in optical security devices (Section 1.3.1), spectroscopy (Section 1.3.2) and refractive index biosensors (Section 1.3.3), which are the scope of applications of this work.

1.3.1 Optical security

In the early 1980s the fraction of counterfeited US dollars and other major currencies experienced a rise due to the widespread accessibility of new low-cost printing technologies, i.e. color photocopiers. This driving force and the invention of very high-throughput and affordable production techniques based on roll-to-roll nanoimprint lithography (NIL) and physical vapor deposition (PVD) enabled the wide implementation of optically variable devices (OVDs) and their use to secure various documents and goods such as credit cards, banknotes and identification documents [159]. Following the successful implementation of diffractive opti-
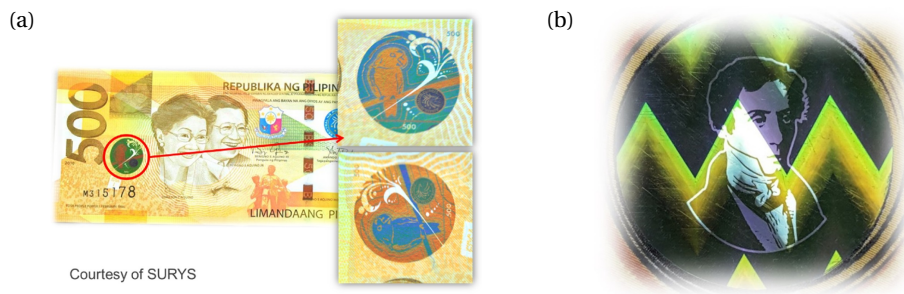
Figure 1.7 – (a) DID™ patch produced by Surys and securing the large denomination banknotes of the Philippines where reflective color permutation is achieved for a 90° document rotation. (b) DID™ Graphic Wave security label providing out of specular visibility and dynamic graphics. Reproduced with permission from [21]. Copyright 2017, Surys.

cally variable image devices (DOVIDs), RWGs-based diffractive identification devices (DID™) demonstrated a particularly high robustness against forging [18] and enable visual control in any light condition, including fully diffused ambient lighting thanks to a color-angular dependent zeroth order reflection [81]. The working principle builds on highly corrugated waveguide geometries having a broadband reflection in the visible spectral range. The angular dependency of the zero-order specular reflection gives rise to various color perceptions at different observation points. Authentication labels made with RWGs are polarization dependent but are easily distinguishable by naked eyes under unpolarized white light and under particular viewing angles while maintaining a high transparency [160]. In particular, a maximal visual impact has been reached with a green to red color inversion when rotating the observation point from collinear (i.e. across grating lines) to conical (i.e. along grating lines) at an oblique viewing angle located approximately at 30° from the normal to the document. RWGs are currently used to secure billion of documents every year including identification documents in the form of security overlays on passport data-pages and identity cards [21] (example in Fig. 1.7a). Since the first implementation on passport in 2003, not a single counterfeiting or lure of the DID™ could be reported despite their use in more than 40 countries. Various new developments and variations allow designing different control protocols and viewing angles (Fig. 1.7b) [21].

1.3.2 Spectroscopy

Spectroscopy with RWGs is an application that has been recently emerging, triggered by the need for compact devices which can be satisfied thanks to the use of waveguiding. Several implementations have been proposed using RWGs as waveguide couplers or zeroth order filters. A concept of RWG out-couplers to angularly separate the different wavelengths coupled in a waveguide in combination with a plano-convex lens to focus them on a photodetector array has been proposed [162]. Furthermore, the RWGs can be curved in order to directly achieve the focus [163]. Another demonstration of a compact device has been made by printing a customized organic photodetector array on the out-coupling RWG [164, 165]. Using
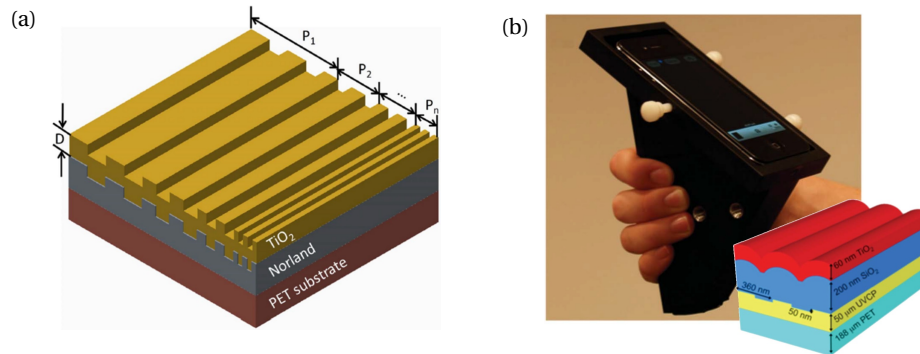
Figure 1.8 – (a) Schematic of a RWG with gradient grating period. Reproduced with permission from [161]. Copyright 2016, IEEE. (b) Spectroscopic biosensor for smartphone application based on RWGs, as illustrated in the inset. Reproduced with permission from [14]. Copyright 2013, The Royal Society of Chemistry.

RWGs in the zeroth order of diffraction, a possible technique to spatially separate resonance wavelengths uses a gradient in the thickness of the waveguide, reaching a resolution as small as 0.011 nm for the wavelength range between 800 nm and 900 nm [166], or alternatively with a gradient in the grating period (Fig. 1.8a) [161, 167]. Mid-IR spectrometers based on RWGs were also reported for infrared spectroscopic imaging using e.g. a filter wheel to sweep for the different bands [168]. Other applications include the measurement of vibrational modes of molecules [169], while discrete-frequency IR spectroscopy [170] has been used for measurements of tissues and polymer samples and for implementing coherent absorbers [171]. Spectrometers based on RWGs also apply to biosensing with incoherent light and, as an example, they can be implemented with broadband light from external sources (such as LED or incandescent lamps) and the camera of a smartphone, as illustrated in Fig. 1.8b [14]. A recent development of filters realized with RWGs includes a stack of two RWGs with a Fabry-Perot resonator to generate a transmission peak [172]: the grating duty cycle and period are controlled to obtain a set of narrowband filters with different central wavelengths.

1.3.3 Refractive index biosensors

As a result of the binding of molecules on a RWG surface, the effective refractive index (n_{eff}) of the guided-mode of a RWG varies, producing a shift in the resonance wavelength [7]:

$$n_{\text{sup}} \sin\theta = m\frac{\lambda_0}{\Lambda} - n_{\text{eff}}, \tag{1.5}$$

where n_{sup} is the refractive index of the superstrate, θ is the waveguide coupling angle (i.e. in-coupling or out-coupling, depending on the configuration), m is the diffraction order, λ_0 is the wavelength in vacuum at which the maximum coupling and resonance occurs and Λ is the grating period. An analytical model based on a slab waveguide, where the propagation constant has additional constraints, can be used to predict, with an accuracy

of 0.45 nm across the visible spectrum, the resonance shift caused by the refractive index changes, including for deep grating modulation [174]. Furthermore, the phase of the out-coupled pattern is also a useful source of information: Mach-Zehnder interferometers based on RWGs have been designed [175] and Sahoo et al. have recently proposed an analytical model to evaluate the phase and shown its importance in refractive index sensing [176]. Many different implementations of RWG have been suggested to create portable and label-free biosensors; they all rely on a strong spatial overlap between the RWG evanescent wave and the analyte. Compared to other methods for detecting the refractive index change (e.g. interferometric systems), RWGs are usually less sensitive because of the shorter interaction length. On the other hand, they support a higher throughput detection system and they can be implemented in less expensive sensing applications, since they are less sensitive to ambient or sample temperature fluctuations [7].

Let us mention for the interested reader the several specialized reviews on RWG biosensors. Cooper reviewed optical biosensors made with different technologies (plasmon resonance, waveguides and resonant mirrors) [177] and compared advantages and drawbacks of labeled assays and label-free assays [67] including RWGs biosensors and a list of manufacturers. An example of application of a commercial RWG biosensor for live cell sensing is illustrated in Figs. 1.9f and 1.9g [17], where different colors show different resonance wavelengths depending on the different culture conditions of the cells. Fang et al. reviewed optical biosensors for cell sensing and their potential implications in drug discovery, for which RWGs biosensors are presented as being the most popular ones, together with SPR biosensors [68, 72]. Fang et al. authored also two book chapters reviewing RWG biosensors for whole-cell assays for drug discovery [73] and RWG biosensors with high-throughput analysis [178]. More details on modeling and mechanisms for RWG biosensors are described in [7, 69, 70], while different practical implementations are reviewed in [7, 71, 75]. RWGs have also been used in fragmented-based drugs screening in both academic and industrial projects [74]. Geschwindner et al. have written a focus on small-molecules screening with RWGs biosensors; they emphasize the specific advantages of the inhibition in solution assay, in contrast to traditional direct binding assay [76]. Recent label-free silicon-based optical biosensors, including RWG-based biosensors, and their implementation into lab-on-a-chip platforms have been reported by Gavela et al. [78]. Finally, a recent review from Paulsen et al. about RWG biosensors is focused on compact readout systems for point-of-care applications and the implementation of multiperiodic and deterministic aperiodic RWGs in order to design specific resonances [79].
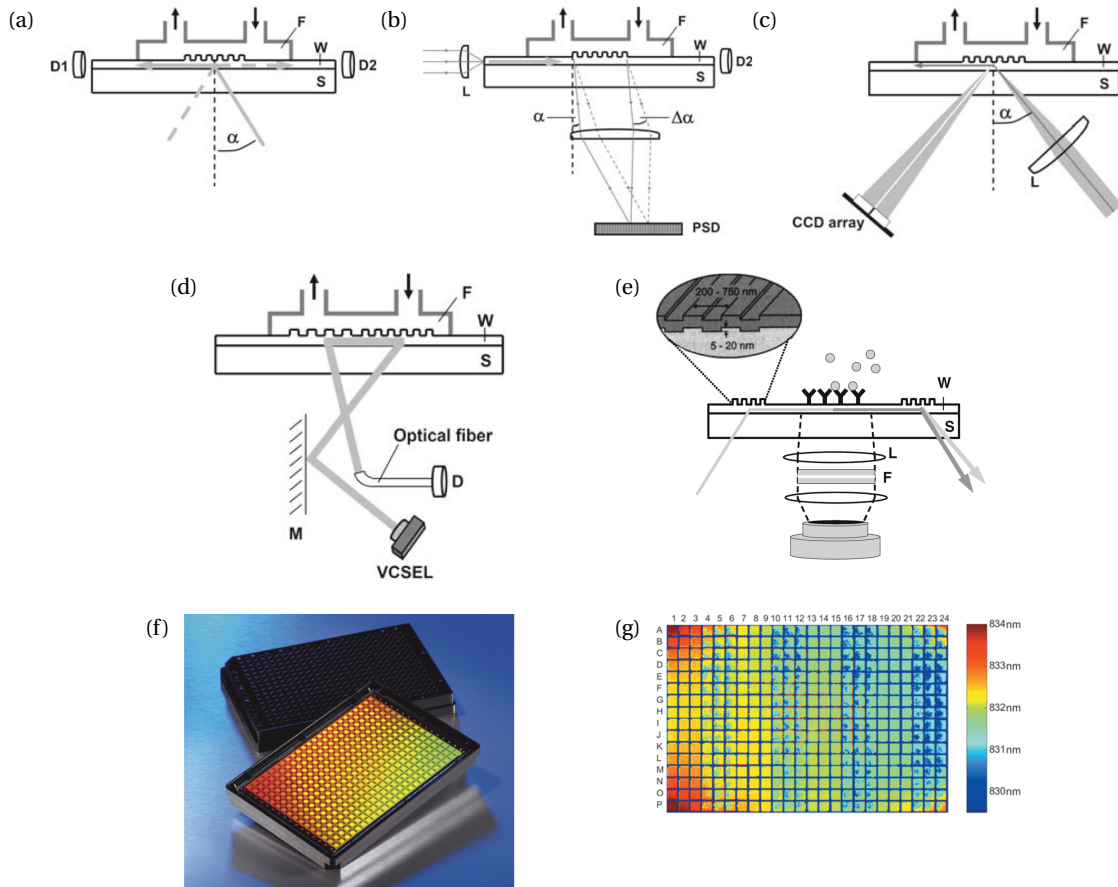
Figure 1.9 – Schematic drawings of some different RWG configurations for sensing: (a) an input grating coupler, in which a RWG grating is used to couple light in the waveguide, which is then sensed, and, conversely, (b) an output grating coupler. (c) A reflected-mode grating coupler similar to (a) but sensing the reflection spectra. (d) A wavelength interrogated optical sensor (WIOS), made by two different RWGs to sense the back-scattered light at a different angle and (e) an evanescent-field fluorescence, made with two RWGs separated by an intermediate flat waveguide. Reproduced with permission from [7]. Copyright 2010, Springer-Verlag Berlin Heidelberg. (f) A Corning Epic™ 384-well RWG biosensor plate, each containing an independent RWG biosensor allowing high throughput screening of intractable targets [67] and (g) a false-colored image of the resonance wavelengths of that plate after overnight culturing of human epidermal carcinoma cells planted in different conditions [173]. (f) Reproduced with permission from [67]. Copyright 2006, Elsevier Ltd. (g) Reproduced with permission from [173]. Copyright 2010, American Institute of Physics.

1.4   Conclusions

Resonant waveguide gratings (RWGs), also known as guided mode resonances (GMRs) and several other names, use the periodicity of a grating to couple light into a thin waveguide. Therefore, they have been used extensively as waveguide couplers for, e.g., optical communication and signal processing for the in-coupling and out-coupling of thin waveguide modes with strong wavelength, polarization and angular dependences. Their incoupled quasi-guided modes can interfere dramatically with the incident illumination depending on the phase difference and generate narrowband reflection and transmission features, leading to unique zeroth order properties. This mechanism makes them highly efficient narrowband or broadband reflectors, as well as transmission filters with applications as laser mirrors, advanced detection systems or spectrometers as well as highly efficient diffraction elements. In another direction, cost efficient fabrication processes and unique appearance have enabled their pervasive use as optically variable devices in optical authentication and document security. Their polarization dependent behavior has led to the development of polarizers, polarization rotators and wave plates. The control of the optical near-field has found widespread applications in biological refractive index sensing, fluorescence sensing, nonlinear effects and optical switching, as well as enhancement of solar light harvesting.

2 Advanced simulation and fabrication methods for RWGs

Part of the results and the literature review presented in this chapter were published in:

- G. Quaranta, G. Basset, O. J. F. Martin, and B. Gallinet, "Recent Advances in Resonant Waveguide Gratings", Laser & Photonics Reviews **12**, 1800017 (2018).

- G. Quaranta, G. Basset, O. J. F. Martin, and B. Gallinet, "Color-Selective and Versatile Light Steering with up-Scalable Subwavelength Planar Optics", ACS Photonics **4**, 1060–1066 (2017).

- G. Quaranta, G. Basset, Z. Benes, O. J. F. Martin, and B. Gallinet, "Light refocusing with up-scalable resonant waveguide gratings in confocal prolate spheroid arrangements", Journal of Nanophotonics **12**, 016004 (2018).

- G. Quaranta, G. Basset, O. J. F. Martin, and B. Gallinet, "Steering and filtering white light with resonant waveguide gratings", Proc. of the SPIE **10354**, 1035408 (2017).

My contributions were: literature review on fabrication methods, scripting and running of the numerical simulations and the design files, optimizing the electron beam lithography fabrication, designing and fabricating the samples, measuring them, analyzing the data, preparing the figures and writing the papers. The co-authors edited the manuscripts and contributed to the discussion of the results together.

This chapter is devoted to the description of simulation and fabrication methods for RWGs. In Section 2.1, an overview of the different numerical modelings used to carry out the work in this thesis is reported and the different methods are compared. In Section 2.2, the strategies that I have used to improve the analysis of RWGs in FDTD and RCWA are described. In particular, I developed specific procedures to simulate periodic structures illuminated with a broadband source at an angle and the possibility of calculating the field distribution with the in-house RCWA package. Section 2.3 presents two origination techniques of gratings which have been used or considered for the work of this thesis: laser interference lithography, a standard process for periodic and uniform large areas, and electron-beam lithography, which is more suitable

when the pattern is not uniform or homogeneous. Furthermore, some thin-film deposition techniques and the nanoimprint lithography (NIL) (Section 2.3.3) are also described, as part of the fabrication steps used for this work. Finally, in Section 2.4, the optimization of the electron beam lithography is reported. It consists on both the optimization of the MATLAB code used to generate the lithographic layout, as well as a fracturing method to efficiently expose gratings with different periods and oriented at different angles.

2.1 Numerical modeling of RWGs

Numerical modeling of RWGs is an essential step for this design and can provide quantitative information such as diffraction efficiency and fabrication tolerances, especially for complex or realistic structures where analytical models cannot be directly applied. A variety of methods is available for the numerical simulation of the optical properties of optical micro and nanostructures, and more specifically RWGs. In this section, the three methods which have been used to model RWGs for the work of this thesis are reviewed: RCWA (Section 2.1.1), FDTD (Section 2.1.2) and FETD (Section 2.1.3).

2.1.1 Rigorous coupled wave analysis

The rigorous coupled wave analysis (RCWA), also known as coupled wave method (CWM), modal method with Fourier expansion (MMFE) or Fourier modal method (FMM) is among the most popular numerical methods for the simulation of optical gratings. It mainly consists in expanding the dielectric permittivity function of the grating and the electromagnetic fields in the plane of the grating using Fourier harmonics and enforcing boundary conditions at the different interfaces. A first derivation of this method can be attributed to Knop for a binary transmission phase grating [8]. We would like to provide here a formulation example of the method to give the reader a first view of its advantages, limitations and challenges. Additional details as well as alternative formulations are provided in the cited references. A linearly polarized electromagnetic wave is incident at an arbitrary angle of incidence θ and at an azimuthal angle ϕ upon a binary dielectric or lossy grating. The grating period Λ is, in general, composed of several regions with different refractive indices (Fig. 2.1).

The permittivity inside the grating region is expanded into Fourier harmonics in each layer indexed by l:

$$\varepsilon_l(x) = \sum_{n=-N}^{N} \varepsilon_{n,l} e^{i\frac{2\pi n x}{\Lambda}}, \tag{2.1}$$

where $\varepsilon_{n,l}$ is the nth Fourier harmonics of ε_l. Similarly, the electromagnetic field is expanded into Fourier harmonics in each layer. Applying Maxwell's equations results in a wave equation which can be solved numerically by calculating the eigenvalues and the eigenvectors associated with a $(2N+1) \times (2N+1)$ matrix in each layer, where $2N+1$ is the number of harmonics
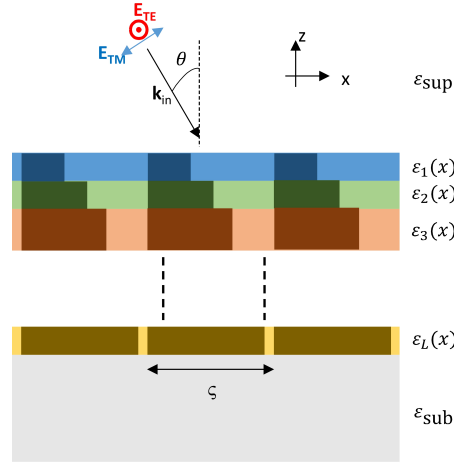
Figure 2.1 – Example of approximation of the permittivity function of a blazed grating in a RCWA approach. The grating would be decomposed in different layers, leading to a staircasing effect of the slope. Each layer l of the permittivity function ε_l is decomposed in Fourier harmonics.

(in general both propagating and evanescent) retained in the field expansions. The space harmonics of the tangential magnetic and electric fields in the lth grating layer are represented in terms of the calculated eigenvalues and eigenvectors. Different matrices are generated with TE or TM polarizations. The reflected and transmitted diffracted amplitudes are obtained by enforcing the boundary conditions at the boundaries between the grating layers. For surface-relief structures divided into L grating layers, this overall results in an additional $2(2N+1) \times (L+1)$ system of equations to be solved.

2.1.2 Finite differences in time domain

The finite differences in time domain (FDTD) method is one of the most popular methods in photonics because of its ability to handle a large variety of problems [182], including both periodic and non-periodic structures. This method is based on the explicit numerical solutions to Maxwell's curl equations.

In case of linear, nondispersive, homogeneous and isotropic media they can be expressed as:

$$\begin{cases} \nabla \times \boldsymbol{E} & = -\mu \frac{\partial}{\partial t} \boldsymbol{H} \\ \nabla \times \boldsymbol{H} & = \epsilon \frac{\partial}{\partial t} \boldsymbol{E} \end{cases}, \tag{2.2}$$

where $\boldsymbol{E}$ is the electric field, $\boldsymbol{H}$ is the magnetic field, μ is the magnetic permeability and ϵ is the electric permittivity of the medium. In case of zero conductivity, the derivative of the x-component of the electric field can be calculated as:

$$\epsilon \frac{\partial}{\partial t} \boldsymbol{E}_x = \frac{\partial}{\partial y} \boldsymbol{H}_z - \frac{\partial}{\partial z} \boldsymbol{H}_y. \tag{2.3}$$

The numerical solution of such equation is obtained by discretizing the space and time in the Yee cell, a discretized computational space where the electric field is calculated in the center of the faces of such cell whereas the magnetic field in the center of the edges:

$$\begin{cases} x & = i\Delta x \\ y & = j\Delta y \\ z & = k\Delta z \\ t & = n\Delta t \end{cases}. \tag{2.4}$$

Using this discretization, $\boldsymbol{E}_x$ at the position (i, j, k) at the time $t + \Delta t$ can be solved as:

$$\boldsymbol{E}_{x,(i,j,k)}^{t+\Delta t} = \boldsymbol{E}_{x,(i,j,k)}^{t} + \frac{\Delta t}{\epsilon_{i,j,k}} \left[\frac{\boldsymbol{H}_{z,(i,j+\frac{1}{2},k)}^{t+\frac{\Delta t}{2}} - \boldsymbol{H}_{z,(i,j-\frac{1}{2},k)}^{t+\frac{\Delta t}{2}}}{\Delta y} - \frac{\boldsymbol{H}_{y,(i,j,k+\frac{1}{2})}^{t+\frac{\Delta t}{2}} - \boldsymbol{H}_{y,(i,j,k-\frac{1}{2})}^{t+\frac{\Delta t}{2}}}{\Delta z} \right]. \tag{2.5}$$

Time domain methods such as FDTD can handle a variety of large systems as they do not require the solution of a linear system of equations, and can be coupled with other equations, such as the equation for the dynamics of population inversion in a laser [183]. However, they also face some challenges, like the implementation of dispersive materials or periodic boundary conditions for broadband sources at non-normal incidence [184]. Furthermore, the calculation of radiative fields is not straightforward compared to, e.g. the modal methods previously discussed, because FDTD assumes a finite computation window. In order to simulate open boundary conditions, perfectly matched layers (PMLs) are used; they are built from layers of lossy material with a perfectly matched interface that should not reflect a plane wave for any frequency, angle of incidence and polarization [185]. PMLs can be seen either as coordinate stretching in the frequency domain or as an artificial anisotropic absorbing medium.

2.1.3 Finite elements time domain

Within the work of this thesis I have also implemented simulations using the finite elements time domain method (FETD). This model solves the Maxwell's equations in time domain as FDTD. However, the domain is assumed to be discretized by a finite element method (FEM) mesh along triangular faces and their edges. In this case, the ordinary differential equations are yielded by Garlekin FEM [186]. In contrast to FDTD, the FETD mesh conforms to the structure and its size adapts locally. Thus, there is almost no dielectric averaging of the refractive indices at the interfaces. FETD is therefore especially useful for structures where the profile of the interfaces is very sensitive to variations (i.e. plasmonics or high index contrast structures) or in case of curved or slanted interfaces (i.e. ring resonators or slanted or sinusoidal gratings) [187]. In terms of computation effort, FDTD simulations provides faster results in case of low accuracy (i.e. $\Delta x < \lambda/15$) and FETD is instead faster in simulations where higher accuracy is

required.

2.2 Optimization of numerical simulations

The devices described in Chapters 3 and 4 have been simulated with the different numerical modeling: RCWA, FDTD, FETD and the surface integral equation (SIE) methods. Each of those numerical techniques has its own advantages and drawbacks, as described in details in the review of numerical methods in Section 2.1. In Section 2.2.1, I report the procedure I used to simulate periodic structures illuminated with a broadband source at an angle. In Section 2.2.2, I describe the possibility of calculating the field distribution with the in-house RCWA package.

2.2.1 Simulations with a broadband source at an angle

In order to characterize a structure consisting of a periodic repetition of the same unit cell, the structure was illuminated with a collimated broadband white light source ($\lambda = 400 - 800\,\text{nm}$) at an angle ($\theta_C = 6°$) and the integrated transmittance was measured every 0.5°, as shown in Fig. 3.11c in Section 3.1.2.

The same system was the simulated with Lumerical, an FDTD simulator, for which some issues regarding the periodicity of the unit cell were present. There are two periodic boundary conditions (BCs) which are normally used in FDTD simulations: the periodic BCs and the Bloch BCs. The periodic BCs are the least computational demanding but can be only used at normal incidence. However, for simulations at non-normal incident angles, a phase correction is needed between the fields at one edge and the fields at the other edge of the simulation region, as represented in Fig. 2.2a. This is implemented in the Bloch BCs:

$$\boldsymbol{E}\left(x \pm \Lambda_x\right) = \boldsymbol{E}\left(x\right) e^{\pm i\Lambda_x k_{\text{Bloch}}}, \tag{2.6}$$

where Λ_x is the simulation size in x-direction, and k_{Bloch} is the Bloch wavevector which is defined as the parallel component of a plain wave with wavelength λ_C tilted at θ_C. The Bloch BCs therefore require more memory and time than the periodic BCs (i.e. up to a factor of 2× for both memory and time). However, since these Bloch BCs create a constant wavevector for all the frequencies, they provide accurate phase correction only for the one wavelength (i.e λ_C), while the other wavelengths suffer from angle errors. In particular, the smaller wavelength-fields are injected at smaller angles, while higher wavelength-fields are injected at larger angles, as further illustrated in Fig. 2.2b:

$$\theta\left(\lambda\right) = \sin^{-1}\left(\frac{\lambda}{\lambda_C}\sin\theta_C\right), \tag{2.7}$$

where (θ_C, λ_C) are the injection angle and wavelength used for the Bloch BCs and $\theta\left(\lambda\right)$ is the actual propagation angle for a generic wavelength λ.
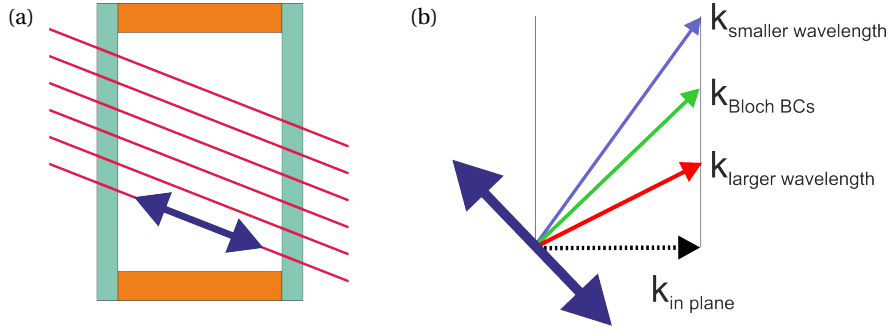
Figure 2.2 – (a) Schematic of a periodic simulation at an angle, where the tilted lines are the coherent wavefronts for the same wavelength. (b) Schematic showing the origin of the angle error for broadband source at an angle with Bloch BCs for wavelengths different than the one used for setting the Bloch BCs.

The expected angular error in this specific FDTD simulation was therefore ±2°, leading to an error of more than 30 nm in resonance spectral positions, according with the proposed analytical model (Eqs. (3.3) and (3.4)). To solve this issue, I set up an FDTD simulation using Lumerical which consisted of multiple simulations of narrowband ranges in order to cover the whole spectrum but avoiding the angular dispersion of Bloch boundary conditions.

Another option recently added in LUMERICAL is the broadband fixed angle source technique (BFAST), which allows to simulate a periodic structure with broadband source at an angle, without the need of having multiple simulations with wavelength swept [188]. This option is not only a BC, but a reformulation of the FDTD algorithm. However, these specific simulations were not converging with this method, due to the large unit cells and the materials dispersion.

The numerical results were then extracted in the far field region, in order to get an accurate estimation of the far-field steering angle of the system. However, even if the simulations were carried out with period structures and Bloch boundary conditions, the number of repetitions of the cell (m) in the evaluation of the far-field was a crucial parameter to optimize in order to include most of the scattered energy. In fact, the far-field extraction of a periodic FDTD simulation is evaluated as:

$$\boldsymbol{E}^{\text{far}} = \boldsymbol{E}_0^{\text{far}} \sum_m e^{i(k-k_{\text{Bloch}})m\Lambda_x},$$
(2.8)

where $\boldsymbol{E}_0^{\text{far}}$ is the far-field from a single period and Λ_x is the size of the simulation cell.

In order to match the simulations with the characterizations, the angular integration of the numerical results was performed, to create angular ranges with the same numerical aperture used in the characterizations (i.e. 0.5°):

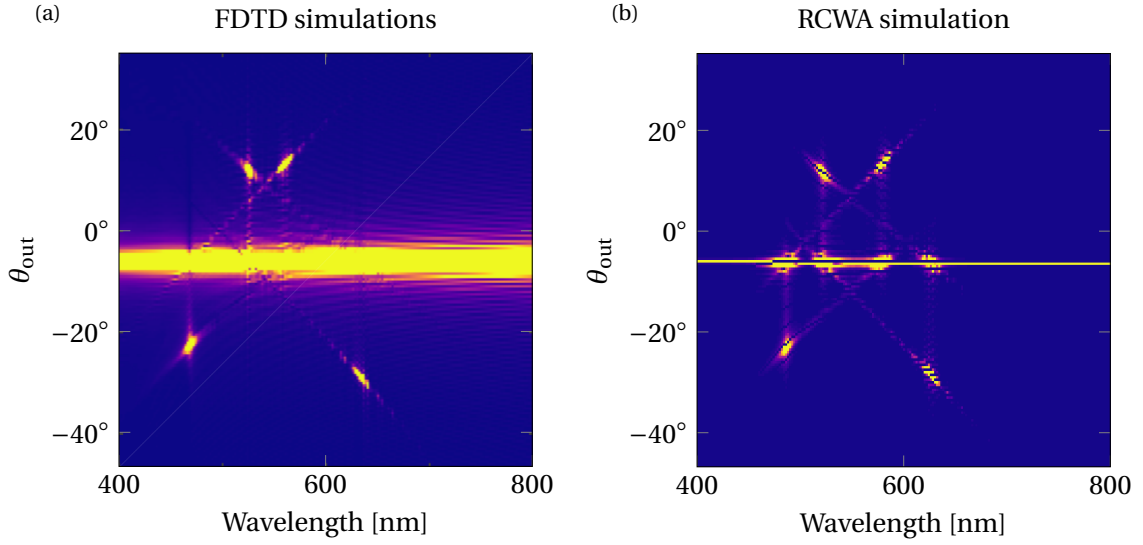$$\int_\theta E^2(\theta)\, d\theta.$$
(2.9)

Figure 2.3 – (a) FDTD and (b) RCWA simulations of the transmittance integrated every 0.5° for an array of unit cells with two adjacent RWGs (design #1), where the illumination is TE polarized and tilted by 6°, normalized to the illumination in air. The measurements and further details are reported in Fig. 3.11.

The LUMERICAL code for the far-field extraction and the angular integration is reported in Appendix A.1.

Afterwards, I simulated the same structure with RCWA. Since the unit cell was relatively large compared to the visible range (i.e. $L = 50\,\mu m$, as indicated in Section 3.1.2), hundreds of diffraction orders were considered. Therefore the simulation was easier to set than FDTD but was still computationally demanding. The maximum number of diffraction orders m propagating in free-space were evaluated considering the equation of a diffraction grating:

$$\max(m) \underset{\theta_2 \to \frac{\pi}{2}}{=} \left\lfloor (n_1 \sin\theta_1 - n_2 \sin\theta_2) \frac{\Lambda}{\lambda} \right\rfloor, \tag{2.10}$$

where θ_1 is the incident angle of the plain wave of wavelength λ in the medium with refractive index n_1 and θ_2 is the mth diffracted order in transmission (i.e. in the medium with refractive index n_2) or in reflection (i.e. $n_2 = n_1$).

The angular integration of the RCWA results was performed with the script provided in Appendix A.2, which converted the transmittance and reflectance from diffraction orders to angular ranges. A comparison of the simulations performed in FDTD and RCWA is reported in Fig. 2.3: it is possibile to observe that the FDTD far-dield distribution gives a broader angular spread for the zeroth order transmittance, therefore RCWA seems more suitable for far-field distributions.
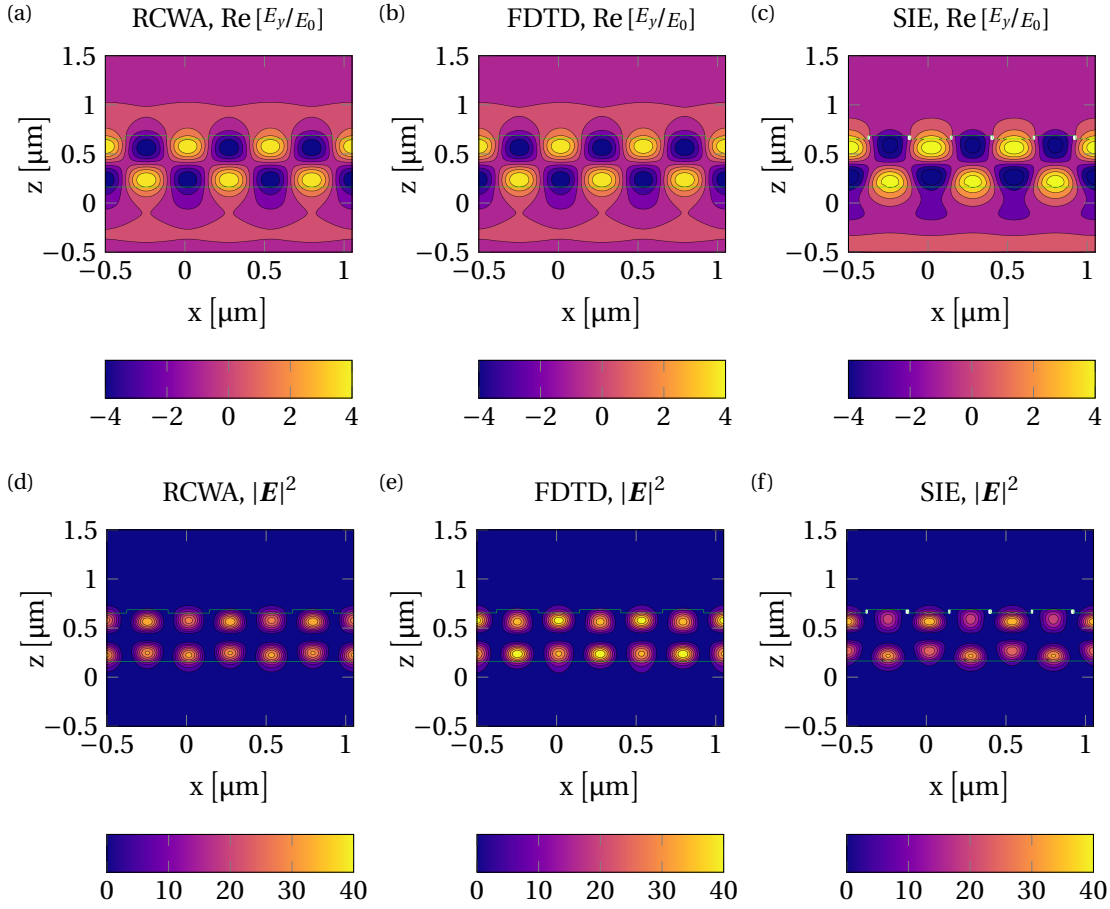
27

Figure 2.4 – Comparison of the coded function to evaluate the field distribution in RCWA (a,d) with already existing function for FDTD (b,e) and SIE (c,f). The structure has the same parameters used in Fig. 1.3e.

2.2.2 Calculation of the field distribution in RCWA

In this section the calculation to derive the electromagnetic field distribution with RCWA is reported, which I have implemented as MATLAB function. This function utilizes the capability of the RCWA tool used in-house to evaluate the full electromagnetic field (E and H vectors) in the substrate, in the superstrate, or in any intermediate stratum. The first step is to convert the electromagnetic field's frequency distribution into a spatial map for each grating layer. For example, in the case of the electric field the conversion is performed through the following equation:

$$\boldsymbol{E_s} = \sum_{m_1} \sum_{m_2} \mathscr{F}\mathscr{F}\boldsymbol{E}_{m_1,m_2} \cdot e^{2\pi i \cdot \left(\boldsymbol{f}_x x + \boldsymbol{f}_y y\right)}, \tag{2.11}$$

where $\mathscr{F}\mathscr{F}\boldsymbol{E}_{m_1,m_2}$ is the amplitude of the electric field for the Fourier order (m_1, m_2), $\boldsymbol{s} = \hat{e}_x x + \hat{e}_y y + \hat{e}_z z$ is the position vector being $\hat{e}_{x,y,z}$ the unit basis vectors and $\boldsymbol{f_x}$ and $\boldsymbol{f_y}$ are the field's grating-tangential spacial frequencies (i.e. parallel to $\hat{e}_x$ and $\hat{e}_y$, respectively). For the

free space propagation in the substrate or in the superstrate, Eq. (2.11) has to be expanded to include the terms $\boldsymbol{f_{z,t}}$ or $\boldsymbol{f_{z,r}}$, which are the transmitted or reflected field's grating-normal spatial frequencies (i.e. parallel to $\hat{e}_z$):

$$\boldsymbol{E_s} = \sum_{m_1} \sum_{m_2} \mathscr{FF} \boldsymbol{E}_{m_1,m_2} \cdot e^{2\pi i \cdot \left(\boldsymbol{f}_{z,t}z + \boldsymbol{f}_x x + \boldsymbol{f}_y y\right)}. \tag{2.12}$$

Once the electric and magnetic fields are computed, it is possible to directly plot the distribution of a specific component or the intensity. For example the electric field intensity is:

$$|\boldsymbol{E}|^2 := |\boldsymbol{E_s}|^2 = |\hat{e}_x E_x|^2 + \left|\hat{e}_y E_y\right|^2 + |\hat{e}_z E_z|^2, \tag{2.13}$$

where $\boldsymbol{E_s} = \hat{e}_x E_x + \hat{e}_y E_y + \hat{e}_z E_z$ is the electric field vector in spatial coordinates. I also included the possibility to make a movie with the time evolution of the electromagnetic field components, e.g. with the phase ϕ from $\phi = 0$ to $\phi = 2\pi$:

$$\mathrm{Re}\left(\hat{e}_z E_z \cdot e^{-i \cdot \phi}\right). \tag{2.14}$$

An example with the comparison of the coded function to evaluate the field distribution in RCWA with already existing function for FDTD and SIE is reported in Fig. 2.4. The reader can observe from the plots that all the three methods have a very good agreement in showing the electromagnetic field distributions for RWGs. I have chosen RCWA as the best tool for this purpose because, among those, RCWA is a method which is very appropriate for diffraction gratings and I have already used it in this thesis for evaluate the far-field and the diffraction efficiency.

Moreover, I have further extended such function to show also the absorption and the energy flux. It is possible to calculate the absorption (or dissipation) of energy using the equation derived by Landau et al. [189]:

$$Q = \frac{\epsilon_0}{4\lambda} \cdot \mathrm{Im}\left[\epsilon_r\right] \cdot |\boldsymbol{E}|^2. \tag{2.15}$$

The energy flux is instead defined as [190]:

$$\boldsymbol{S} = \frac{c}{8\pi} \cdot \mathrm{Re}\left[\boldsymbol{E} \times \boldsymbol{H}^*\right]. \tag{2.16}$$

2.3 Overview of fabrication techniques, implementations and materials for RWGs

Advances of RWGs have not only been boosted by increases in computational power and improved modeling algorithms as outlined in Section 2.1, but also thanks to the developments of several microfabrication and nanofabrication techniques. In particular, new mastering

techniques have provided microstructures and nanostructures of higher quality and with increased reproducibility and homogeneity, while replication and fabrication techniques have allowed higher throughput, lower costs and better accuracy from research and development to industrial production [191, 192]. In parallel, various characterization, metrology and quality control techniques have also been developed [193, 194]. Section 2.3.1 presents two origination techniques of gratings which have been used or considered for the work of this thesis: laser interference lithography, a standard process for periodic and uniform large areas, and electron-beam lithography, which is more suitable when the pattern is not uniform or homogeneous. The mastering of the grating usually includes the etching process to transfer the pattern of the photoresist into the substrate. The thin-film deposition techniques are discussed in Section 2.3.2. For high-throughput or cost-efficient requirements, the master grating is replicated by nanoimprint lithography (NIL) (Section 2.3.3).

2.3.1 Grating mastering and low-throughput fabrication techniques

Laser interference lithography

A very common technique for the manufacturing of periodic gratings larger than $1\,\text{m} \times 1\,\text{m}$ is holographic lithography [195], or laser interference lithography [196]. It is a technique based on recording the standing wave of an interference pattern between two or more coherent laser beams with a photoresist. The holographic exposure of such a thin photoresist layer allows the manufacturing of various grating structures, usually periodic and with sinusoidal or quasi-sinusoidal topographies. Note however that this approach is robust against misalignments and the development of the photosensitive material development is critical to achieve the desired grating profile and depth. Yet, this approach can be pushed to the extreme and it is possible to create sub-50 nm period patterns by using extreme ultraviolet holographic lithography at synchrotron radiation facilities [197].

Electron beam lithography

When non-periodic patterns or smaller patterns are required, the electron beam lithography is also a standard origination technique, typically affordable for samples up to a few cm^2 [198]. It is the preferred technique when the RWG pattern is not uniform or homogeneous [199]. Electron beam lithography allows to precisely control the duty cycle DC [200] and to achieve sub-10 nm grating lines [201, 202]. Since large patterns require the stitching of multiple deflection fields of an electron beam, stitching errors can create irregularities in the pattern. However, field stitching up to 100 nm have been shown not to degrade the RWG linewidth [203]. Recent developments for large-area electron beam exposure have reached exposure speeds of $1\,\text{min/mm}^2$ for non-tilted gratings with a 560 nm period [204], and $3\,\text{min/mm}^2$ for tilted gratings with a 200 nm to 500 nm period [179].

2.3.2 Deposition techniques

Deposition techniques such as chemical vapor deposition (CVD) [205], physical vapor deposition (PVD) [206], plasma deposition [207], atomic layer deposition (ALD) [208] or RF sputtering [209] allow the creation of waveguiding layers with high uniformity and accuracy, as well as multilayer stacks. It is critical for most applications to accurately control the deposition of the waveguiding layer(s), which define primarily the guided-mode effective index and therefore the resonance frequency. These techniques can be used both at wafer level and in high-throughput coating techniques such as roll-to-roll PVD, performed after roll-to-roll grating replications using nano imprint lithography (NIL). It is possible to fabricate a position variable RWG filter by sputtering a graded thickness waveguide [210]. An oblique angle layer deposition is suggested to improve the sensitivity of RWG sensors [211]. The deposition rate is also uneven and highly sensitive to experimental conditions [212].

2.3.3 Nanoimprint lithography

High resolution (sub-10 nm) NIL has been used for more than 20 years [213, 214] as a low-cost technique compatible with high-throughput manufacturing to replicate nanostructures [215]. Many different process flows and replication techniques are gathered under the name NIL. An example is the casting or coating of a sol-gel material on a PDMS soft-replica to replicate the structure on glass or thin-film polymer [216] after UV or thermal curing and annealing [217, 218]. Another widely used implementation is hot-embossing [219] based on a negative replication stamp made of nickel and various additives. For high-throughput replication of grating patterns, sheet to sheet and preferably roll-to-roll NIL or injection molding [220] techniques have been industrially applied [215, 221], especially for biosensing [87], optical security [181] and solar cells applications [222]. In order to improve the replication fidelity and to broaden the range of geometries and aspect-ratios that can be replicated, UV reticulation of liquid, gel or soft materials (UV-NIL) is preferred to hot-embossing techniques and gradually replacing them in many industries. Recent variations on NIL include stretchable molds to replicate the grating with the desired period [223, 224], multiple-mold replica NIL to reduce the grating depth [225], or doped NIL to fabricate RWG in one step without the need for any further deposition [226].

2.4 Optimization of MATLAB code and electron beam lithography for large area of tilted RWGs

In the scope of this thesis work I had to fabricate structures with the following requirements:

- portions of 1D gratings having:

    - different periods, i.e. from 200 nm to 600 nm;

- – different orientations, i.e. from 0° to 90°;

- pattern size of at least $1\,\text{cm}^2$;

- grating depth between 50 nm and 100 nm;

- compatible with nanoimprint lithography.

Due to the aperiodicity of those patterns, holography was not a suitable technique. Laser lithography was neither appropriate, because of the small feature sizes. Therefore, the only feasible techniques available were deep-UV lithography (DUV) [227] and electron beam lithography [228]. We decided to utilize the electron beam lithography, which provides a high resolution and flexibility in writing a high number of different patterns.

In this section I report the work performed to overcome many challenges for the fabrication of large area optical structures. In particular, I had to develop efficient MATLAB codes to generate dense and large lithographic layouts (as described in Section 2.4.1), and a procedure to speed-up the exposure by electron beam lithography with a customized pre-fracturing method (Sections 2.4.2 and 2.4.3).

2.4.1 Efficient MATLAB scripting for handling large structures

The most common file standard for electron-beam lithography and photolithography is the GDSII format, saved as `gds` file. The GDSII library, or database, format has become an important industry standard for the description of nanostructure designs that are fabricated with either photo or electron lithography.

Thus, I had first to create a suitable GDSII file containing the designed lithographic layout. The creation of such a file was particularly challenging because of the number of features: in a 5 in wafer there were more than 300 000 000 individual grating lines. The tool used in CSEM to create `gds` files was CLEWIN [229], however I quickly experienced issues because it is not optimized to design layouts with a huge number of elements.

To fulfill this goal I used instead MATLAB with the *GDSII Toolbox* developed by Ulf Griesmann [230], which allows creating, reading, and modifying files in GDSII library format. Other MATLAB toolboxes used were: the *Symbolic Math Toolbox*, the *Parallel Computing Toolbox* and the *Image Processing Toolbox*. This software combination was chosen because MATLAB is a very efficient tool for post-processing of numerical modeling results and for creating a lithographic layout as input for the fabrication process.

The first scripts I made were not taking advantage of the array reference (`Aref`) element of the GDSII format [231], and so each grating line was individually defined in the `gds` library. The
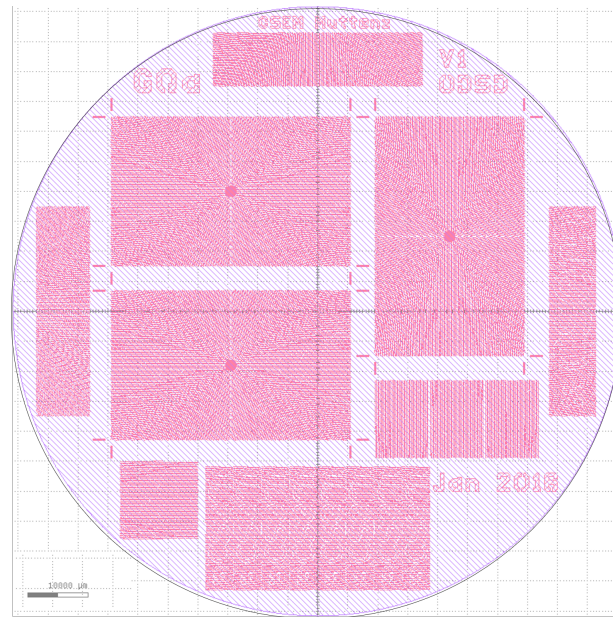
Figure 2.5 – Preview of a `gds` file with a lithographic layout comprising 15 different patterns on a 5 in wafer.

creation of those files was therefore very long: a file for a 5 in wafer with 15 tests (see Fig. 2.5) would initially required 5 days to be computed, with a size of about 5 TB on a workstation with $2 \times$ INTEL XEON E5630 processors. This code was not suitable because of the large size of the `gds` file that would have been challenging to process on the computer for the electron beam lithography, and the computation time was not affordable for debugging and making tests.

The `Aref` element is instead defined using only three data: the coordinates of the two reference axes of the coordinate system (which does not need to be Cartesian), the elementary structure of the array and the number of repetitions of such structure. Therefore, by implementing the `Aref` element, each grating period could be defined with one grating line and the number of its repetitions, and it could be called in many cells of the layout without the need of re-defining it. Moreover, I optimized the code to work with parallel computations. With these improvements, the computation of the same file took a few hours and was only 200 MB large. In the following, I report the part of the code related to the creation of an `Aref` element:

```matlab
arc = [0, 0; length_cell, 0; 0, -(height_cell/2-rem(height_cell/2,i/1000))];
adim.row = floor(height_cell/2/(i/1000));
adim.col = 1;
grat_A_str{i}=gds_structure([short_name,'_grat_A_',int2str(i)], ...
    gds_element('aref', 'sname',[short_name,'_line_A_',int2str(i)], ...
    'xy',arc, 'adim',adim));
```

where `length_cell` is the product of the number of grating lines and the grating period (i.e. L as defined in Section 3.1.1), `height_cell` is the length of each grating line and `i` is the grating period Λ.

The final important step towards code optimization was a sparing use of the symbolic equation solver (i.e. `S = solve(eqn,var)`). The solver was used to compute the intersection between a circle and an ellipse in order to determine the position of the center of each cell in the pattern (see Section 3.2.1 for further details). Since there was not an analytical solution, `solver` returned solutions containing `root`, which had to be approximated numerically using `vpa`. This process was initially computed for each cell in the pattern:

```
S = solve([(x/rad_a(j))^2 + (y/rad_b(j))^2 == 1,...
    (x-x_C)^2 + (y-y_C)^2 == (length_cell/2)^2+(height_cell/2)^2], [x, y]);
Px1 = double(vpa(S.x(1)));
Px2 = double(vpa(S.x(2)));
Py1 = double(vpa(S.y(1)));
Py2 = double(vpa(S.y(2)));
```

where `x`, `y` are the coordinates of the center of the cell to be determined, `rad_a`, `rad_b` are the semi-major and semi-minor axis of the ellipse having its center in (`x_C`,`y_C`) and `j` is the number of the current ellipse. The code was optimized by symbolically solving the roots of the equation before the main loop (i.e. line 1-2 of the code above), and by keeping the only numerical approximations in the loop:

```
Py1 = double(S.x(3));
Py2 = double(S.x(4));
Px1 = -sqrt(rad_a(j)^2-rad_a(j)^2/rad_b(j)^2.*Py1.^2);
Px2 = -sqrt(rad_a(j)^2-rad_a(j)^2/rad_b(j)^2.*Py2.^2);
```

In this way the required time to generate a full layout was less than 15 min. Further details of the scripting technique are presented in Sections 3.2 and 3.3.

2.4.2   Pre-fracturing technique

I used the electron beam lithography facility at CMI-EPFL, where I developed a process which allowed mastering of such structures. The core of this process consists of a pre-fracturing technique that converts each grating line into smaller stripes, which is described in the next section.

There are several steps which are required to expose a lithography layout with the electron beam. The first step is to convert the elements in the layout file to primitive shapes. Such operation is called *fracturing*. This is because the electron beam is capable of exposing only some specific kinds of shapes, which are encoded in the electronic control board of the pattern generator. In particular, for each shape the system generates a signal to control the deflection plates such that the electron beam is properly deflected to expose the whole primitive. The electron beam at CMI, the VISTEC Electron Beam EBPG5000ES, is capable of using both rectangles and trapezoids at any desired angle.

Once the layout has been fractured into primitives, each primitive shape has to be filled with individual electron beam shots. This operation is usually referred to as *shot filling*. Two important parameters to be considered for the shot filling are the beam step size (*BSS*, also
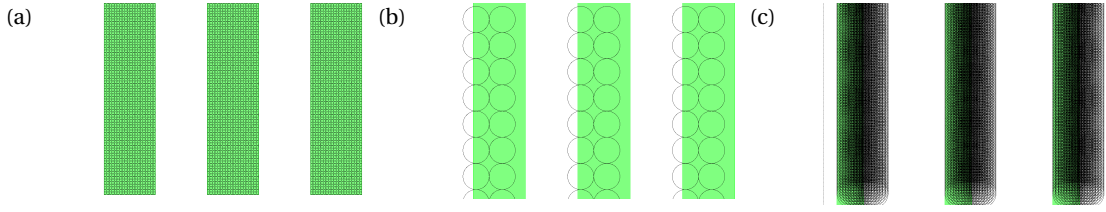
Figure 2.6 – Typical fracturing configurations of 1D vertical gratings ($\Lambda = 400\,\text{nm}$), with different combinations of beam size and beam step size. (a) $BSS = 10\,\text{nm}$, beam size = 10 nm. (b) $BSS = 100\,\text{nm}$, beam size = 100 nm. (c) $BSS = 10\,\text{nm}$, beam size = 100 nm, bias = $-50\,\text{nm}$.

defined as shot step) and the beam size (or spot size). The beam size depends on the current I used to generate the beam: the larger the current, the larger is the FWHM of the beam [19]. It is important to highlight that a given beam size does not imply that the final exposed and developed shot has the same size: the fabricated feature size is also related to the dose δ and to the development process; it can be tuned to be smaller or larger than the beam size.

There are many algorithms which are available for fracturing and shot filling, depending on the types of features in the layout. The frequency F at which the electron beam exposes the shots is related to the dose, beam current and the BSS [232]:

$$F\,[\text{MHz}] = 0.1 \cdot \frac{I\,[\text{nA}]}{\delta \left[\frac{\mu C}{\text{cm}^2}\right] \cdot BSS^2\,[\mu\text{m}]}. \tag{2.17}$$

The goal of a good electron beam optimization process is to find the best combination of parameters to maximize the exposure frequency. The pattern generator of the ebeam used at CMI supports a maximum frequency of 50 MHz.

Multiple combinations of beam step size and beam size can be adopted in the fracturing. Usually the fracturing of grating lines is performed by using a beam size as large as the BSS, as represented in Figs. 2.6a and 2.6b, provided a suitable dose and development time. In general, the larger the BSS and the beam size, the faster the exposure but the lower the quality and the resolution, because the grating lines get more rough. This edge roughness can sometimes degrade the optical performances. In those cases, a large beam size can be used in combination with a smaller BSS, in order to smooth the edge shape, as illustrated in Fig. 2.6c. A bias should also be applied in those cases to decrease the width of the grating lines for compensating the larger exposure due to the large beam size.

The fracturing is however more challenging when tilted grating lines have to be exposed, because the shot filling is performed on a square grid and the structures are tilted. Therefore, there are staircase issues for beam sizes and beam step sizes comparable to the width of the grating lines, which could also lead to underexposed and overexposed areas and thus to segmentation of the grating lines. This is illustrated in Fig. 2.7b. Therefore, the standard
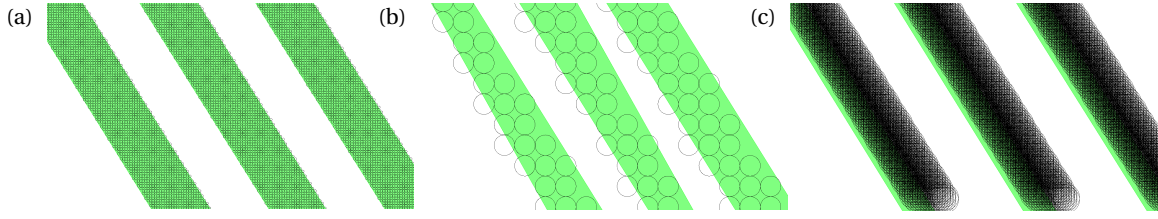
Figure 2.7 – Typical fracturing configurations of 1D gratings ($\Lambda = 400\,\text{nm}$) tilted by 32°, with different combinations of beam size and beam step size. (a) $BSS = 10\,\text{nm}$, beam size = 10 nm. (b) $BSS = 100\,\text{nm}$, beam size = 100 nm. This case suffers from staircase-issues and line-segmentation. (c) $BSS = 100\,\text{nm}$, beam size = 10 nm, bias = $-50\,\text{nm}$.

approaches to expose tilted gratings would be either to use a small beam size (i.e., 10 nm) and a small BSS (i.e., 10 nm) as in Fig. 2.7a, or to use a large beam size (i.e., 100 nm) with a smaller BSS (i.e., 10 nm) as in Fig. 2.7c. However, the two standard approaches suffer from other limitations related to the frequency and the exposure time of a large pattern as discussed in the following.

We chose to use the HSQ resist, which is a negative resist with a very high resolution and low line edge roughness. The dose required to expose the grating lines as in Figs. 2.7a and 2.7c has been found by a dose test to be around $750\,\mu\text{C/cm}^2$. Thus, the configuration as in Fig. 2.7a can be exposed with $I = 10\,\text{nA}$, $BSS = 10\,\text{nm}$ and $\delta = 750\,\mu\text{C/cm}^2$. Using Eq. (2.17), it is possible to evaluate the exposure frequency as $f \approx 13\,\text{MHz}$. Assuming to have a pattern density around 50 %, in $1\,\text{cm}^2$ there are about 5×10^{11} shots which are 10 nm far apart. Therefore, the required net time T_{exposure} to expose $1\,\text{cm}^2$ with that configuration is around $T_{\text{exposure}} = 5 \times 10^{11}/f \approx 11\,\text{h}$.

On the other side, the frequency required to expose the pattern fractured with the configuration as in Fig. 2.7c (i.e. with $I = 200\,\text{nA}$, $BSS = 10\,\text{nm}$ and $\delta = 750\,\mu\text{C/cm}^2$) is found to be around $f \approx 267\,\text{MHz}$, which exceeds the maximum frequency of the pattern generator and therefore that configuration is impossible to utilize with that instrument.

The configuration in Fig. 2.7b (i.e. with $I = 200\,\text{nA}$, $BSS = 100\,\text{nm}$ and $\delta = 750\,\mu\text{C/cm}^2$) would be exposed at $f \approx 2.7\,\text{MHz}$, and so the required net time to expose the 5×10^9 shots in $1\,\text{cm}^2$ would be approximately $T_{\text{exposure}} = 5 \times 10^9/f \approx 31\,\text{min}$. Thus, the pattern with a large beam size and a large BSS would be exposable in a very short time, however the quality would be very poor with staircase-issues and line-segmentation, as previously reported.

We therefore developed another special fracturing, which takes advantage of the large beam current (i.e. lower exposure time), of having a small BSS (i.e. higher fidelity and small line roughness) and has a feasible frequency and dose combination. In particular, we split each grating line into one or more smaller stripes in a pre-fracturing process, depending on the size of the grating period. Each stripe width is equal to the BSS used in the fracturing. The BSS used is, therefore, smaller than the beam size: for the purpose of this work we used a $BSS = 10\,\text{nm}$ and a beam size of about 100 nm (i.e. $I = 200\,\text{nA}$). In this way, it is possible to
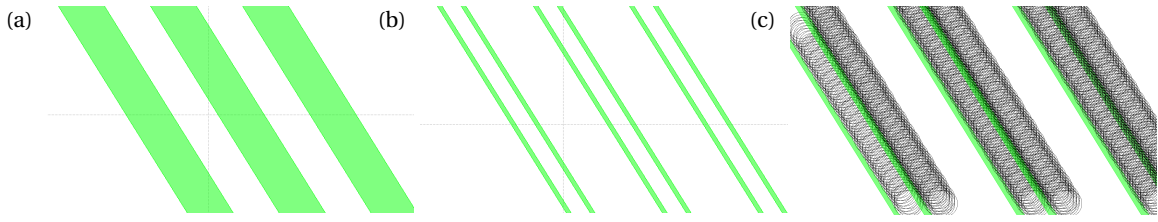
Figure 2.8 – Illustration of the developed pre-fracturing technique on a 1D grating ($\Lambda = 400\,\text{nm}$) tilted by 32°, which allows to expose tilted grating lines of many grating periods at any angle with higher lineshape fidelity and lower exposure time compared to the standard fracturing technique. (a) Initial grating. (b) Pre-fractured grating. (c) Pre-fractured, fractured and shot filled grating.

expose the pattern with a large electron beam while preserving enough accuracy to expose a large variety of grating periods and grating orientations. This pre-facturing process is illustrated in Fig. 2.8. In this case, the required dose is larger than the standard range, because the thin stripes have to be over-exposed in order to reach a width of about the beam size. The fracturing has then been performed using the standard large rectangles and fine trapezoids technique (LRFT) [233].

After some dose tests, we found that a good dose density was about $\delta = 7500\,\mu\text{C/cm}^2$, giving a frequency of about $f \approx 27\,\text{MHz}$. This value is reasonable since the stripes are about 10 times thinner than the grating lines. In this case there are 10 times fewer shots than in the configuration of Fig. 2.7a, i.e. 5×10^{10} shots. Therefore, the required net time to expose $1\,\text{cm}^2$ is about $T_{\text{exposure}} = 5 \times 10^{10}/f \approx 31\,\text{min}$. This pre-fracturing technique thus allows to efficiently expose the pattern at the same speed as in Fig. 2.7b but having a much higher lineshape fidelity and being more robust for multiple grating orientations.

Since the estimated frequency is about half of the maximum frequency available, I made later improvements of this pre-fracturing technique by creating stripes which are twice the *BSS*. In this way, the pattern can be exposed with twice the frequency in almost the same amount of time and the lineshape and the robustness for the fracturing at any angles was further improved because of the reduced BSS. Further details are reported in Section 2.4.3.

However, some other considerations have to be done regarding the exposure time. The total exposure time (T_{total}) does not only include the net exposure time T_{exposure} calculated in the previous examples, but also the settling time T_{settling} [204]:

$$T_{\text{total}} = T_{\text{exposure}} + T_{\text{settling}}. \tag{2.18}$$

Such settling time corresponds to the overhead time that includes mainfield, subfield settling times, pattern generator overhead and beam blanker [234]. In the fabricated layouts, the overhead time was actually the limiting parameter, mainly due to the mainfield settling and due to the very large pattern, as discussed in the following.
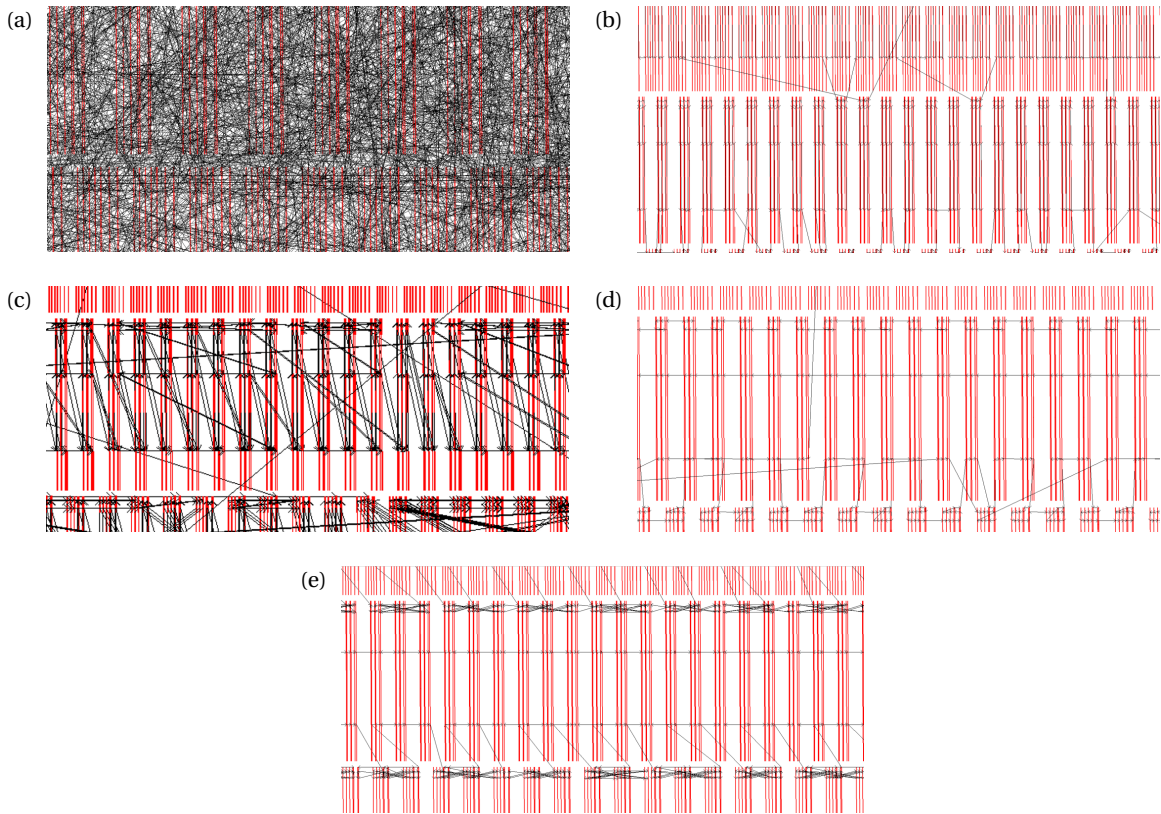
Figure 2.9 – Several writing order techniques have been simulated on the design #6, which is 1 cm × 1 cm large. The black lines and arrows show the order of exposure of the different primitive shapes. (a) Random: $T_{\text{settling}} = 7\,\text{h}\,14\,\text{min}$. (b) Follow Geometry: $T_{\text{settling}} = 5\,\text{h}\,24\,\text{min}$. (c) Array Compaction: $T_{\text{settling}} = 4\,\text{h}\,36\,\text{min}$. (d) Writing Order: $T_{\text{settling}} = 2\,\text{h}\,40\,\text{min}$. (e) Subfield Compaction: $T_{\text{settling}} \approx 2\,\text{h}\,30\,\text{min}$.

The optimization of T_{settling} has been performed by tuning the *writing order*: once the pattern has been fractured and the position of the shots has been determined, the writing order has to be determined. In particular, the beam exposes all the primitive shapes within a field before moving to the next one. However, the order of exposure of the primitives is not encoded by default in the pattern generator and has to be assigned in advance during the fracturing process. In BEAMER (by GENISYS), the software I used to perform the fracturing, several writing order algorithms are available [235]. In principle the best order is the one that minimizes the movement of the electron beam between different primitives, because during this movements the electron beam is blanked. As shown in figure Fig. 2.9, I simulated different writing orders and used the fastest one for these types of layouts, which was the *Subfield Compaction*.

By considering both the net exposure time and the settling time, the total estimated time for $1\,\text{cm}^2$ was found to be around $T_{\text{total}} \approx 3\,\text{h}$. The actual fabrication of the design #6 took about $5\,\text{h/cm}^2$, which is still much shorter than what would have been achieved with the conventional fracturing technique of Fig. 2.7a, estimated to take between $15\,\text{h/cm}^2$ to $25\,\text{h/cm}^2$.
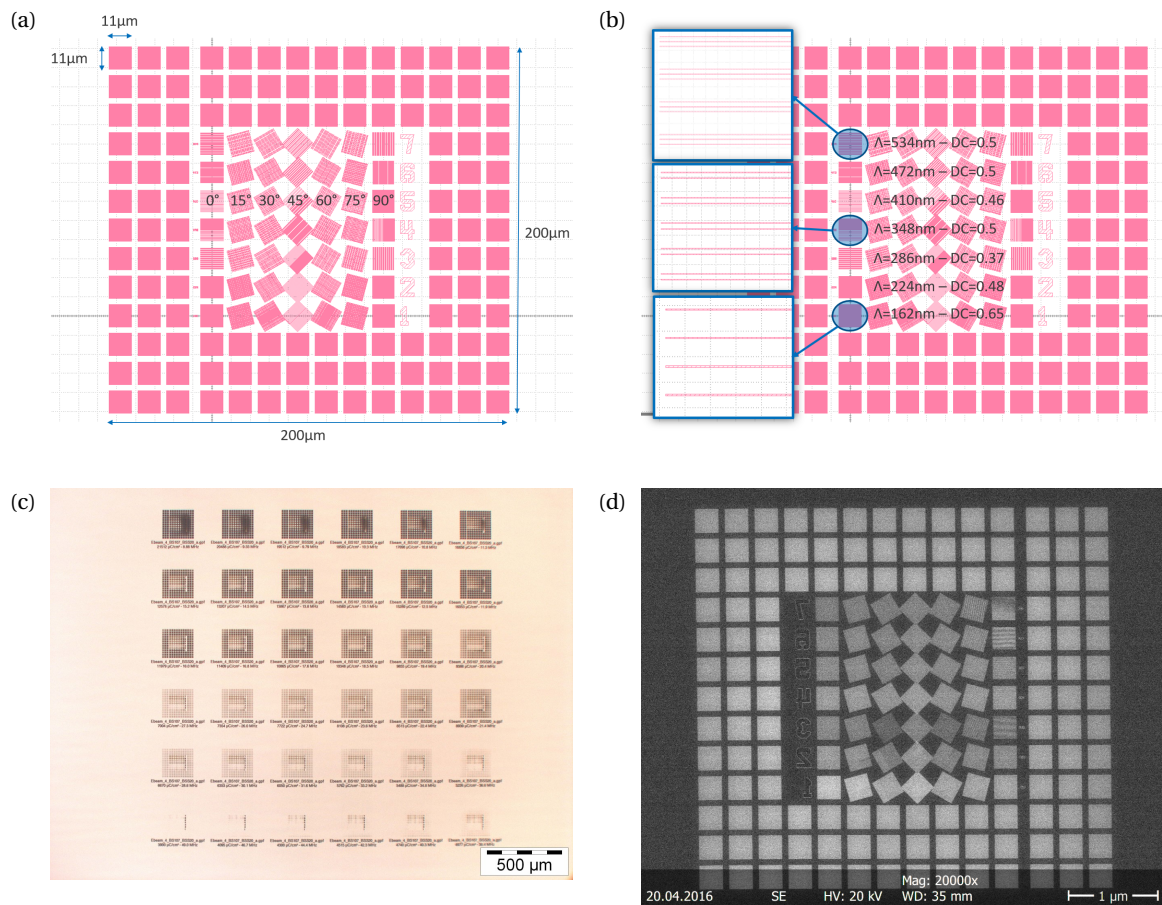
Figure 2.10 – Lithographic layout, microscope and SEM images of a dose test, varying the dose from $\delta = 3900\,\mu\text{C/cm}^2$ to $\delta = 21\,512\,\mu\text{C/cm}^2$, with 5 % increments. (a,b) Lithographic layout. (c) Microscope picture with different dose tests. (d) SEM overview ($\delta = 6353\,\mu\text{C/cm}^2$).

2.4.3 Characterizations and procedures

I included the pre-fracturing technique described in the previous section in the MATLAB script used to create the gds files in order to automatically generate pre-fractured gds file with grating lines split into thinner stripes. Afterwards, several fabrication tests have been performed for the final tuning of the many parameters related to the electron beam lithography step.

The first type of tests aimed at finding the correct dose range. Thus, I created a test pattern with many grating periods (from 162 nm to 534 nm) and tilted in many directions (from 0° to 90°). The largest gratings were created with three stripes, and the smallest grating with one stripe only. The test pattern included an outer region with other dummy gratings to compensate the proximity effect. The pattern was then exposed at different doses in order to find the best dose that could properly expose all the gratings. The lithographic layout, as well as microscope and SEM images are shown in Figs. 2.10 and 2.11.

Grating period [nm]	Number of stripes	Stripe width [nm]	Stripe gap [nm]
$150 < \Lambda < 230$	1	22	0
$230 < \Lambda < 250$	1	33	0
$250 < \Lambda < 270$	2	22	20
$270 < \Lambda < 300$	2	22	30
$300 < \Lambda < 350$	2	22	50
$350 < \Lambda < 450$	2	22	80
$450 < \Lambda < 500$	3	22	60
$500 < \Lambda < 600$	3	22	80

Table 2.1 – Parameters for the pre-fracturing technique, used in combination with $BSS = 10\,\text{nm}$, $I = 200\,\text{nA}$ (beam size $\approx 100\,\text{nm}$), and HSQ004 resist.

Step	Process	Parameters
1	Plasma cleaning	O_2, 400 mL/min, 500 W, 4 min
2	Substrate cooling	1 min
3	HSQ coating	HSQ004, 3000 rpm
4	Resist exposure	$BSS = 10\,\text{nm}$, $I = 200\,\text{nA}$, $\delta = 7500\,\mu\text{C/cm}^2$
5	Resist development	2 min in TMAH 25%
6	Substrate rinsing	In DI until $R > 12\,\text{M}\Omega$
7	Substrate drying	N_2 drying

Table 2.2 – Process for the electron beam lithography of large-scale grating patterns with periods at many angles on a Si wafer.

Once the dose was determined, I performed several tests to tune the pre-fracturing technique. In particular, I varied the distance between the stripes and the number of stripes across a variety of grating periods and I analyzed the SEM images though a MATLAB script that I coded to automatically detect the pattern with the closest duty-cycle to the desired one. An example is reported in Fig. 2.12.

Finally, I performed some finer dose tests with a small part of the actual pattern, in order to take into account the proper pattern density. We decided not to perform the proximity-effect correction because of the large and uniform area, so that the exposure was not further slowed down.

I report in Table 2.1 the tuned parameters for the pre-fracturing technique. The process flow for the electron beam lithography is given in Table 2.2. These parameters and steps have been used to realize the demonstrators in Chapter 3. The developed resist had enough adhesion with the Si wafer and the right depth, such that an etching step was not required: it was possible to use it for making replicas as Ni shims by galvanic growth or on glass substrates by NIL.

Furthermore, I describe in the following the work done for mastering the gratings used in Chapter 4. In this case I kept a standard fracturing technique as in Fig. 2.6a since the grating

Step	Process	Parameters
1	Plasma cleaning	O_2, 400 mL/min, 500 W, 4 min
2	Substrate cooling	1 min
3	ZEP coating	ZEP 50 %, 3000 rpm
4	ZEP baking	180° for 5 min
5	Resist exposure	$BSS = 20$ nm, $I = 50$ nA, $\delta = 250\mu$C/cm^2
6	Resist development	1 min in Amyl-Acetate
7	Substrate rinsing	1 min in 90:10 MiBK:IPA
8	Substrate drying	N_2 drying
9	Substrate etching	Slow dry etching at 0°
10	Resist stripping	O_2, 400 mL/min, 500 W, 4 min

Table 2.3 – Process for the electron beam lithography and etching of vertical 1D gratings in a Si wafer. The etching time is reported in Fig. 2.13.

lines were all oriented vertically. However, since the pattern was etched in the Si wafer, I used the positive ZEP resist because of its higher dry etching selectivity [236]. The etching machine used was Alcatel AMS 200 SE, an optimized Deep Reactive Ion Etching (DRIE) system for Si and SOI wafers. Because I needed to have different grating depths (i.e. from 5 nm to 250 nm), I tested several etching times. The related process flow is reported in Table 2.3, and the analysis of grating depth vs etching time is shown in Fig. 2.13.
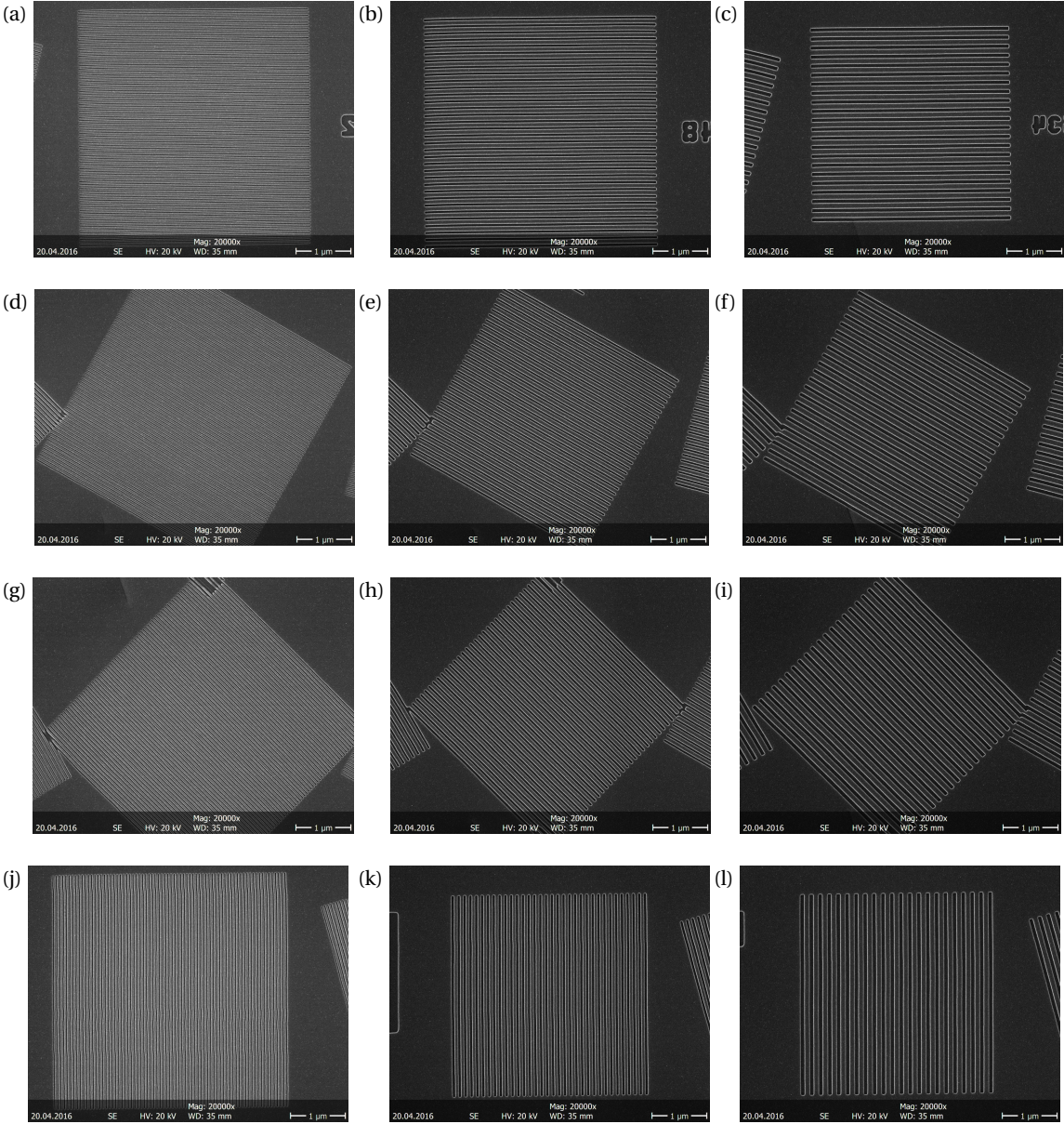
Figure 2.11 – SEM images of several gratings with different combinations of periods Λ and angles Ψ exposed at the same dose ($\delta = 6353\,\mu C/cm^2$). Periods Λ, from left to right: 162 nm, 348 nm, 543 nm. Angles Ψ, from top to bottom: 0°, 30°, 45°, 90°.

(a)

(b)

Figure 2.12 – Example of a performed test to tune the pre-fracturing technique, i.e. for finding the best number of stripes and the best distances between them across the different gratings. (a) SEM image. (b) Analysis of the duty-cycle vs stripes distances.

Figure 2.13 – Etching time vs grating depth.

2.5 Conclusions

The advanced developments of RWGs carried out in this thesis have required improvements in both simulations and fabrications methods. Resonant waveguide gratings are optical structures which are very sensitive to some fabrication steps, e.g. the thick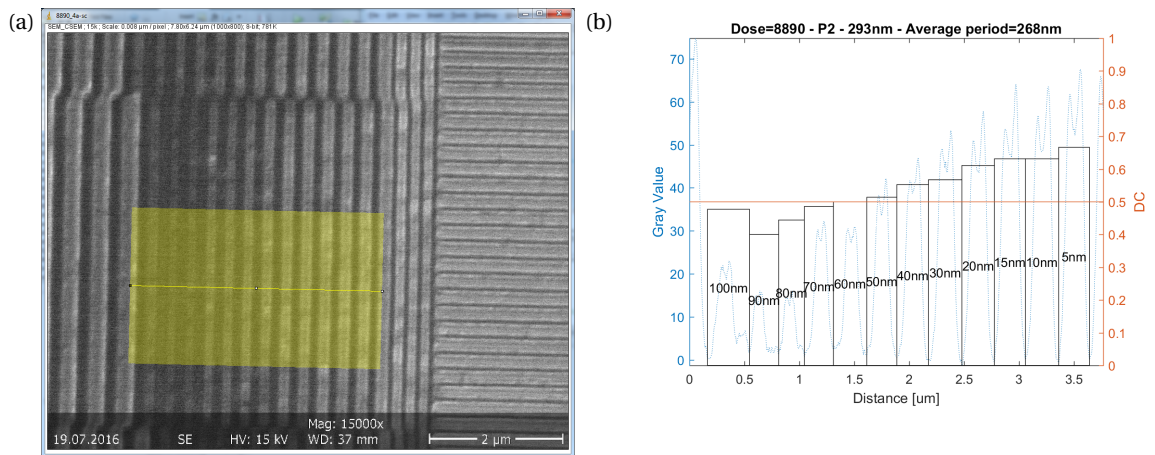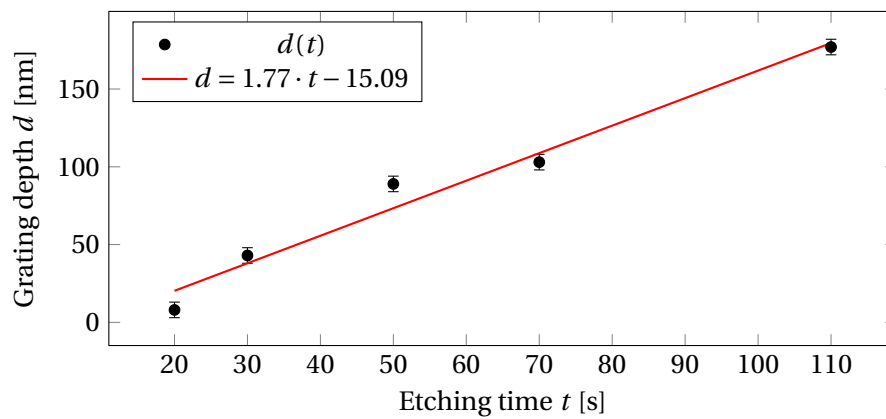ness of the waveguide layer or the grating depth. Thus it is important to have good agreements between simulations and fabrications and to be able to predict and, eventually, account for some of the fabrication deviations. Some of the developed simulation methods, such as the simulations with a broadband source at an angle or the plot of the electromagnetic field distributions, have been crucial in this thesis to assure a good prediction of the outcoupled angle, as explained in details in the next chapters. Moreover, the optimization of the electron beam lithography has been a fundamental step to guarantee a feasible fabrication of such elements, that would not had been possible to produce without the work presented in this chapter. In particular, a pre-fracturing of the grating lines in one or more smaller stripes, depending on the grating period, is first implemented, followed by the fracturing using a beam step size smaller than the beam diameter. This method is beneficial to efficiently fabricate gratings with different periods and oriented at different angles. Further improvements in the exposure time could be achieved by means of advanced electron beam configurations, such as a variable shape beam or a multi column beam [237, 238], or by direct laser writing with deep or extreme ultraviolet light [239].

3 Paired impedance matched RWGs: light filtering and redirection

Part of the results presented in this chapter were published in:

- G. Quaranta, G. Basset, O. J. F. Martin, and B. Gallinet, "Color-Selective and Versatile Light Steering with up-Scalable Subwavelength Planar Optics", ACS Photonics **4**, 1060–1066 (2017).

- G. Quaranta, G. Basset, Z. Benes, O. J. F. Martin, and B. Gallinet, "Light refocusing with up-scalable resonant waveguide gratings in confocal prolate spheroid arrangements", Journal of Nanophotonics **12**, 016004 (2018).

- G. Quaranta, G. Basset, O. J. F. Martin, and B. Gallinet, "Steering and filtering white light with resonant waveguide gratings", Proc. of the SPIE **10354**, 1035408 (2017).

My contributions were: designing and fabricating the samples, measuring them, analyzing the data, scripting the simulations, preparing the figures and writing the papers. The co-authors edited the manuscripts and contributed to the discussion of the results together.

In Section 3.1, the properties of the unit cell that is used in the whole chapter is described. In Section 3.1.2, the cell is repeated periodically with no gap between cell so that it forms a grating with a period equal to the cell length. In Section 3.2, a more complex design method is proposed, in which the cell is repeated on a surface with different periods, spacing and orientations so that a point light source is filtered and refocused to an observation point. Realizations as optical document security labels with smartphone authentication are provided. Conclusions and outlooks are given in Section 3.4.

3.1 Properties of paired-RWGs

In this section I introduce the properties of an optical system whose unit cell is composed of two finite-size and impedance matched RWGs. In Section 3.1.1, I describe the work done for
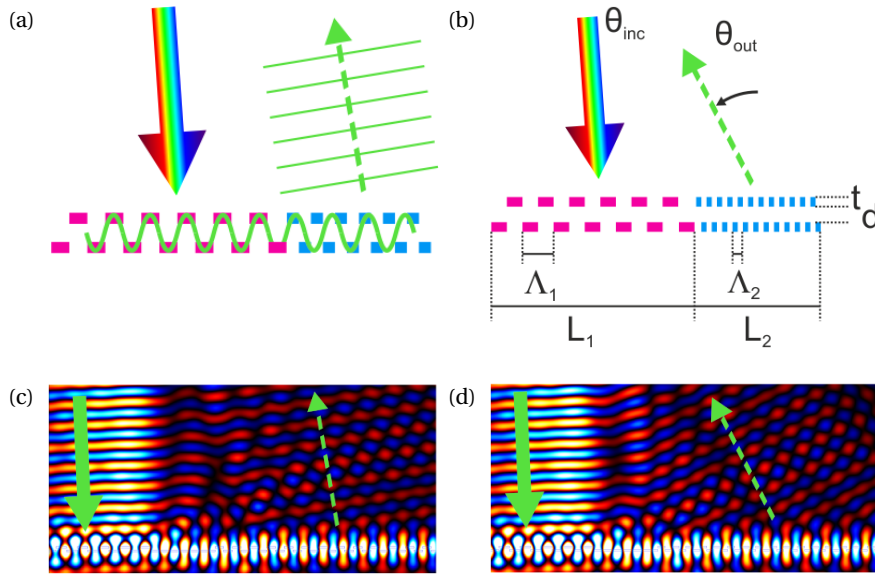
Figure 3.1 – Schematic of a single unit cell showing the redirection in reflection. (a) Corrugated ultrathin waveguide coats a first and a second adjacent gratings, schematized in pink and blue, respectively. A specific wavelength range is in-coupled inside the waveguide by the first grating from a white incident light beam, and out-coupled from the second grating. (b) By changing the period of the second grating, it is possible to out-couple the light at a different in-plane angle. (c) and (d) Corresponding amplitude of the transversal near-field obtained with FDTD simulations.

the physical understanding and the modeling of a single isolated unit cell. In Section 3.1.2 I analyze the optical properties of a periodic array of the same cell.

3.1.1 Isolated paired-RWGs: physics and modeling

A typical schematic of an isolated paired-RWG is shown in Figs. 3.1a and 3.1b: two RWGs with periods Λ_1 and Λ_2 and lengths L_1 and L_2 are coupled together. Both resonant gratings share a thin high-refractive index (HRI) guiding layer, where the corrugated waveguide thickness t and the modulation depth d of the supporting grating are well below the wavelength. Furthermore, for simplicity, we chose to have $L_1 = L_2$ in order to have the boundary between the two RWGs in the center of the unit cell. However, it is possible to customize the ratio between L_1 and L_2 to enhance the efficiency of the structure, that is, the grating responsible for in-coupling could be longer than the grating for out-coupling.

The broad-band light source incident on the first RWG can be partly coupled into leaky guided modes when the impedance matching of the propagation wave vector is fulfilled [61, 89]. For TE-polarization and using the orientation of Fig. 1.2, the wave impedance Z_{TE} of the system
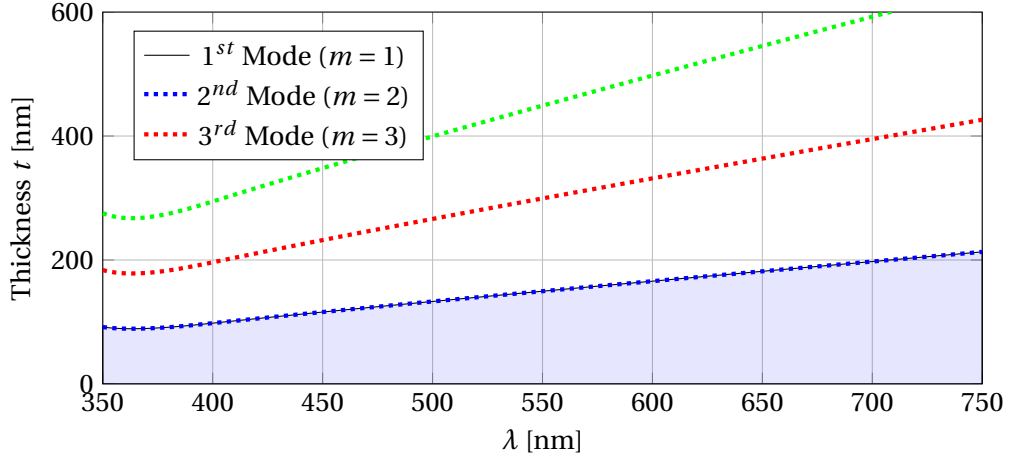
Figure 3.2 – Cut-off conditions for a symmetric dielectric slab waveguide (ZnS [243] as waveguide material, Ormocomp [244] as cladding material). The fundamental mode (TE_0 or TM_0) has no cut-off thickness. The filled blue region is the single mode regime.

can be defined as the ratio of the transverse electric and magnetic field [240]:

$$Z_{TE} = \frac{E_y}{H_z} = \frac{-E_z}{H_y} = \frac{\omega\mu}{\beta},$$ (3.1)

where $\omega = \frac{2\pi c}{\lambda}$, μ is the permeability of the medium, λ is the wavelength of light in vacuum c is the speed of light and β is the propagation constant defined in Eq. (1.2). Thus, for fixed wavelength λ, materials and waveguide thickness t, two RWGs are impedance matched if the propagation constant, or analogously the angles of propagation (θ_m, ϕ_m) reported later in Eq. (3.4), are the same. By reciprocity, the coupled modes propagating in the second RWG can be out-coupled. Since the RWG has a finite-length L_1 the coupled modes have a spectral band whose width depends on the grating length [241].

Various modes can propagate in the waveguide layer in different directions. Specifically, we demonstrate devices using very thin corrugated waveguides allowing only a few waveguide modes in the visible range. The cut-off condition for symmetric ($n_{sub} = n_{sup} = n_{clad}$) dielectric slab waveguides [242] can be used to determine the number of allowed waveguide modes m in such a system:

$$t_{\text{cut-off},m} = \frac{m\lambda}{2\sqrt{n_{\text{core}}^2 - n_{\text{clad}}^2}}.$$ (3.2)

For color-selective applications, it is important to have RWGs that support only the fundamental mode, in order to enhance the color purity. An example of the cut-off thicknesses for the first waveguide modes is shown in Fig. 3.2, where the blue shaded region represents the single

mode regime.

The coupled leaky modes propagate in the first and later second RWG with a field distribution that extends into the cladding. Moreover, the guided propagation is similar to the propagation in a noncorrugated waveguide having the same thickness t. Since the second RWG has the same corrugated thickness t, both RWGs are almost impedance matched and there are low losses at their interface.

The direction of the outcoupled modes differs from the direction of the incoming light because the periods of the two RWGs are different. It is possible to tune the direction of the out-coupled modes by changing the period of the second RWG, as represented in Fig. 3.1b in the in-plane regime [245]. The system works also in conical regime, as detailed later in this section.

For binary RWGs as in the case here or sinusoidal RWGs, the leaky-guided modes are out-coupled in both reflection and transmission at the same angle and almost the same efficiency. Since operation for such a device is usually in reflection, we omit in Fig. 3.1 the light transmitted downward. It should be mentioned that, in general, different spectral portions of the light source can be in-coupled into the second RWG, and be out-coupled from the first RWG.

This structure supports only strong resonances for the light polarized transverse electric (TE), with the electric field parallel to the y-axis in Fig. 3.1c. The efficiency of the resonances for the orthogonal, transverse magnetic (TM) polarization are negligible compared to those of TE modes in case of corrugated thin-film waveguides [246, 247] and close to normal incidence. It is however possible to extend this concept to thicker waveguides, to efficiently allow the operation in both polarizations.

A very useful analytical model to describe the process of in-coupling and out-coupling for this structure is here calculated, based on the impedance matching condition for a slab waveguide [240]. The model is valid when both the modulation depth d and the waveguide thickness t are well below the wavelength, such that the propagation behavior of the leaky modes can be modeled as propagation in a noncorrugated waveguide. The model becomes inaccurate when t, d are comparable to the effective wavelength. We use this model to predict the grating periods (Λ_1 or Λ_2, respectively) that are needed to in-couple and to out-couple from the waveguide a central wavelength λ, using the angles of incidence and out-coupling given in polar and azimuthal angles in the cladding material, ($\theta_{\text{in}}, \phi_{\text{in}}$) and ($\theta_{\text{out}}, \phi_{\text{out}}$), the refractive index n_{clad} of the low-refractive index material (waveguide cladding), the refractive index n_{core} of the HRI material (waveguide core):

$$\tan\left(\frac{\pi}{\lambda} \cdot n_{\text{core}} \cdot \sin\theta_m - m\frac{\pi}{2}\right) = \begin{cases} \dfrac{\sqrt{n_{\text{core}}^2 \cdot \cos^2\theta_m - n_{\text{clad}}^2}}{n_{\text{core}} \cdot \sin\theta_m} & \text{for TE Modes} \\[3ex] \dfrac{n_{\text{core}}\sqrt{n_{\text{core}}^2 \cdot \cos^2\theta_m - n_{\text{clad}}^2}}{n_{\text{clad}}^2 \cdot \sin\theta_m} & \text{for TM Modes} \end{cases} , \quad (3.3)$$

where θ_m is the internal angle of propagation in the slab waveguide and m is the waveguide propagation order. The angle θ_m is related to the in-coupling and out-coupling angles through the grating equation:

$$
\begin{cases}
k_{x_{\text{in,out}}} = \dfrac{2\pi}{\lambda} \cdot n_{\text{clad}} \cdot \sin\theta_{\text{in,out}} \cdot \cos\phi_{\text{in,out}} - i\,\dfrac{2\pi}{\Lambda_{1,2}} \\[2mm]
k_{y_{\text{in,out}}} = \dfrac{2\pi}{\lambda} \cdot n_{\text{clad}} \cdot \sin\theta_{\text{in,out}} \cdot \sin\phi_{\text{in,out}} \\[4mm]
\qquad \Longrightarrow \begin{cases}
\theta_m = \tan^{-1} \dfrac{\sqrt{k_{x_{\text{in,out}}}^2 + k_{y_{\text{in,out}}}^2}}{k_{z_{\text{in,out}}}} \\[4mm]
\phi_m = \tan^{-1} \dfrac{k_{y_{\text{in,out}}}}{k_{z_{\text{in,out}}}}
\end{cases}
\end{cases}
\qquad . \tag{3.4}
$$

The angle (θ_m, ϕ_m) has to be the same for both the in-coupled and out-coupled waves in order to respect the impedance matching condition between both RWGs building the unit cell. To enhance the efficiency of this unit cell and to work with substantially subwavelengths thickness structures, we set $i = \pm 1$. Furthermore, we use the fundamental waveguide mode $m = 0$, such that a very thin waveguide layer can be used and supports only one propagating mode, thus, enhancing the color-purity of the device.

An infinitely long RWG would filter the spectrum of the leaky mode toward monochromatic RWG modes. For finite RWGs, the bandwidth of the in-coupled spectrum depends on the number of grooves [241] and is not limited to this central wavelength.

Figure 3.3 shows the spatial dispersion graph for a typical unit cell for TE polarization, where the incoming light is at in-plane incidence (i.e., $\phi_{\text{in}} = 0$). The details of the design are reported in Appendix B. When we change the polar angle of incidence (i.e., in-coupling angle θ_{in}) we observe a variation of the out-coupled light, both in its spectrum and direction. We notice in Fig. 3.3 up to four different peaks (in the visible spectrum for this configuration). Indeed, it is possible to incouple light from each of the two gratings and from both the $i = +1$ and the $i = -1$ diffracted orders. We notice that the spatial dispersion lines form pairs of symmetric lines with respect to the $\theta_{\text{in}} - \theta_{\text{out}}$ axis. This symmetry is related to the k-space symmetry of the system, when both gratings are exchanged and illuminated from the opposite angle $-\theta_{\text{in}}$. Let us note that the data reported in Fig. 3.3 are valid both in reflection and transmission.

.

The dashed lines in Fig. 3.4a represent the dispersion of the first diffraction order of the RWGs in the limit cases where $\theta_{\text{in}} = \pm 90°$ or $\theta_{\text{out}} = \pm 90°$, red for the first grating (responsible for in-coupling the incident light) and blue for the second one (responsible of the out-coupling process). By changing the angle, the slope of the diffraction lines changes and they can intersect the dispersion curves of the waveguide, allowing the in-coupling/out-coupling of
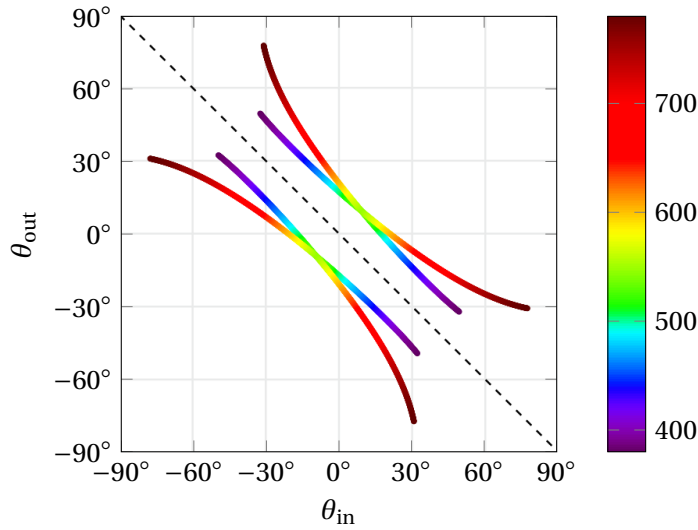
Figure 3.3 – Spatial dispersion graph obtained with the analytical model (Eq. (3.3)) for a typical unit cell (design #1) showing the in-coupling θ_{in} and the out-coupling θ_{out} angles. It is possible to in-couple the light from both RWGs and from both diffracted orders that can be supported ($i = +1$) by each RWG (colorbar in [nm]).

specific spectral ranges at given angles. The same information is highlighted in Fig. 3.4b, in terms of angular relation of the in-coupling and the out-coupling beams. By engineering different combinations of periods and orientations of the unit cells, it is possible to obtain the redirection of a beam for a specific color at any desired angle. For example, in Figs. 3.4c and 3.4d the angular dispersion graphs of the same unit cell but with different Λ_1 are reported, to show the versatility of the system.

From Eq. (3.4) the reader may deduct that the unit cell can work both in the in-plane regime (i.e. when the incoming light is oriented perpendicular to the grating lines) and in the fully conical regime (i.e. when the incoming light is parallel to the grating lines), or in any intermediate position. The beam redirection behavior is illustrated with two different graphs: the dispersion plot and the angular plot, represented in Fig. 3.4 for a typical unit cell (design #2, reported in Appendix B).

In order to understand better the properties of conical diffraction, I created a MATLAB script which allows visualizing conical diffraction of a 1D grating and to evaluate the angles of diffraction. The script was especially helpful to understand Eqs. (3.3) and (3.4) in the case of conical incidence. A screenshot of the GUI for this script is displayed in Fig. 3.5.

As direct consequence, I verified that the two gratings of a cell do not necessarily need to be aligned in the same direction, but they can have the grating vectors oriented in different ways. In Fig. 3.6 I report as example two configurations with different angles and periods of the second grating so that the same spectral portion can be in-coupled from the same direction (θ_{in},ϕ_{in}) and out-coupled to the same direction (θ_{out},ϕ_{out}).
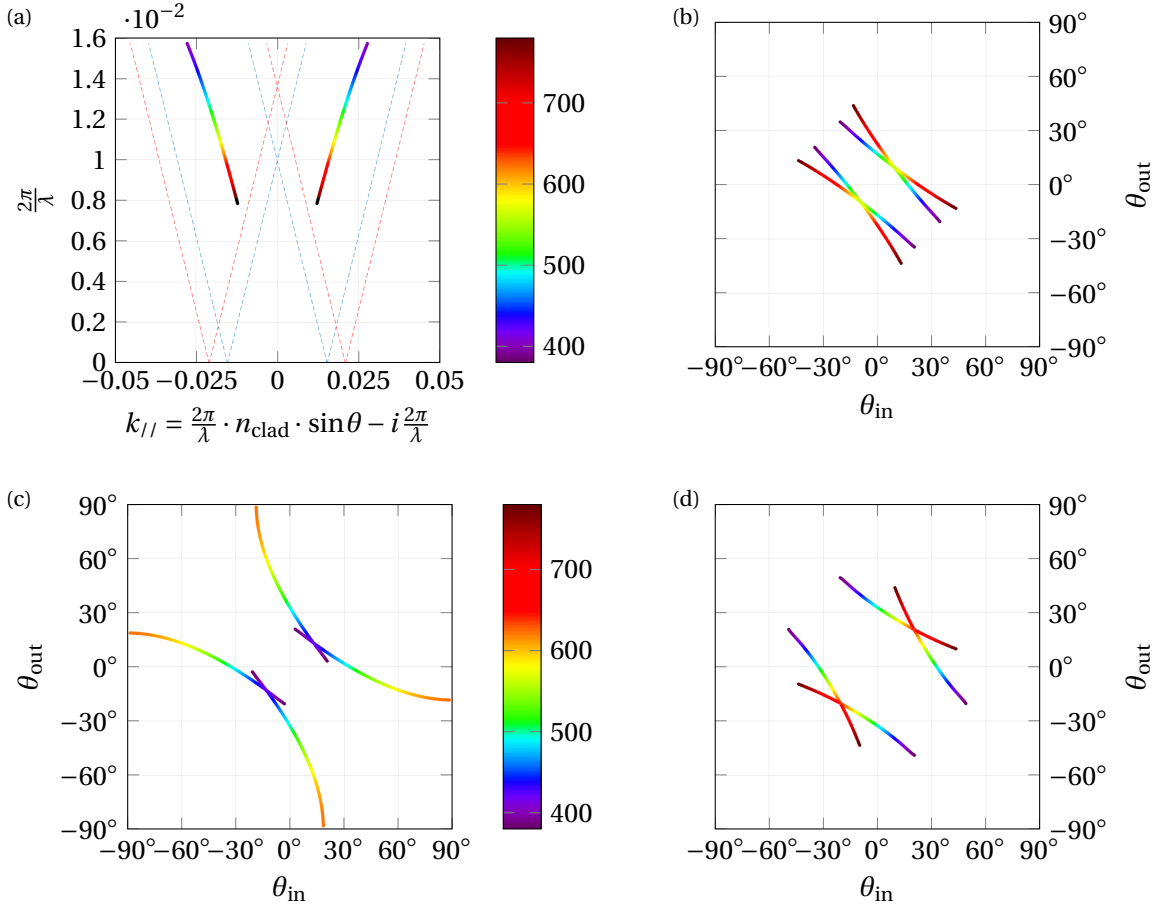
Figure 3.4 – Unit cell made with two RWGs. One RWG is responsible for in-coupling a spectral portion of the incident beam that is then out-coupled from the second RWG. (a) Energy-momentum dispersion plot. (b)-(d) Angular dispersion plots for different Λ_1. The filtered and redirected wavelength is expressed by the color of the lines (colorbar in [nm]). (a,b) Design #2, (c) design #2 with $\Lambda_1 = 200\,\text{nm}$, (d) design #2 with $\Lambda_1 = 600\,\text{nm}$.

3.1.2 Arrays of paired-RWGs: from diffraction to beam redirection

In this section, I describe a system where the same cell (described in Section 3.1.1) is repeated periodically with no gap between cells, as illustrated in Fig. 3.7. Furthermore, I only consider in-plane regime and TE-polarization. For simplicity of notation, the gratings length is reported in terms of the number of grating periods, for both the first and the second grating of the cell (i.e. N_1 and N_2, respectively).

In the case of an array of paired-RWGs, N_1 and N_2 are not only important for determining the spectral band of the coupled modes as discussed in Section 3.1.1, but they also affect the direction of the scattered light. I have thus performed numerical simulations (with both FDTD and RCWA models) for studying the influence of N_1 and N_2 on the angular distribution of the reflected scattered light.
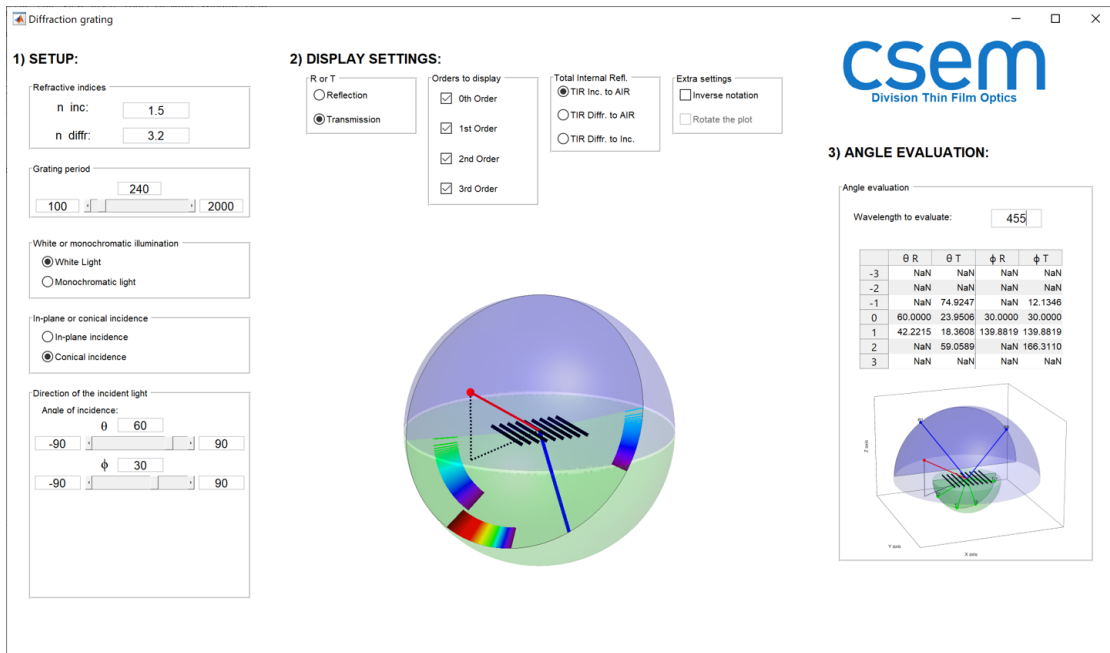
Figure 3.5 – MATLAB script created to visualize conical diffraction in transmission and reflection and to evaluate the angles of diffraction.
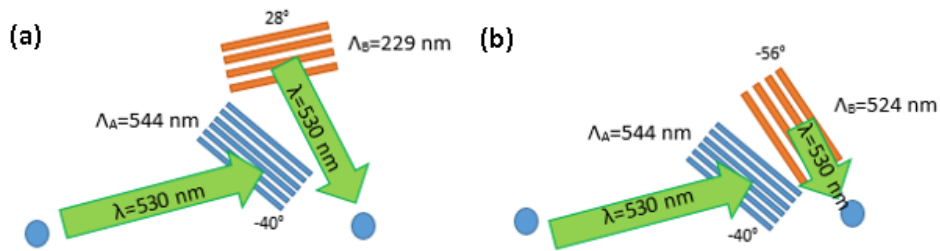

Figure 3.6 – For a given optical configuration, the unit cell can be designed with the two gratings oriented in different directions.

In Fig. 3.8 the far-field reflectance from RCWA simulations is reported: the angular distribution of the out-coupled light includes the contribution from different diffraction orders of the super-period $s = L_1 + L_2$, where $L_{1,2} = N_{1,2}\Lambda_{1,2}$. Therefore, when the cell has a small super-period (i.e. small values of L_1 and L_2), the diffraction pattern is more angularly spread. Conversely, when the cell has a large super-period (i.e. large values of L_1 and L_2), the diffraction orders are closely spaced in angles.

Based on these numerical results, two different regimes can be observed. One regime is based on the diffraction of the super-periods, in particular for small values of N_1 and N_2. Conversely, when the super-period is large and it is made with several periods, the structure exhibits a beam redirection behavior where the contribution of the diffraction from different cells is negligible. Structures with limited diffraction noise have therefore either a very small super-period as in Fig. 3.8b to allow the propagation of only one real diffraction order in free space, or
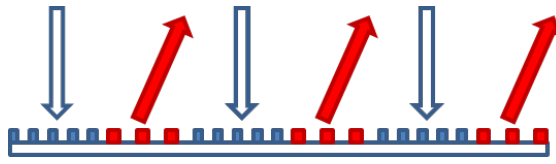
Figure 3.7 – Schematic of an array of paired-RWGs.
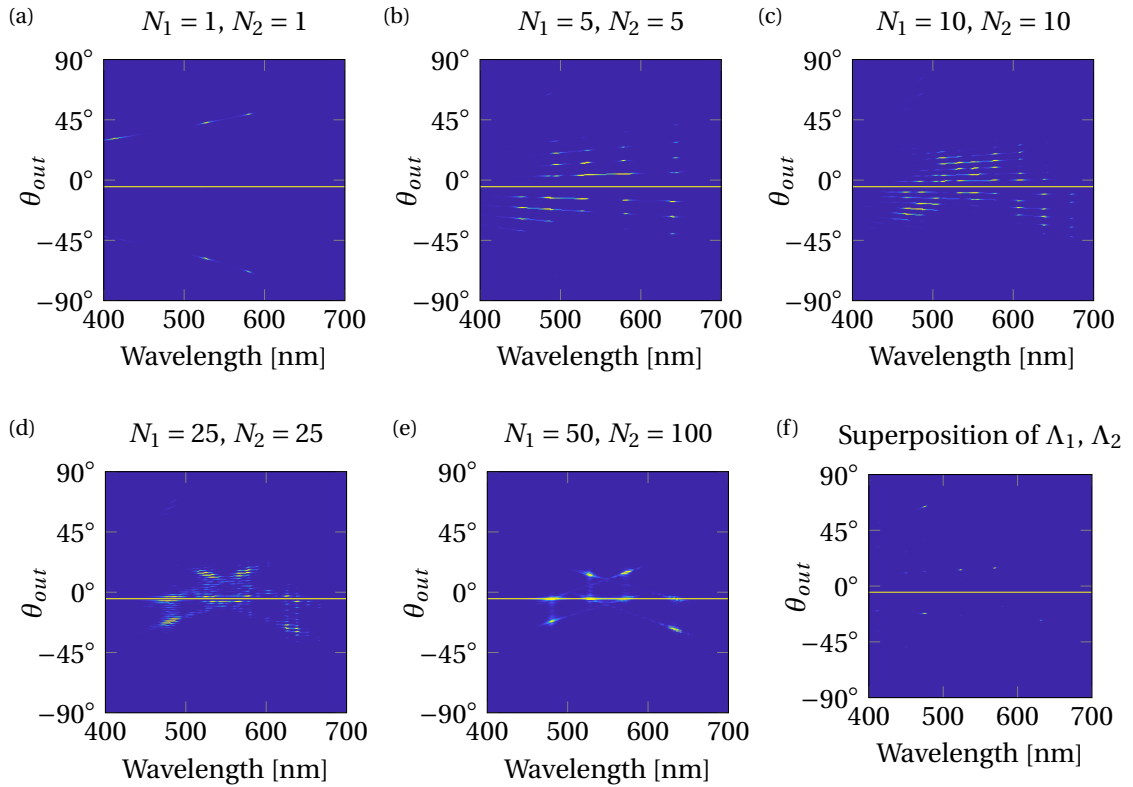
Figure 3.8 – Simulations of reflectance (TE-pol) integrated every 0.5° of the design #1 with increasing values of N_1 and N_2.

a very large super-period as in Fig. 3.8e so that there is a negligible angular distance between the different orders.

We fabricated the design #1 to characterize the efficiency of such structures. We used the cell design as in Fig. 3.8e: we set all the unit cells to have the same periods ($\Lambda_1 = 380$ nm and $\Lambda_2 = 310$ nm), all aligned into the same direction and with no separation between them. We then made several patterns of 2 cm × 1 cm each with different N_1 and N_2. Pictures of such fabricated samples have been taken with a smartphone with the flash turned on as in Fig. 3.9: we could observe that the light of the flash has been diffracted back towards the camera and spectrally filtered. In this case the expected filtered central wavelength can be calculated by solving Eqs. (3.3) and (3.4) for $\theta_{\text{in}} = \theta_{\text{out}}$ and $\phi_{\text{in}} = -\phi_{\text{out}}$. The position of the diffracted peaks can also be computed analytically using the grating equation for a grating period s and the

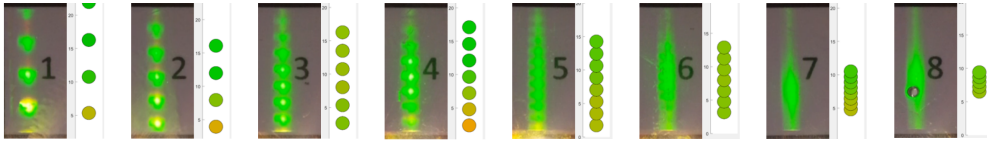Figure 3.9 – Smartphone images of the fabricated design #1, with increasing number of N_1 and N_2, as well as an analytical model to describe the diffraction from the S-periodic pattern. Image 1: $N_1 = 15$, $N_2 = 5$. Image 2: $N_1 = 20$, $N_2 = 7$. Image 3: $N_1 = 30$, $N_2 = 10$. Image 4: $N_1 = 30$, $N_2 = 15$. Image 5: $N_1 = 50$, $N_2 = 10$. Image 6: $N_1 = 50$, $N_2 = 17$. Image 7: $N_1 = 100$, $N_2 = 33$. Image 8: $N_1 = 100$, $N_2 = 50$.
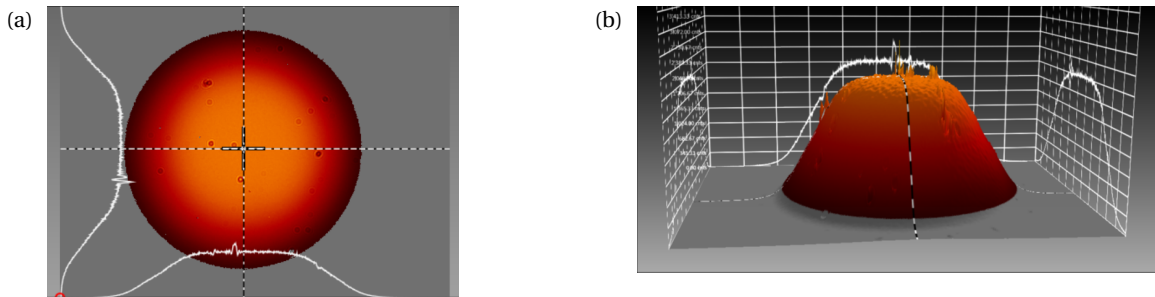

Figure 3.10 – (a) 2D top view of the beam profile. (b) 3D beam profile, showing a good homogeneity.

spectral band (and thus the number of visible diffraction orders) is related to the filtering strength of a finite-size RWG [241].

I then performed the optical characterizations of such patterns using a broad-spectrum white light covering the whole visible and near-IR spectrum (400-1000 nm). The light was generated with a halogen lamp (DH-2000, OCEAN OPTICS) and in-coupled into a fiber with $NA = 0.15$. The fiber was connected to a parabolic reflective collimator (RC04SMA, THORLABS) and reduced in diameter with an aperture (3 mm). The system was placed on a motorized rotation stage (CR1-Z7, THORLABS) to scan the angle of transmission. A second motorized rotation stage was placed on top of the previous one. The sample was placed on that second stage with a holder in order to change the incidence angle of the collimated light on the sample. The whole system was then placed on a motorized linear stage (LTS300, THORLABS) to achieve a higher alignment precision. A spectroradiometer (SPECTRASCAN PR-730, PHOTO RESEARCH) was used to measure the transmitted light after the sample. The transmitted light was recorded from −5° to 40° with steps of 0.5° with a numerical aperture of the spectroradiometer equivalent to 0.5°. The data were then normalized to air. I verified the beam homogeneity with a SPIRICON beam profiling camera, as shown in Fig. 3.10.

The characterization for the case of $N_1 = 50$ and $N_2 = 100$ (corresponding to Fig. 3.8e) has been performed at normal incidence and is reported in Fig. 3.11c. The four resonances are similar in both transmission and reflection, however we chose to characterize the transmittance as reflectance measurements cannot be performed at near-normal incidence. I also performed
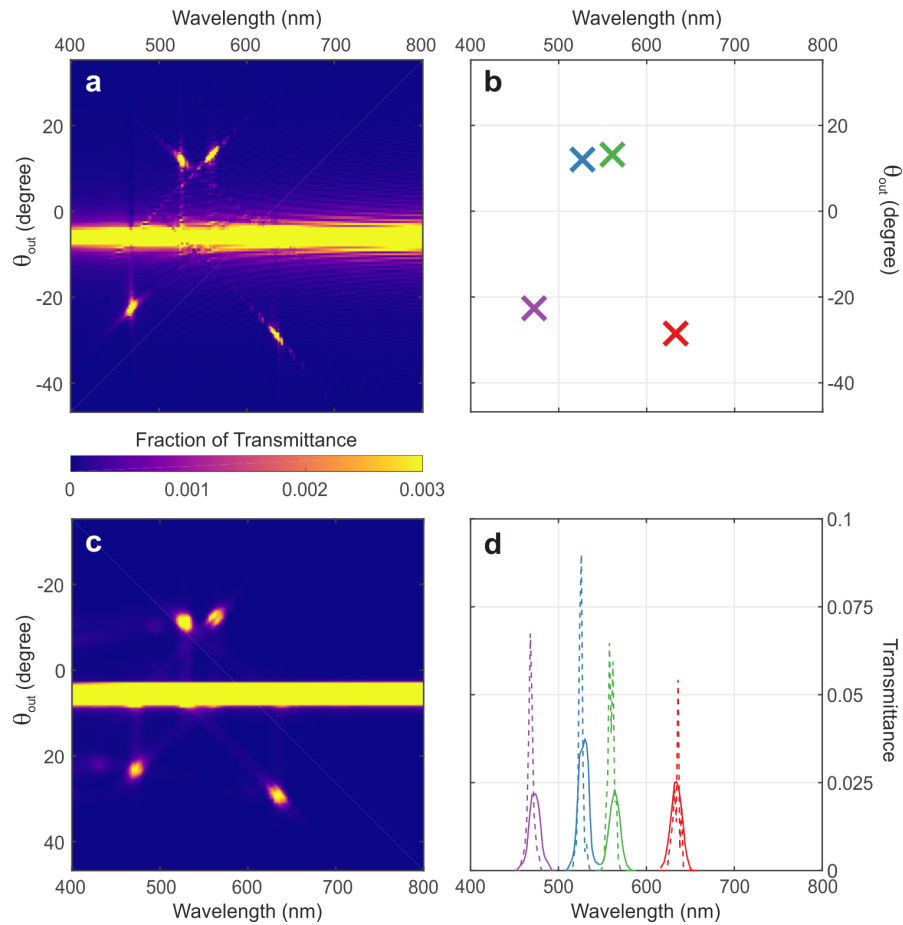
Figure 3.11 – (a) Simulations and (c) measurements of the transmittance integrated every 0.5° for an array of unit cells with two adjacent RWGs (design #1), where the illumination is TE polarized and tilted by 6°, normalized to the illumination in air. (b) The comparison with the analytical model. (d) The transmittance integrated over the angular spread of the four peaks is compared between measurements (solid lines) and simulations (dashed lines).

a FDTD simulation of this structure and the far-field results are plot in Fig. 3.11a, showing a good agreement with the RCWA simulation of Fig. 3.8e. We observe four resonances similar to those obtained in the simulations. The differences, especially in the angular spreading of the resonances, are mainly related to the optical setup (in particular to a 0.2° beam divergence of the light source and the 0.5° numerical aperture of the spectrometer) and to the fabricated device, whose profile differs from the simulated one because of more sinusoidal corrugations which reduce the quality factor of the resonances. These resonances represent the four possible coupled modes obtained in the analytical model (Fig. 3.11b). The analytical model reproduces very well the experimental and full-field numerical data, in spite of the important corrugation of the waveguide (let us recall that Eq. (3.3) holds for a smooth waveguide). Figure 3.11d shows the width profile of the resonances, with a bandwidth of 14 nm for all the resonances, compared with the 5 nm we get from the simulations. This bandwidth is well suited for the optical security application described below, and it can be reduced or increased

by varying the length of the unit cell (i.e., L_1, L_2 in Fig. 3.1).[241] The angular spread is about 3° for each resonance, and it can be reduced by engineering the distance between different unit cells (Eq. (3.5)). The efficiency of each resonance is smaller than 10 % because of the following: the in-coupling grating covers about 50 % of the area, there is an efficiency of about 50 % in both the in-coupling and out-coupling processes in leaky RWGs, and the out-coupled light is split approximately in equal ratio in both the superstrate and the substrate. With these assumptions, we expect less than 10 % efficiency for each resonance.

Another possible configuration is when the two periods of the cell (Λ_1 and Λ_2) are superimposed instead of being adjacent. For this case, I performed numerical simulations considering a minimum subperiod of 100 nm to take into account fabrication tolerances. With the parameters of the design #1 the superposition of the two periods forms a super-period $s = 11.78 \mu m$. In this case, both the in-coupling and the out-coupling gratings cover 100 % of the the cell and the out-coupling process is performed in same region of the in-coupling process, so the simulated efficiency is about 5 % higher for each scattered peak than in the configuration with adjacent gratings. The far-field transmittance of such configuration is reported in Fig. 3.8f. We can observe that there is a narrower angular spread than the case of $N_1 = 50$, $N_2 = 100$ and a narrower spectral band, despite a smaller super-period.

3.2 Advanced patterning of paired-RWGs

A large pattern of these paired-RWG elements can be created in order to filter a specific spectral portion of a point source and to redirect and focus it to another point in the space, viz. the observation point, by positioning the beam redirecting elements on a surface with different grating periods and orientations (see Fig. 3.12). Moreover, the arrangements of these elements must preserve the phase coherence of the whole pattern at the observation point.

In Section 3.2.1 I report a design technique which I have developed that allows rapid creation of those patterns. This technique is based on geometrical and ray-tracing considerations for prolate spheroidal mirrors (usually referred to as ellipsoidal mirrors), which reflect any ray of light coming from one focal point (f_s) to the other focal point (f_p). In Section 3.2.2 that technique is used to generate a test pattern, which is compared to other ones that are generated without applying that technque (i.e. by setting a fixed grating orientation). Finally, in Section 3.2.3 a fabricated sample is used to verify the phase-coherence.

3.2.1 Design method based on confocal prolate spheroids

The design method is derived from the optical properties of a perfect prolate spheroid mirror: all the light rays coming from a point source at a focal point preserve the phase coherence when reaching the second focal point, since by geometry their paths have the same length [248].
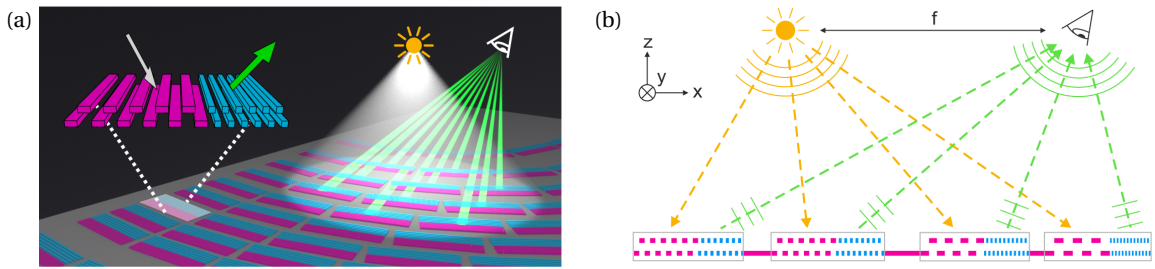
Figure 3.12 – (a) Concept art of light refocusing from a point source to an observer by a pattern of paired-RWGs. (b) 2D section of the concept: it is possible to engineer a complete surface that redirects the light coming from one point to another using constructive interference, as represented here in the inplane regime.
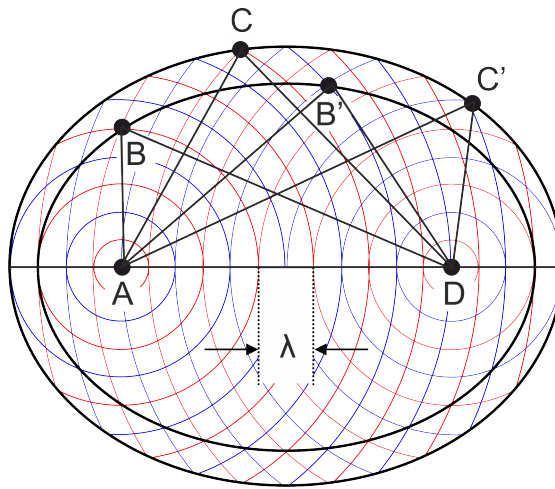
Figure 3.13 – System of confocal elliptical mirrors sharing the same foci: a spherical wave emitted from one focal point always reach the other focal point with the same phase regardless the wavelength and the path.

Moreover, in order to create a pattern covering a given surface, confocal spheroids with different radii are used, as explained in the following. The difference in optical path length between rays reflected from the different spheroids must be a nth multiple of the wavelength in order to ensure constructive interference at the emission from the elements. It follows that also the axes of those ellipsoid must be a nth multiple of the wavelength. A section of those system, i.e. two confocal elliptical mirrors, is sketched in Fig. 3.13, where A and D are the two shared focal points, and B, B', C and C' are random points on their surfaces. Therefore in such systems of confocal ellipsoids the following relations are always satisfied:

$$\overline{AC} + \overline{CD} = \overline{AC'} + \overline{C'D} = \overline{AB} + \overline{BD} + n\lambda = \overline{AB'} + \overline{B'D} + n\lambda, \tag{3.5}$$

where n is an integer number. Following these geometrical considerations, we choose a prolate spheroid Q having the foci and the semi-major axis a on the x-axis, and the semi-minor axis b lying on the y-axis and z-axis (Fig. 3.14a).
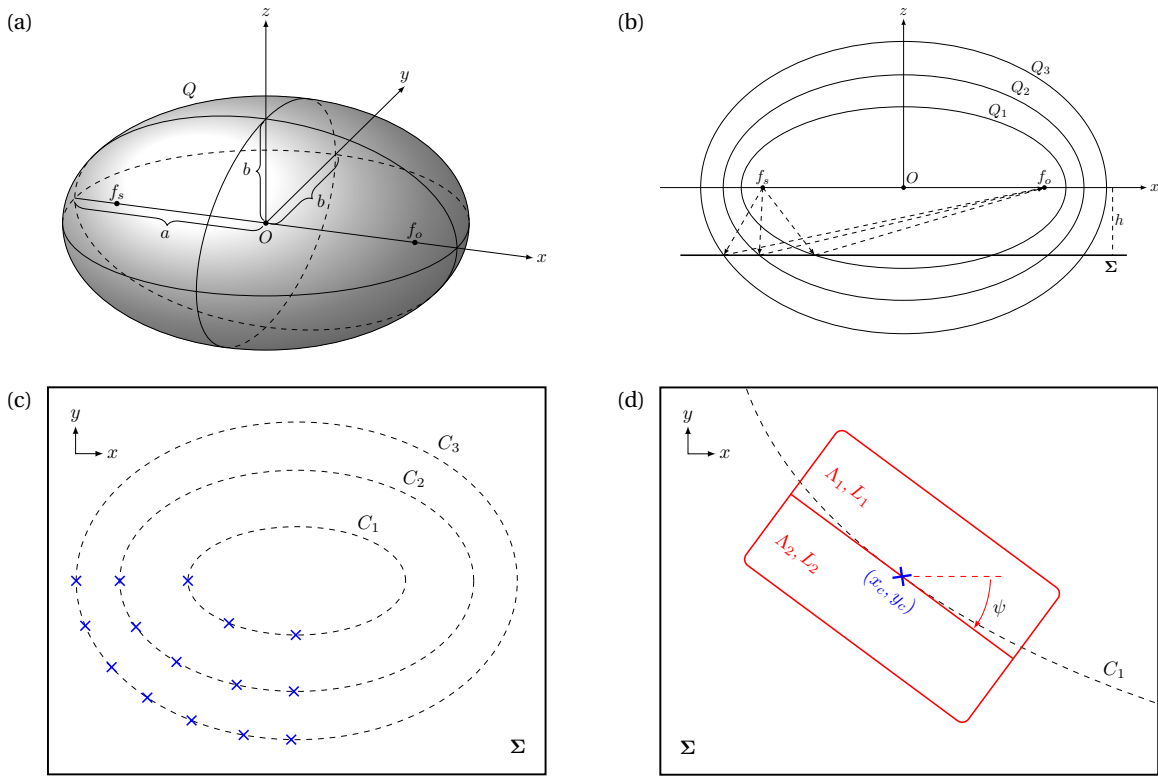
Figure 3.14 – Scheme of the design method based on confocal prolate spheroid arrangements. (a) A prolate spheroid Q. (b) Section of three confocal prolate spheroid, where the structured surface Σ is used to filter and redirect the light from a point source set in the focal point f_s to an observation point set in the focal point f_o. (c) Beam redirecting elements (marked as blue ticks) are placed on the plane Σ and are arranged on sections of the confocal prolate spheroids intersecting the plane Σ. (d) A beam redirecting element (rounded red rectangle) made with two RWGs, where one RWG (Λ_1, L_1) is responsible to in-couple and filter the light coming from f_s and the other RWG (Λ_1, L_1) is used to out-couple the light to f_o.

We place the source point f_s and the observation point f_o in the position of the two foci of Q such that the surface with the pattern of paired-RWG elements (defined as Σ) is intersected by such a spheroid Q. For the purpose of this work, we assume that the surface Σ is planar and normal to the z-axis. Moreover, we consider the case where the source point f_s and the observation point f_o have the same distance h to that surface, so that a spheroid described by the two foci (f_s, f_o) has its semi-major axis parallel to the surface Σ. However, the proposed design rules are valid even in the case when the source and observation points are not parallel to the x-axis or when the surface Σ is not planar. If the foci (f_s, f_o) are not parallel to the x-axis it is still possible to use this system and to apply transformation matrices for any rotation (R)

or translation (T) around any axis (x,y,z):

$$R_x(\theta_x) = \begin{bmatrix} 1 & 0 & 0 & 0 \\ 0 & \cos(\theta_x) & -\sin(\theta_x) & 0 \\ 0 & \sin(\theta_x) & \cos(\theta_x) & 0 \\ 0 & 0 & 0 & 1 \end{bmatrix}, \tag{3.6}$$

$$R_y(\theta_y) = \begin{bmatrix} \cos(\theta_y) & 0 & \sin(\theta_y) & 0 \\ 0 & 1 & 0 & 0 \\ -\sin(\theta_y) & 0 & \cos(\theta_y) & 0 \\ 0 & 0 & 0 & 1 \end{bmatrix}, \tag{3.7}$$

$$R_z(\theta_z) = \begin{bmatrix} \cos(\theta_z) & -\sin(\theta_z) & 0 & 0 \\ \sin(\theta_z) & \cos(\theta_z) & 0 & 0 \\ 0 & 0 & 1 & 0 \\ 0 & 0 & 0 & 1 \end{bmatrix}, \tag{3.8}$$

$$T(\Delta_x, \Delta_y, \Delta_z) = \begin{bmatrix} 1 & 0 & 0 & \Delta_x \\ 0 & 1 & 0 & \Delta_y \\ 0 & 0 & 1 & \Delta_z \\ 0 & 0 & 0 & 1 \end{bmatrix}, \tag{3.9}$$

where the combination of rotations around different axes and a translation can be obtain with the product of such matrices:

$$T(\Delta_x, \Delta_y, \Delta_z) \cdot R_x(\theta_x) \cdot R_y(\theta_y) \cdot R_z(\theta_z) \cdot \begin{bmatrix} x \\ y \\ z \\ 1 \end{bmatrix}. \tag{3.10}$$

We set the origin of the reference system in the middle between the two foci, and we define the half distance between the two foci as f:

$$f = \frac{1}{2}\overline{f_s f_o} = \sqrt{a^2 - b^2}, \tag{3.11}$$

where a and b are, respectively, the major and minor-axis of the prolate spheroid Q. Such prolate spheroid can be therefore defined as:

$$Q: \frac{x^2}{a^2} + \frac{y^2 + z^2}{b^2} = 1. \tag{3.12}$$

Since $h < b$ (i.e. the plane Σ intersects the prolate spheroid), the intersection the spheroid with such a plane Σ defines an ellipse C lying on Σ:

$$C: \frac{x^2}{a^2 \cdot \left(1 - \frac{h^2}{a^2 - f^2}\right)} + \frac{y^2}{a^2 - f^2 - h^2} = 1. \tag{3.13}$$

When a paired-RWG element (Fig. 3.14d) is placed on the planar surface Σ with its center (x_c, y_c) on the ellipse defined in Eq. (3.11) and oriented by an angle Ψ such that the grating lines are parallel to the tangent of the ellipse in (x_c, y_c), it is possible to numerically compute the period of the two gratings such that a broadband light beam coming from f_s is filtered to the desired portion of spectrum and redirected to f_o. If multiple beam redirecting elements have their centers on the ellipse C of Eq. (3.11), the path distances from f_s to f_o will all have the same length, because of the geometrical considerations about prolate spheroids described previously (Fig. 3.14c). Moreover, the out-coupled beams have the same phase difference from the in-coupled beams, since the optical paths and phases gained during the propagation in the RWG having the same length are constant.[176] All the light beams have therefore the same phase at the observation point f_o.

In order to design a full pattern that covers the surface Σ, a number of n prolate spheroids (Q_n) with different radii and intersecting Σ have to be used. Since all those spheroids share the same foci (f_s, f_o), they are described by the geometrical formalism of confocal prolate spheroids (Fig. 3.14b):

$$Q_n : \frac{x^2}{(a+k)^2} + \frac{y^2 + z^2}{(a+k)^2 - f^2} = 1, \tag{3.14}$$

where k is a constant used to increment the length of the semi-major axis.

The intersection of such a family of confocal prolate spheroids Q_n with the plane Σ is described by a family of n non-confocal ellipses C_n:

$$C_n : \frac{x^2}{(a+k)^2 \cdot \left[1 - \frac{h^2}{(a+k)^2 - f^2}\right]} + \frac{y^2}{(a+k)^2 - f^2 - h^2} = 1, \tag{3.15}$$

where the first and the second denominators denote the squares of the semi-major and semi-minor axes of the ellipses.

The constant k defines the distance between the different spheroids or ellipses and must be chosen carefully in order to preserve the phase coherence of the beam-redirecting elements between the different ellipses. In particular, in order to have constructive phase interference for the whole pattern, the path length between the source and the observer must be a multiple of the redirected central wavelength λ, as expressed in Eq. (3.5).

3.2.2 Comparison of the design method with cases of constant grating orientation

In order to verify the design method proposed in this section, we computed a test pattern and we analyzed it using the analytical model calculated in Section 3.1.1. The test pattern (design #3, the parameters are reported in Table B.3) was generated in the following way:

- a list with the centers of the different cells was generated;

- the angle of the cells was calculated using the proposed prolate ellipsoid model;

- the two periods of each cell were calculated with the analytical model.

The results are plotted in Fig. 3.15, showing the calculated orientation angle Ψ of the cells, periods $\Lambda_{A,B}$ and the wavevector components $k_{i_{x,y,z}}$ for both the RWGs (as in Eq. (1.2)).

Two further designs were created with the same parameters, except that the rotation angle of the cell Ψ which has been set to 0° and 90° (i.e. design #4 and design #5). The parameters are reported in Tables B.4 and B.5.

The results are plotted in Figs. 3.16 and 3.17: it is possible to see that the design with the smaller conical incidence (i.e. with the smaller wavevector k_y) is the design #3 based on the prolate spheroid method. This design has therefore a higher efficiency compared to other possible designs where the grating orientation is constant throught the whole pattern.

3.2.3 Evidence of constructive interference

We designed and fabricated a pattern to test the proper behavior of the constructive interference model of Section 3.2.1. For that purpose, the pattern was designed to have all the unit cells aligned into the same direction (i.e. the centers of the cells lie on a line parallel to the semi-minor axis a). In particular, the distance s between different cells was tuned with Eq. (3.5) to create constructive interference in a specific spatial point at one side of the structure. The distance between the source and the observer was chosen to be $\Delta_f = 10\,\mathrm{mm}$ (i.e. the distance between the flash and the camera of a smartphone, so that it can be anayzed by means of a smartphone) and the vertical distance from the structure was set to $h = 65\,\mathrm{mm}$ in order to use a smartphone as test platform.

If a picture with the smartphone is taken in the proper position (i.e. Fig. 3.18a), the pattern is fully green because constructive interference happens for the whole sample. On the other hand, if the picture is taken from a different position (i.e. Fig. 3.18b), the pattern is not uniformly green and exhibits localized colored spots.
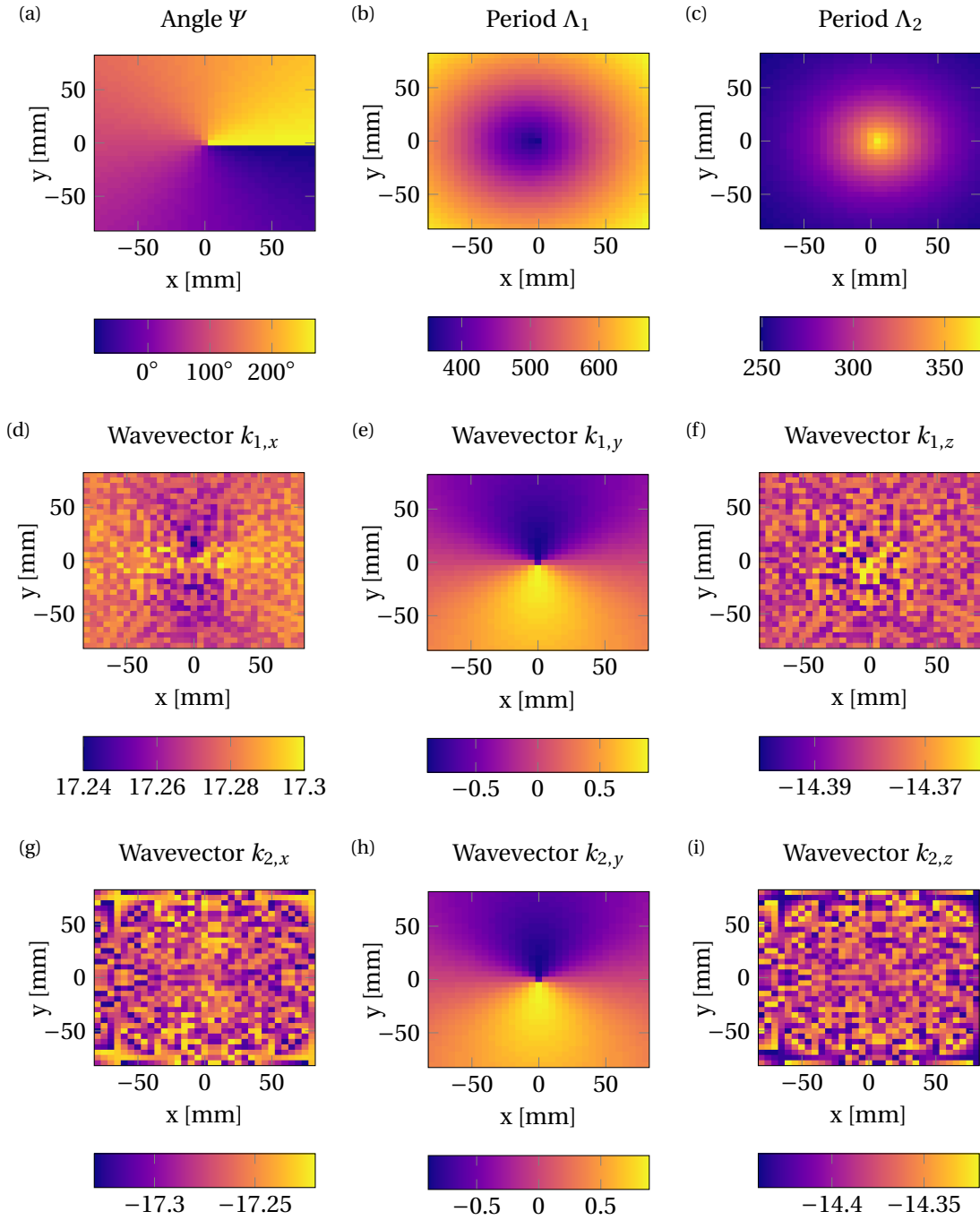
Figure 3.15 – Calculated orientation angle Ψ of the cells, periods $\Lambda_{A,B}$ and wavevector components $k_{i_{x,y,z}}$ for both the RWGs of the cells for the design #3, where the orientation angles and periods are calculated with the design method of Section 3.2.1. Colorbars are in degrees for the angle, in nm for the lengths and nm^{-1} for the wavevectors.
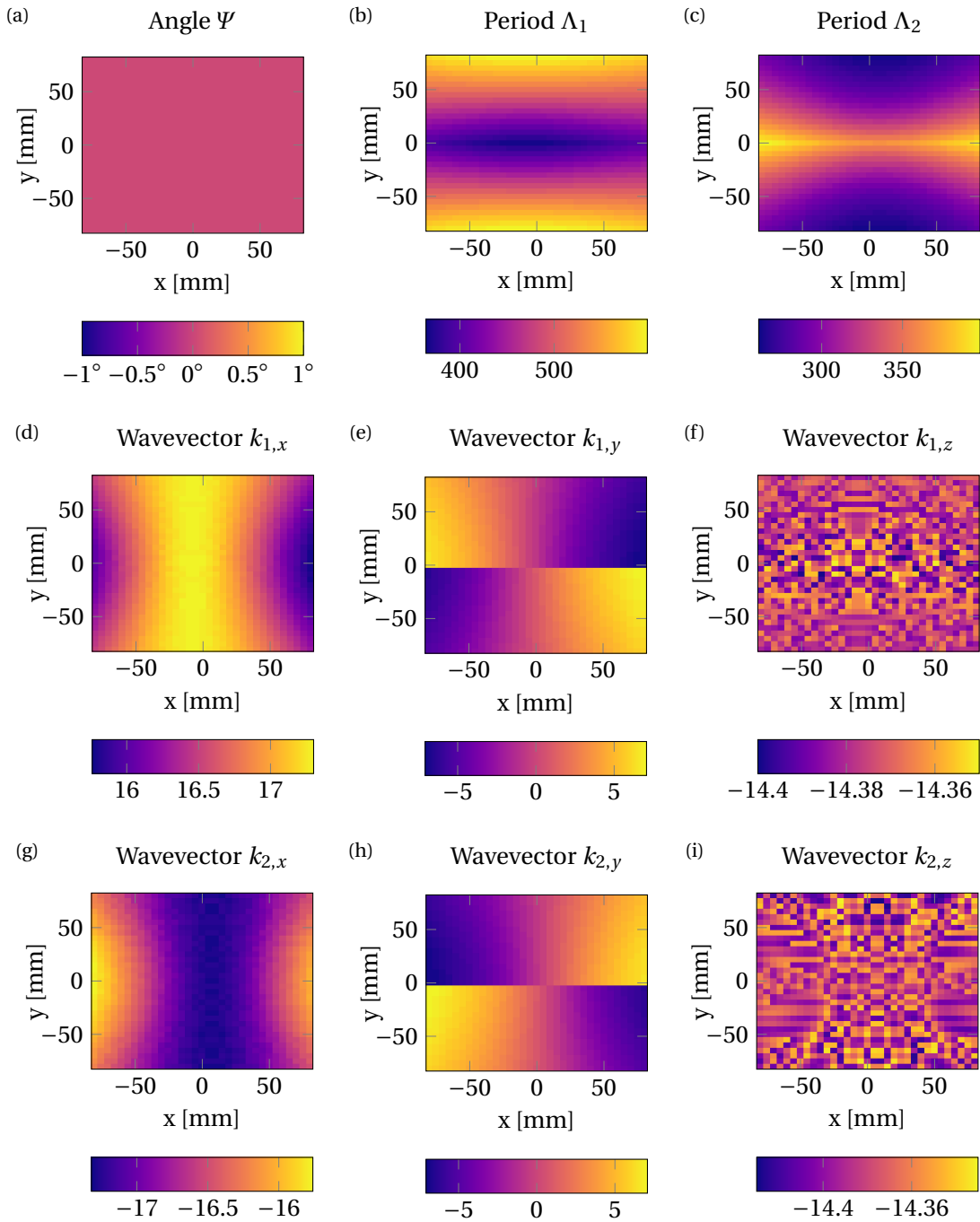
Figure 3.16 – Calculated orientation angle Ψ of the cells, periods $\Lambda_{A,B}$ and wavevector components $k_{i_{x,y,z}}$ for both the RWGs of the cells for the design #4, where the orientation angles have been set to 0°. Colorbars are in degrees for the angle, in nm for the lengths and nm^{-1} for the wavevectors.
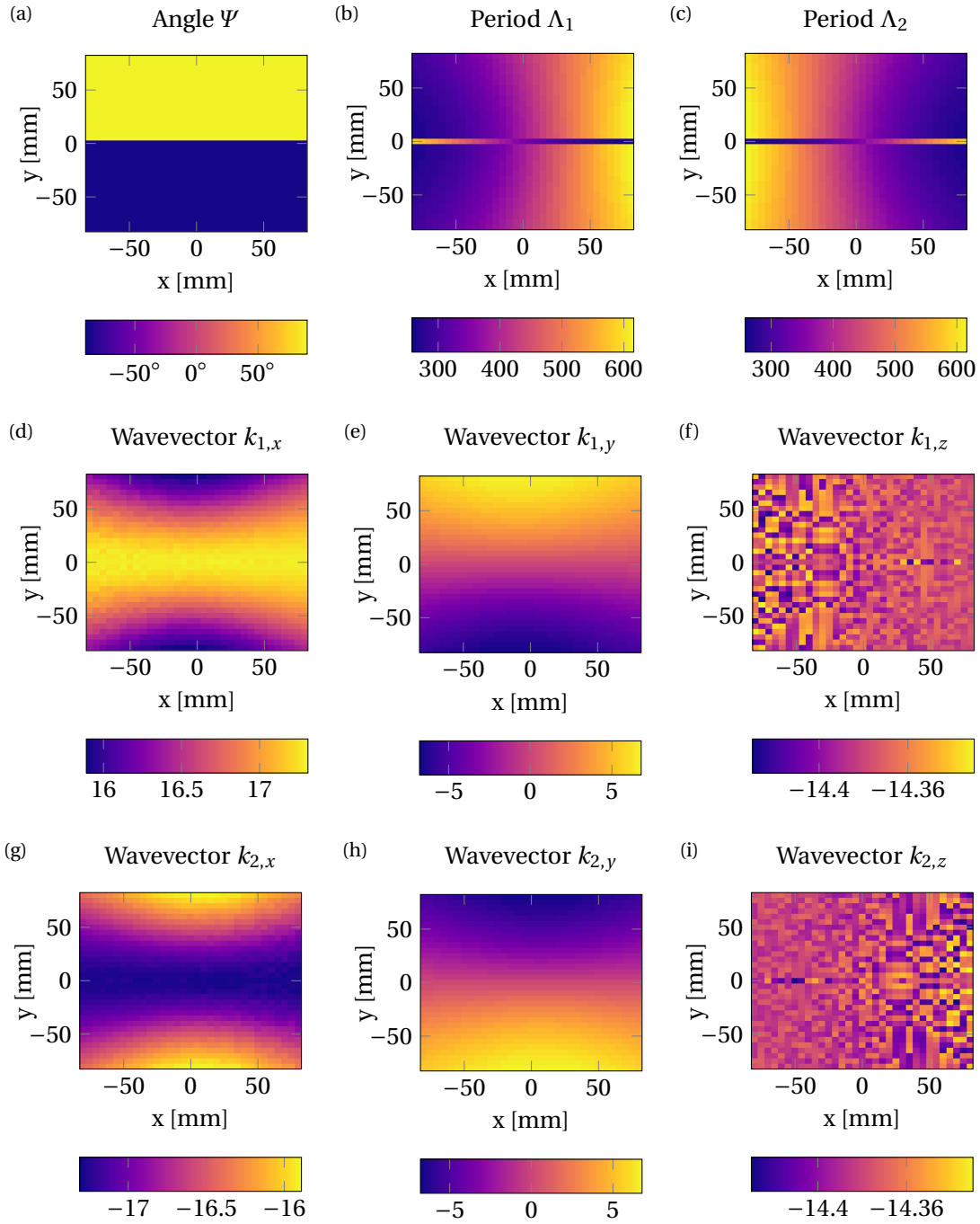
Figure 3.17 – Calculated orientation angle Ψ of the cells, periods $\Lambda_{A,B}$ and wavevector components $k_{i_{x,y,z}}$ for both the RWGs of the cells for the design #5, where the orientation angles have been set to 90°. Colorbars are in degrees for the angle, in nm for the lengths and nm^{-1} for the wavevectors.

Figure 3.18 – a) Image taken with a smartphone in the designed position and b) another image taken after having rotated the pattern in the $x - y$ plane by 180°. (c) Schematic of the two positions. The double pattern present in both pictures is due to the double LED of the smartphone.

3.3 Realization of smartphone-based optical security devices
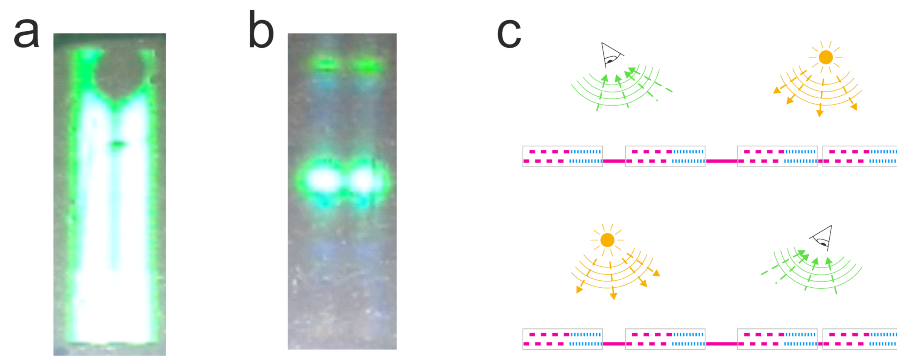
It is possible to take advantage of the beam redirection property shown in the previous sections to design beam redirecting or focusing devices that can be used in a variety of different fields, for example:

- optical security device which shows hidden pattern by means of a smartphone[249];

- multifocal (i.e., different colors focused in designed positions) or monochromatic lenses;

- biosensors such as gas sensors, where a pattern appears on the smartphone only when no gas is detected[250];

- see-through optical combiners for near-eye displays, by redirecting the light from a micro-projector to the human eye[251].

In the following we show the implementation for optical security devices that work with a smartphone. In particular we designed and fabricated several transparent structures that show uniform colors, pictures and animations on the smartphone's screen when the smartphone is located in a specific position on top of the security device, as illustrated in the concept-art Fig. 3.19. In particular, the light coming from the smartphone's flash is spectral-filtered from the device and redirected to the camera. In our work, we have approximated the smartphone's flash and camera to points and we have used the prolate spheroid technique discussed in the previous section. The effect is obtained only for the order $i = +1$ for the in-coupling and the order $i = -1$ for the out-coupling, while other channels do not yield constructive interference. Under normal ambient light condition, the structure is almost completely transparent and it is not possible to observe any diffraction by nacked eye, except at very large angles. Thanks to the tolerance of the configuration (e.g., out-coupled spectrum of 14 nm and broad redirection angle), the effect is robust with respect to the smartphone positioning. In particular, it accepts some offset in all the three directions, as well as in the distance between source and observer. In fact, the effect has been tested with different smartphones (e.g., NOKIA LUMIA 920, SAMSUNG GALAXY S3, and IPHONE 6s) and it correctly appeared as designed. The tenuous color variations between the designed and the observed colors are mostly related to the smartphone hardware and the postprocessing software (i.e., the spectrum of the LED, the characteristics of the CMOS sensor, the brightness level, as well as the white balance).

3.3.1 Design of uniformly colored squares on different substrates

The first designs aimed to create a squared pattern which shows uniform colors when the smartphone is properly positioned. In particular, three squares of 1 cm × 1 cm were realized: red (design #6), blue (design #7) and green (design #8). They have been designed to work together sharing the same coordinates of the point source (f_s) and observer (f_o) to test the color homogeneity for different positions and angles of the RWGs. The details of the parameters for those designs are reported in Table B.6.
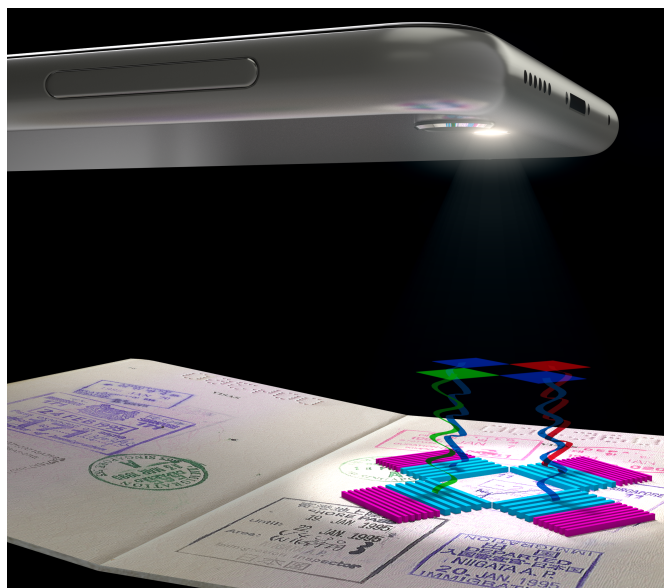
Figure 3.19 – Optical security label made with RWGs that reveals a hidden pattern by using the flash and the camera of a smartphone in a specific spatial position (artistic rendering).

For each realization, we engineered a flat surface composed by more than 20 000 passive beam redirecting elements, where the light coming from the flash of the smartphone is spectrally filtered and in-coupled in one RWG. The other RWG of the unit cell is responsible to out-couple the guided-mode toward the camera of the smartphone. Moreover, all the beam redirecting elements have been designed to create constructive interference of all the out-coupled beams in the position of the camera and the smartphone, where they are focused. The system is in off-axis configuration because the angle Ψ between the source point f_s (i.e., the flash) and the observer f_o (i.e., the camera) is nonzero but is determined by the system of confocal prolate spheroids described in the previous section. In Fig. 3.20, the engineered values of the grating periods (Λ_1 and Λ_2) and the orientation of the beam redirecting elements (Ψ) with respect to the x-axis are reported for the design #6 (i.e. the red pattern).

First, the fabrication of the designed pattern involves the creation of the master silicon wafer by means of electron beam lithography process, as described in details in Section 2.4. Using UV-NIL lithography, a first realization is created by replicating the master wafer on glass using Ormocomp, a UV curable sol-gel [244], and hard-backed. Subsequently, the ZnS layer is deposited with PVD, and finally, the structure is encapsulated by the same UV sol-gel used for the NIL lithography. A second realization is fabricated on a thin PMMA foil by hot-embossing nanoimprint lithography. Afterward, the ZnS waveguiding layer was added with PVD and the structure was finally encapsulated and glued on a business card.

To test the realizations, a smartphone (i.e., ASUS ZENFONE 2) was fixed on a stand at 6.5 cm above the device, with the flash, and the camera centered in the chosen positions of source (f_s) and observer (f_o), respectively. In this configuration, the light of the flash is filtered and
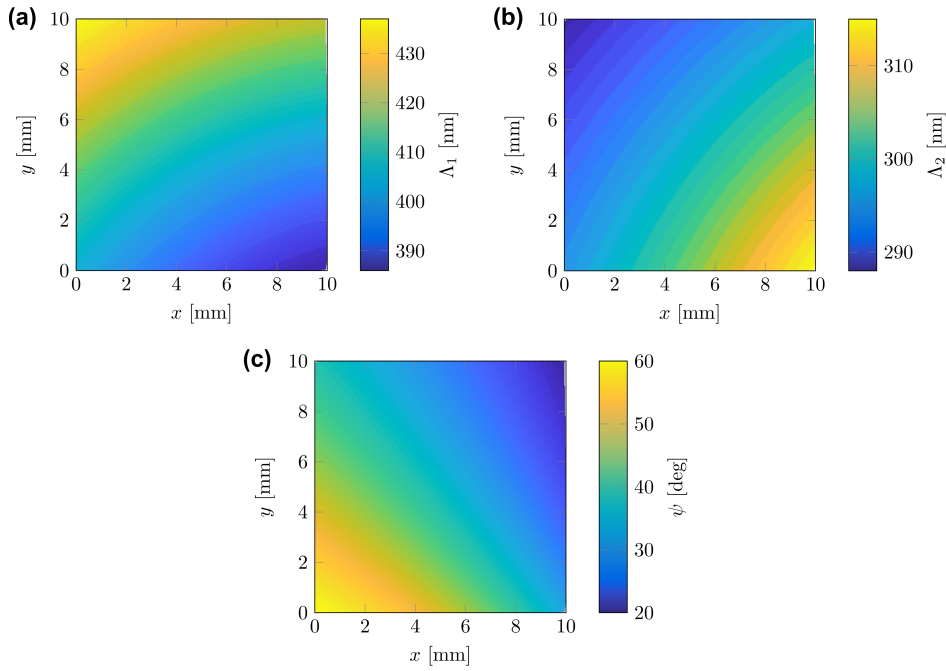
Figure 3.20 – Engineered label (design #6) that shows a uniform red color on the screen of a smartphone when enlighted with its flash in a specific position. Values of (a) Λ_1, (b) Λ_2 and (c) the grating orientations Ψ are shown.

redirected to the camera, showing colorful squares (Fig. 3.21b,c). Thanks to RWGs, the optical effect has been shown to work with a low coherent light source, such as the white LED of the smartphone. However, it is also possible to use light sources with higher coherence. The pattern is almost invisible to the naked eye, and it has small diffraction noise. It is possible to observe defects related to the fabrication on PMMA (Fig. 3.21b) with hot-embossing technique. These defects are not present in the same device created on a glass substrate (Fig. 3.21c). Some defects and inhomogeneities are visible on the glass sample due to electron beam exposure approximations, which could be easily addressed.

To quantitatively characterize the high transparency of the sample in environmental illumination, we measured the transmittance with a spectrometer (SPECTRASCAN PR-730, PHOTO RESEARCH) normalized to the illumination in air. The light source used was generated from a halogen lamp (DH-2000, OCEAN OPTICS) and collimated with a parabolic reflective collimator (RC04SMA, THORLABS) perpendicularly to each of the three squared patterns. The results are reported in Fig. 3.22, as well as the computed Lab colors of such spectra using the CIE Standard Illuminant D65 and the CIE 1964 Color Space. We can observe a general high transparency level for all the three structures, with high values of the coordinate L. Furthermore, we notice the presence of two dips for each measurement, related to the resonances of the RWGs in transmission at normal incidence for both Λ_1 and Λ_2. Due to those dips, the coordinates a and b are different from zero and thus slightly different from true gray neutrality.
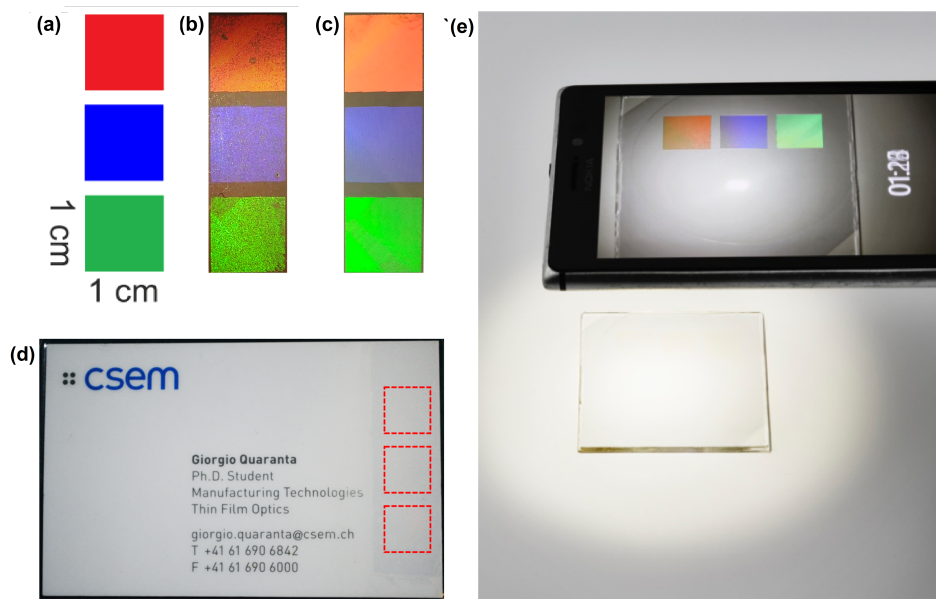
Figure 3.21 – (a) Images of devices created with a customized pattern where the source and the observer are the flash and the camera of a smartphone. Note that the devices are not visible outside the designed observation point. The desing aims to realize uniform red, blue, and green squares (1 cm × 1 cm each). (b,c) Images taken with the smartphone placed in the proper position and with the flash turned on for a device embedded on a business card, as illustrated in (d), and for a device fabricated on glass substrate, as further illustrated in (e).

Another realization we designed was a pattern showing a uniform white color. The device was created with three interlaced patterns red, green and blue working in the same illumination and observation point. A picture taken with the smartphone is shown in Fig. 3.23.

3.3.2 Design of animated images with multiple focal points

Other smartphone-based demonstrators has been designed in the context of optical document security. In particular, we have investigated a dynamic effect which enables seeing on the smartphone different colorful images by slighly translating the smartphone on the device.

These devices have been engineerd by composing two interlaced patterns of 4 mm × 4 mm. In particular, half of the total area is designed to show one image in one illumanation and observation position, and another half is designed to show a different image in another position. The area splitting is made in a chessboard-like partition, as visible in Fig. 3.24. The reader can notice the different squared cells made with two different grating periods (visible by the difference in contrast) and rotated by almost 90° with their adjacent cells because of the two interlaced patterns.

I created a MATLAB script which generates the `.gds` file with the desired design, which is used in the electron beam lithography process to fabricate the master wafer. The script is
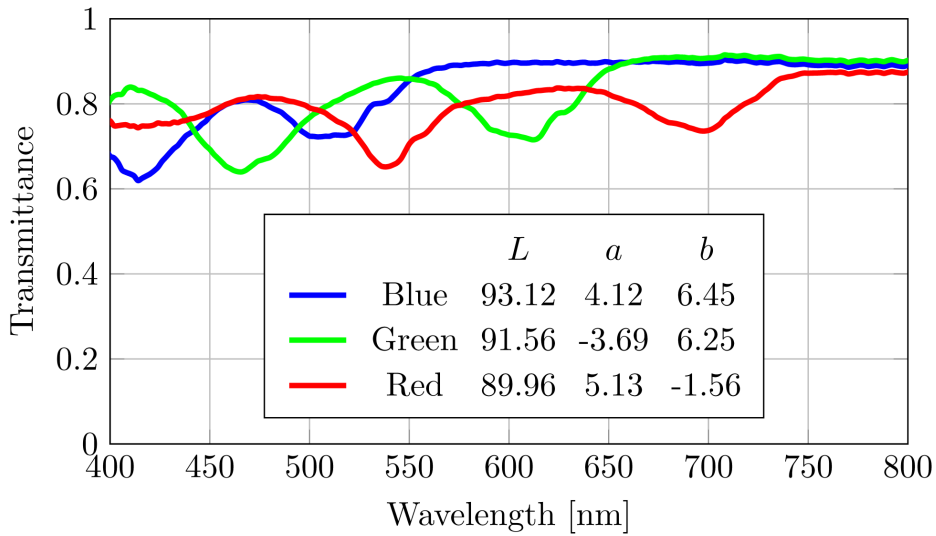
Figure 3.22 – Transmittance at normal incidence from the three squared patterns, normalized to the illumination in air, showing the high transparency of the patterns. The inset reports the computed Lab colors of these spectra, using the CIE Standard Illuminant D65 and the CIE 1964 Color Space.

fully-automatized and optimized for parallel computing. As input, the user needs to load the `.png` images with the colorful patterns to be seen on the smartphone as well as the parameters of the system (i.e. size of the pattern, size of the unit cell, materials and waveguide thickness, smartphone positions). The script relies on the analytical model of shallow RWGs described in Section 1.1.2. Thanks to the use of analytical equations only and a careful optimization of the `parfor` loops, patterns of $25 \, \text{mm}^2$ can be efficiently generated in less than 5 min with a mobile workstation based on INTEL i7-4900MQ processor. Moreover, the grating lines are automatically split into thinner stripes in the `.gds` file using the pre-fracturing technique described in Section 2.4. The flow-chart of the MATLAB script is shown in Fig. 3.26.

The samples were fabricated and replicated on glass and on PMMA foils laminated in business cards, as described in the previous section. Simulations and smartphone images of the fabricated realizations are shown in Fig. 3.25.
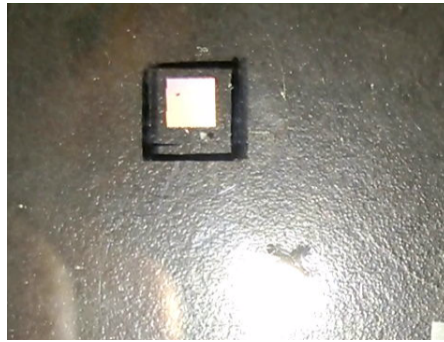
Figure 3.23 – Device composed by three interlaced patterns of red, green and blue working in the same illumination and observation points, showing a white color.
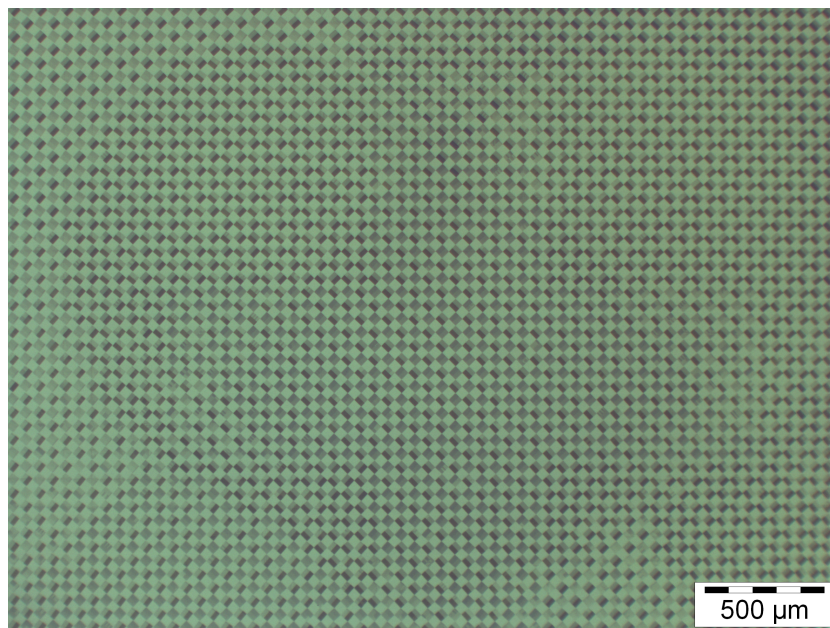
Figure 3.24 – Microscope image for the master wafer of a device composed of two interlaced patterns working in different illumination and observation points.

(a)

(b)
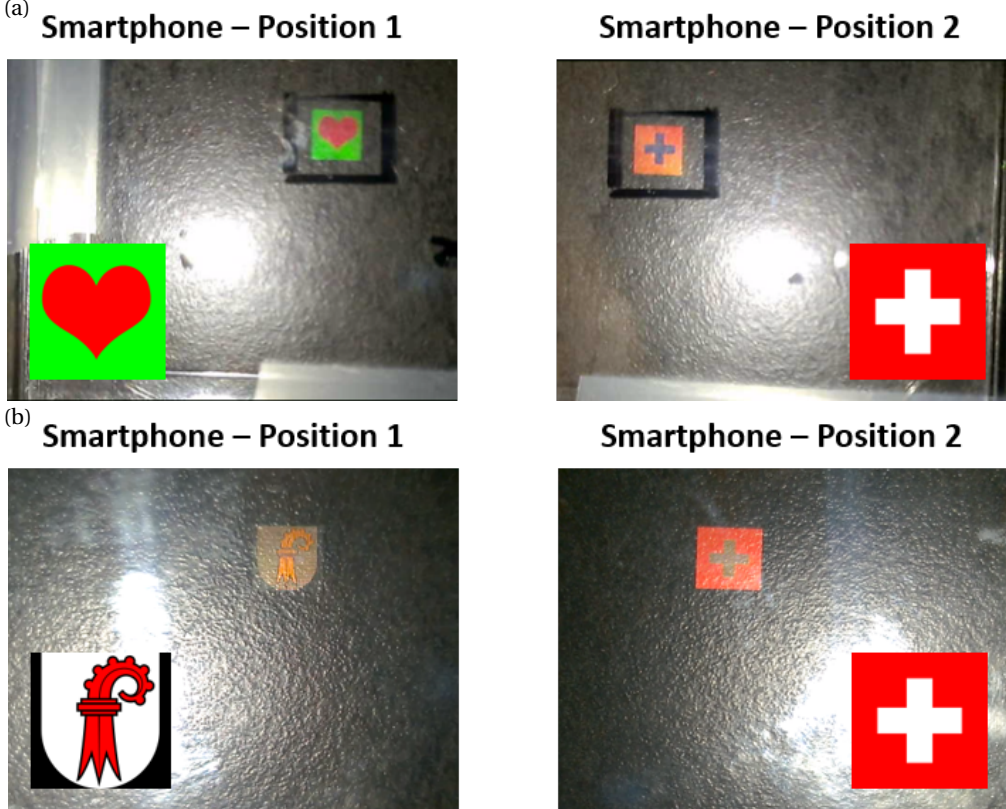
Figure 3.25 – Smartphone photos of fabricated samples which shows different images depending on the position of the smartphone. The insets are the designs, where black is created with a dummy grating with small period such that it does not diffract, and the white is the pixelization of red, green and blue redirecting cells closely nearby. The samples are 4 mm × 4 mm.
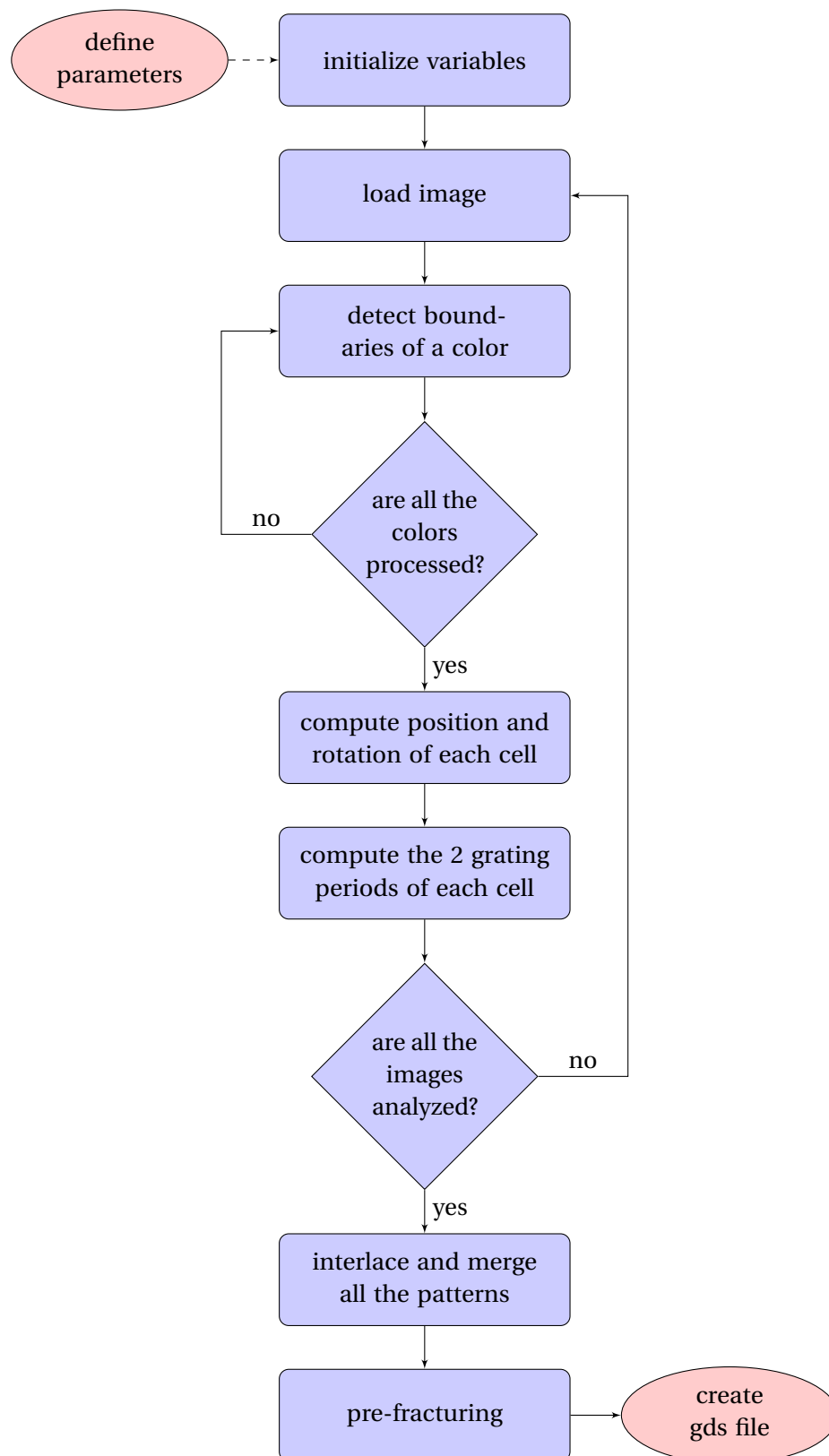
Figure 3.26 – Flow-chart of the MATLAB script to generate the gds file for the animated images

3.4   Conclusions

In summary, we have demonstrated a planar optical structure that selectively filters and redirects or refocus spectral portions of the incoming light. It operates under unpolarized white light and low-coherence source and works both in transmission and reflection. This device relies on unit cells that are designed by choosing a particular pair of impedance matched RWGs, where the first acts as in-coupler and the second acts as out-coupler. This structure exhibits a good color tunability; it is made by only one NIL replication and one thin film layer deposition, such that its fabrication is compatible with up-scalable fabrication processes. The demonstrated device is therefore well-suited for industrial applications, where high throughput is required. Further developments can include the possibility of using ultrathin metallic waveguides or combined metallic/dielectric waveguides. The reported concept was created for an optical security application, for which RWGs have been very successful and are used to secure billion of documents every year [21]. The proposed methodology can be applied to realize passive beam redirecting structures for a variety of other fields. When one focal point is set to infinity, multifocal (i.e., different colors focused in designed positions), or monochromatic lenses can be designed with a system of confocal paraboloids. This method could also be implemented in gas sensing, where a pattern appears on the smartphone only when no gas is detected. This behavior can be realized with refractive-index sensing [7] or absorption sensing [87]. Furthermore, see-through optical combiners for near-eye displays could be designed by redirecting the light from a microprojector (in the position of the point source f_s) to the human eye (in the position of the observer f_o) [251].

4 Color-selective optical coupler for multimode waveguides

My contributions to this chapter were: designing and fabricating the samples, measuring them, analyzing the data, scripting the simulations, preparing the figures and writing the text. The thesis director and thesis co-director edited the manuscripts and contributed to the discussion of the results together.

The guided modes of a slab waveguide cannot be excited by free-space light incident on its interfaces, because an additional momentum has to be provided [252]. An extensive range of optical couplers have been utilized to add such momentum, such as highly focused optical beams onto an exposed cross-section of the waveguide [253] or prism couplers [254]. Diffraction grating couplers and resonant waveguide gratings are among the most implemented configurations for miniaturized and integrated couplers because of their planar manufacturing process [1]. However, those configurations are spectrally broad and, for a thick multimode waveguide and white light source, a broad portion of the spectrum is coupled into guided-modes [83, 255]. As a consequence, it is not possible to achieve narrowband operations in such configurations. Recent advances in metasurfaces have allowed designing spectrally selective diffraction devices, but with fabrication technologies challenging to up-scale [256, 257].

In this chapter, a method to efficiently couple a narrowband spectrum from a free-space incident white light source to a thick multimode waveguide is reported. The method is based on the excitation of surface modes of a dielectric waveguide with a thin-metallic substrate [258, 259]. A schematic of such a structure is shown in Fig. 4.1: a narrowband portion of a broadband light source is coupled from the superstrate into surface modes at the corrugated dielectric-metallic interface of the waveguide, it is evanescently transmitted to the other metallic interface and radiated into the substrate as a guided mode. We refer to the thicknesses of the dielectric and metallic layers as t_W and t_M, respectively. The corrugation of such a waveguide is achieved by a grating of period Λ and modulation depth d. The refractive indices of the superstrate, dielectric layer, metallic layer and multimode waveguide substrate are n_{sup}, n_W, n_{M} and n_{sub}, respectively. In this work, the superstrate is air ($n_{\mathrm{sup}} = 1$), the dielectric layer and the multimode substrate are chosen to be silica (SiO$_2$), with dielectric function from Malitson [260], and the metallic layer is silver (Ag), with dielectric function from Yang et al.
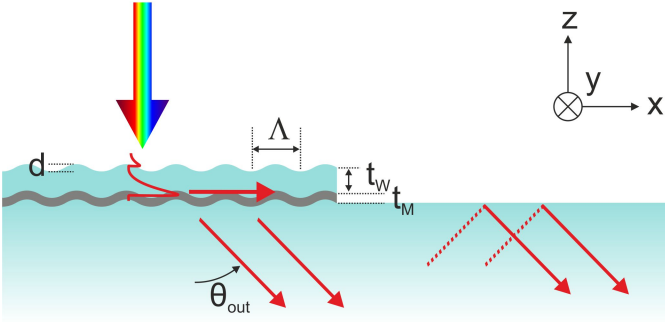
Figure 4.1 – Schematic of the device which allows to selectively couple light with high wavelength selectivity into a thick multimode waveguide. The wavelength range, as well as the coupled angle θ_{out} can be independently tuned by changing geometrical parameters of the device (i.e. the grating period Λ and the thickness of the dielectric waveguide t_W).

[261].

4.1 First diffraction order transmission from surface plasmon polaritons

We start the discussion with the analysis of a simpler structure, where there is no waveguide layer (i.e. $t_W = 0$), to show how a thin corrugated metallic layer can diffract narrowband portions of light into the substrate. This configuration is well known in literature: the metallic film is capable of supporting surface-plasmon polaritons (SPPs) for TM-polarization of the incident light [262]. Assuming to have a flat interface, the dispersion relation is calculated by imposing the continuity of the wave equation for E_x and H_y at the two interfaces [258]:

$$\tanh\left(k_M t_M\right) = -\frac{k_M n_{\mathrm{M}}^2 \left(n_{\mathrm{sup}}^2 k_{\mathrm{sub}} + n_{\mathrm{sub}}^2 k_{\mathrm{sup}}\right)}{n_{\mathrm{sup}}^2 n_{\mathrm{sub}}^2 k_M^2 + n_{\mathrm{M}}^4 k_{\mathrm{sup}} k_{\mathrm{sub}}},$$
(4.1)

with:

$$\begin{cases} k_{\mathrm{sup}}^2 = \beta^2 - n_{\mathrm{sup}}^2 k_0^2 \\ k_{\mathrm{M}}^2 = \beta^2 - n_{\mathrm{M}}^2 k_0^2 \\ k_{\mathrm{sub}}^2 = \beta^2 - n_{\mathrm{sub}}^2 k_0^2 \end{cases},$$
(4.2)

where $k_0 = \frac{2\pi}{\lambda}$ is the wavevector of the propagating wave in vacuum and β is the complex propagation vector parallel to the surface.

When the thickness of the metallic layer t_{M} is much larger than the skin depth, then $\tanh\left(k_M t_M\right) \to 1$ [258] and so Eq. (4.1) can be reduced to two sets of solutions:

$$k_{\mathrm{sup}} n_{\mathrm{M}}^2 = -k_{\mathrm{M}} n_{\mathrm{sup}}^2, \quad k_{\mathrm{sub}} n_{\mathrm{M}}^2 = -k_{\mathrm{M}} n_{\mathrm{sub}}^2,$$
(4.3)

leading to the well-known SPP dispersion relations for single metallic/dielectric interfaces [263]:

$$\beta_{\mathrm{SPP,\,sup}} = k_0 \frac{n_{\mathrm{sup}} n_{\mathrm{M}}}{\sqrt{n_{\mathrm{sup}}^2 + n_{\mathrm{M}}^2}}, \quad \beta_{\mathrm{SPP,\,sub}} = k_0 \frac{n_{\mathrm{sub}} n_{\mathrm{M}}}{\sqrt{n_{\mathrm{sub}}^2 + n_{\mathrm{M}}^2}}.$$
(4.4)

We then consider the influence of the grating to such a system. As illutrated in Fig. 4.2a, the incident light is diffracted by the grating at the first interface and the first diffraction order is coupled into a SPP mode:

$$\beta_{\mathrm{SPP}} = k_{\mathrm{sup},x} + m \frac{2\pi}{\Lambda},$$
(4.5)

for $m = 1$, where m is an integer number called diffraction order. It is possible to verify that such a mode is non-radiative, or bounded, at the first interface because:

$$\mathrm{Re}\left(k_{\mathrm{sup}}^2\right) = \mathrm{Re}\left(\beta^2\right) - \mathrm{Re}\left(n_{\mathrm{sup}}^2 k_0^2\right) > 0.$$
(4.6)

77
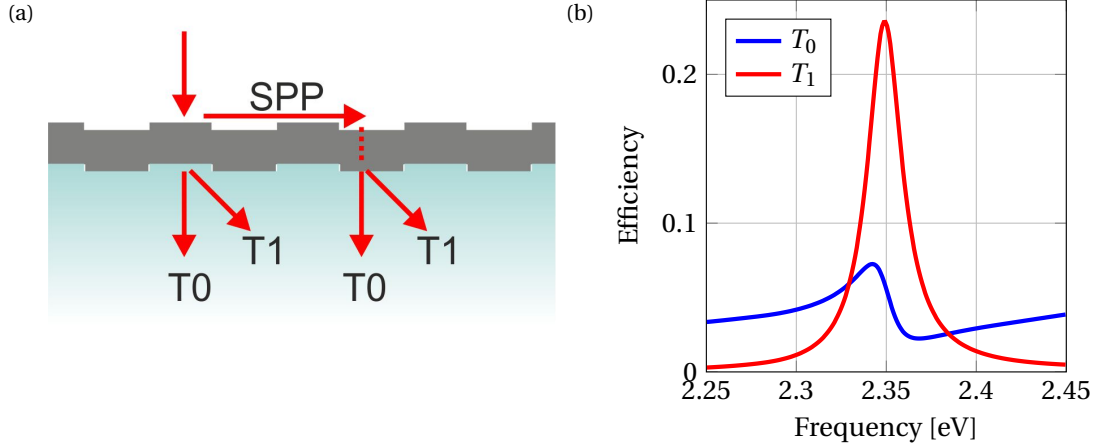
Figure 4.2 – (a) Schematic of the different contributions of the zeroth diffraction order transmission and first diffraction order transmission in case of no waveguide layer ($t_W = 0$ nm). (b) Simulated ratio of diffracted to incident power T_0 and T_1 for $\Lambda = 500$ nm, $d = 13$ nm, $t_W = 0$ nm, $t_M = 50$ nm, rectangular grating profile.

The bounded mode is evanescently transmitted to the second interface, where it becomes a leaky mode, which irradiates into the substrate. In fact, it is possible to verify that: $\text{Re}\left(k_{\text{sub}}^2\right) < 0$ because $n_{\text{sub}} > n_{\text{sup}}$. Such radiation can occur without diffraction or by being again diffracted by the grating at the second interface:

$$k_{\text{sub},x} = \beta_{\text{SPP}} + q\frac{2\pi}{\Lambda} = k_{\text{sup},x} + m\frac{2\pi}{\Lambda} + q\frac{2\pi}{\Lambda}, \tag{4.7}$$

where q is an integer number of the diffraction order at the second interface. In the case of no further diffraction (i.e. $m = 1$ and $q = 0$), the SPP mode is radiating at the first diffraction order into the substrate:

$$k_{\text{sub},x} = k_{\text{sup},x} + \frac{2\pi}{\Lambda}, \tag{4.8}$$

whereas in the case of diffraction at the second interface (with $m = 1$ and $q = -1$), the mode is radiating at the zeroth diffraction order into the substrate:

$$k_{\text{sub},x} = k_{\text{sup},x} + \frac{2\pi}{\Lambda} - \frac{2\pi}{\Lambda} = k_{\text{sup},x}. \tag{4.9}$$

The incident light can also be transmitted without being diffracted at the first interface (i.e. $m = 0$): in this case the light can also propagate through the second interface without diffraction (i.e. $q = 0$) or might be diffracted (i.e. $q = 1$). By neglecting higher diffraction orders, the first transmitted diffraction order has therefore two different contributions: ($m = 1$ and $q = 0$) and ($m = 0$ and $q = 1$). Accordingly, the zeroth diffraction order has also two main contributions: ($m = 0$ and $q = 0$) and ($m = 1$ and $q = -1$). The magnitudes of these contributions are determined by the grating geometry. For example, Hooper and Sambles [264] reported that the total first diffraction order transmitted field with two corrugated interfaces could be weaker

than in the case of a single corrugation, because of the phase difference between the two contributions.

The zeroth and first diffraction order efficiencies around the resonance wavelength are shown in Fig. 4.2b and can be modeled by the asymmetric modulation Fano-like function [265, 266]:

$$T_{0,1} = T_{a_{0,1}} \frac{\left(\omega - \omega_0 + q'\gamma_c\right)^2 + \gamma_i^2}{\left(\omega - \omega_0\right)^2 + \left(\gamma_c + \gamma_i\right)^2},$$

(4.10)

where $T_{a_{0,1}}$ is the transmittance of the continuum of the diffracted orders ($m = 0$, $q = 0$) and ($m = 0$, $q = 1$), ω_0 is the Fano resonance frequency, q' is related to the asymmetry parameter $q = q' \Big/ \left(1 + \frac{\gamma_i}{\gamma_c}\right)$, γ_c and γ_i are the radiative and the non-radiative damping, respectively. In particular, the amplitude of the transmission at resonance depends on the coupling between the mode and the continuum, the intrinsic losses as well as on the amplitude $T_{a_{0,1}}$ of the continuum itself.

Because the scope of this work is to maximize the efficiency T_1, we are studying the influence of two parameters on the T_1 response: the thickness of the metallic layer t_M (Fig. 4.3) and the grating depth d (Fig. 4.4) for a sinusoidal grating. We plot the efficiency of the maximum of T_1 and compare it with the efficiency of T_0 and the absorption at the same wavelength in Figs. 4.3e and 4.4e. The maximum T_1 efficiency is obtained for $d = 25$ nm and $t_M = 50$ nm. Similar simulations with a rectangular grating profile are reported in Appendix C: the rectangular grating has the same thickness t_M at which the first diffraction order transmission is maximum than the sinusoidal grating, but a lower value of the best grating depth d, because the coupling strength is strongly dependent on the grating profile. Because of the staircase approximation in the RCWA model, we have performed a local regression of the results using weighted linear least squares and a first degree polynomial model to minimize local lobes in the results of Fig. 4.3.

Specifically, the losses are due to the near-field coupling between the two different metallic interfaces (Figs. 4.3a and 4.3b) and are reduced if the film thickness is increased. For a fixed modulation depth, related to the coupling efficiency, the intrinsic losses and coupling efficiency are balanced at a specific film thickness, resulting in a maximum of the T_1 peak amplitude (critical coupling condition [267]). Conversely, the amplitude of the continuum T_{a_1} exponentially decreases as a function of the thickness of the metallic layer t_M according to the Beer-Lambert law [268]. Therefore, the balance between the amplitude of the continuum, the coupling strength and the losses determines a maximum in the first diffraction order transmission at $t_M = 50$ nm, which is consistent with other observations reported by Fang et al. [269] and by Giannattasio et al. [270]. For increasing values of the grating depth d, the increasing coupling strength γ_c is also balanced by intrinsic losses at initial coupling. In addition, constructive and destructive interferences in the propagation of diffracted orders are observed (simulations for an extended depth range are shown in Appendix C). The noise in the plots is due to the staircase approximation of the sinusoidal interface in RCWA calculations,
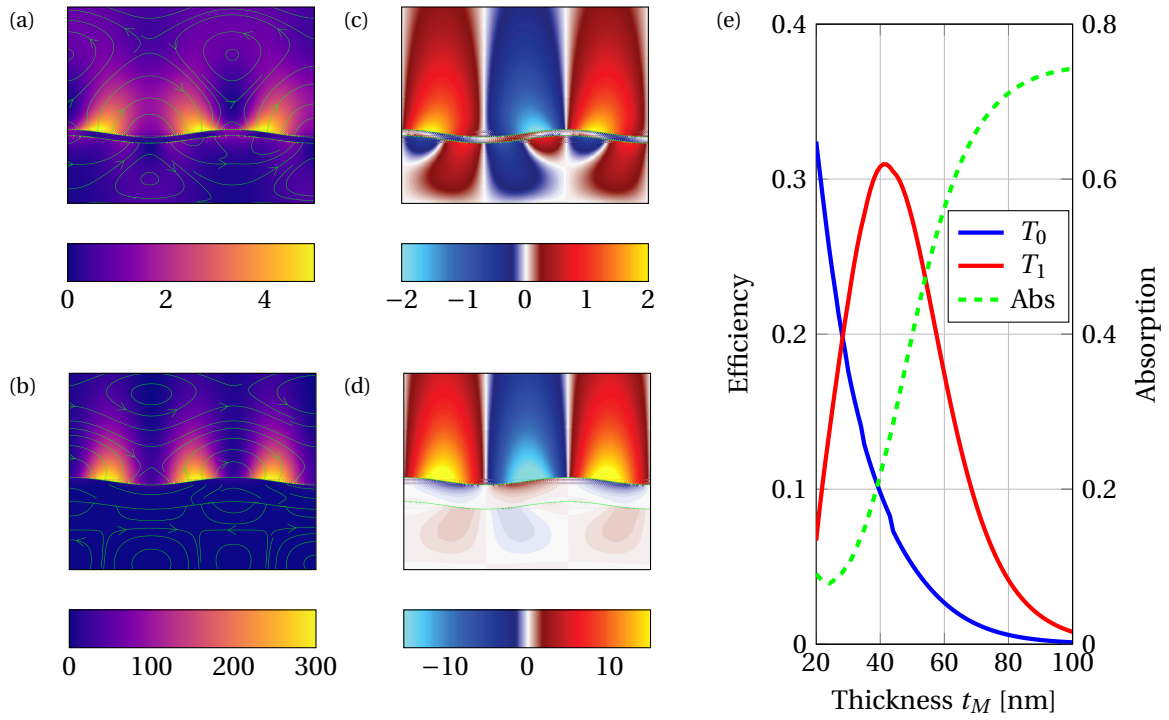
Figure 4.3 – RCWA simulations for different thicknesses of the metallic layer t_M. (a,b) Electric field intensity $|\boldsymbol{E}|^2$ with instantaneous electric field lines and (c,d) steady-state field profiles $\mathrm{Re}[E_x/E_0]$ at two geometries: (a,c) $t_M = 20\,\mathrm{nm}$, $\lambda = 533\,\mathrm{nm}$ (b,d) $t_M = 80\,\mathrm{nm}$, $\lambda = 525\,\mathrm{nm}$. Other parameters: $\Lambda = 500\,\mathrm{nm}$, $d = 25\,\mathrm{nm}$, $t_W = 0\,\mathrm{nm}$, sinusoidal grating profile. (e) Efficiencies T_0, T_1 and absorption at the resonance peak for differ ent thicknesses t_M.

which creates convergence difficulties for such a highly conducting metal grating, and be reduced by decreasing the thickness of each layer.
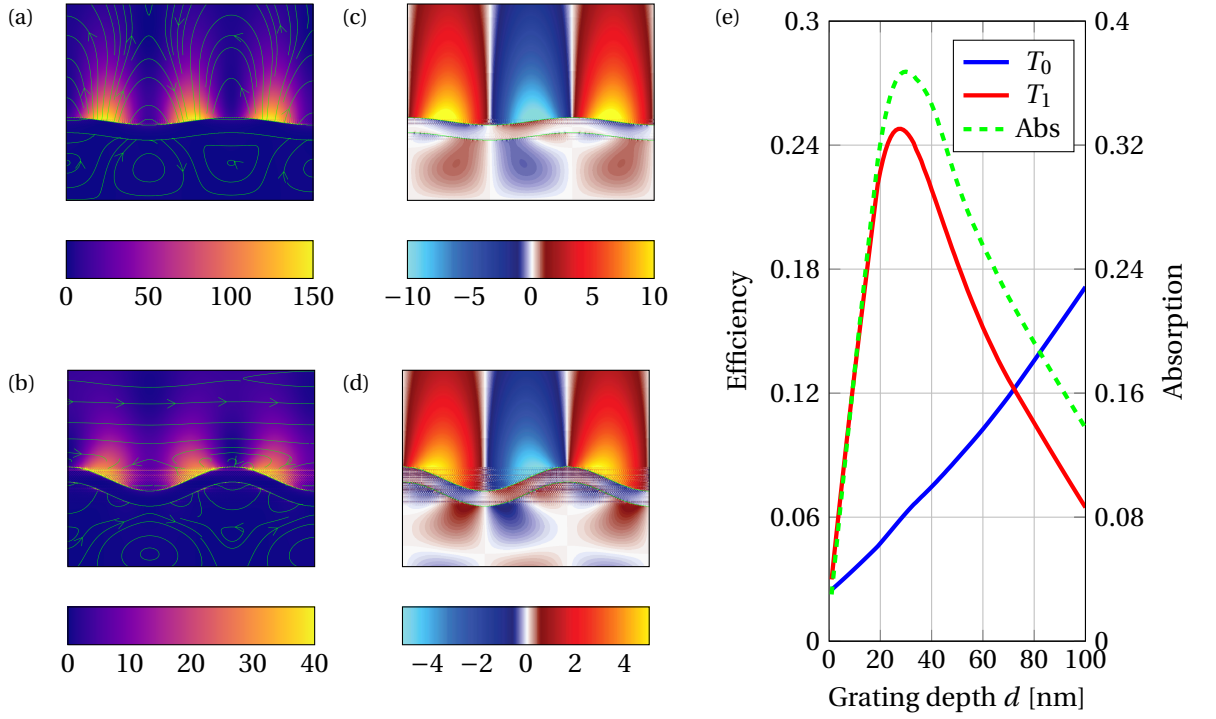
Figure 4.4 – RCWA simulations for different grating depths d. (a,b) Electric field intensity $|\boldsymbol{E}|^2$ with instantaneous electric field lines and (c,d) steady-state field profiles $\mathrm{Re}\,[E_x/E_0]$ at two geometries: (a,c) $d = 25\,\mathrm{nm}$, $\lambda = 525\,\mathrm{nm}$, (b,d) $d = 80\,\mathrm{nm}$, $\lambda = 535\,\mathrm{nm}$. Other parameters: $\Lambda = 500\,\mathrm{nm}$, $t_M = 50\,\mathrm{nm}$, $t_W = 0\,\mathrm{nm}$, sinusoidal grating profile. (e) Efficiencies T_0, T_1 and absorption at the resonance peak for grating depths d.

4.2 Hybrid plasmon-waveguide systems

When a dielectric layer of thickness t_W is added to the plasmonic waveguide, different modes can be excited. A new dispersion equation is derived using the same procedure as in Section 4.1 for TM-polarization:

$$\tanh(k_W t_W) = -\frac{A \tanh(k_M t_M) + B}{C \tanh(k_M t_M) + D}, \tag{4.11}$$

where:

$$\begin{cases} A = k_W n_W^2 \left(k_M^2 n_{\mathrm{sup}}^2 n_{\mathrm{sub}}^2 + k_{\mathrm{sup}} k_{\mathrm{sub}} n_M^4 \right) \\ B = k_W k_M n_W^2 n_M^2 \left(k_{\mathrm{sup}} n_{\mathrm{sub}}^2 + k_{\mathrm{sub}} n_{\mathrm{sup}}^2 \right) \\ C = k_{\mathrm{sub}} k_W^2 n_M^4 n_{\mathrm{sup}}^2 + k_{\mathrm{sup}} k_M^2 n_W^4 n_{\mathrm{sub}}^2 \\ D = k_M n_M^2 \left(k_W^2 n_{\mathrm{sup}}^2 n_{\mathrm{sub}}^2 + k_{\mathrm{sub}} n_{\mathrm{sup}} n_W^4 \right) \end{cases}, \tag{4.12}$$

and:

$$k_W^2 = \beta^2 - n_W^2 k_0^2. \tag{4.13}$$

Dispersion curves for the modes are shown in Fig. 4.5a and compared with RCWA simulations for increasing values of the the waveguide thickness t_W. We observe that the mode TM_0 is red-shifted for increasing values of t_W, and the first order guided mode TM_1 appears at larger t_W values. In this example, both modes are excited with the first diffraction order of the grating, expressed with the superscript [1].

The dielectric layer acts as a dielectric waveguide with a metallic substrate, allowing the excitation of bulk modes and surface modes [259]. Because of the complex refractive index n_M, the propagation constant β has complex values and thus the mode distributions of a dielectric waveguide with a metallic substrate are different compared to the case of a pure dielectric waveguide. In particular, we are interested at the TM_0 mode: it has no cut-off condition and is partly confined at the metal-waveguide interface, as illustrated in Fig. 4.6. In the case of $t_W = 0$, the dispersion relation is reduced to the dispersion relation of a metallic layer discussed in Section 4.1 (Eq. (4.1)).

The dispersion curve for such a surface mode is plotted in Fig. 4.5b for different waveguide thicknesses t_W: in the case of zero thickness the dispersion curve is overlapping the curve of the SPP mode at the air-Ag interface, whereas in case of large thicknesses t_W and t_M the dispersion curve approaches the curve of the SPP mode at SiO_2-Ag interface.

Figure 4.6 shows the simulated electric field distributions and the energy flux for a given set of parameters. In particular, Fig. 4.6a shows the electric field intensity $|\boldsymbol{E}|^2$ where the hot spots (i.e. high field confinement) regions are visible. Figures 4.6c and 4.6d show the real part of the electric field in z and x directions, respectively. In particular, the E_z field indicates the surface charges at the dielectric/metal interface, the signature of a plasmon mode.

As discussed in Section 4.1, the system with the metallic layer only can already be implemented as color-selective coupler. However, the control of the coupled angle is limited to the choice of materials. In fact, by choosing air as superstrate, Ag as metallic layer and SiO_2 as multimode waveguide substrate, the coupled angle θ_{out} is near the total internal reflection (TIR) angle for the SiO_2 substrate, which is around 42°. The additional waveguide layer gives an additional degree of freedom to the system and, in particular, by changing its thickness is also possible to change the coupled angle θ_{out} for the same wavelength. In Fig. 4.7 the simulated and calculated wavelength peaks and coupled angles θ_{out} are plotted, by changing the grating period Λ or the waveguide thickness t_W: the average error between the simulated (a) and calculated (b) wavelengths of the peaks is around 0.7 %. The green lines represent different cases of grating periods, from the left (i.e. $\Lambda = 350$ nm) to the right (i.e. $\Lambda = 950$ nm). Thus, a device with the additional waveguide layer can operate color-selective coupling to higher coupled angles θ_{out}. In Fig. 4.7a the color of the plot is related to the efficiency of the first transmitted diffraction order T_1: the highest efficiencies are obtained between 600 nm
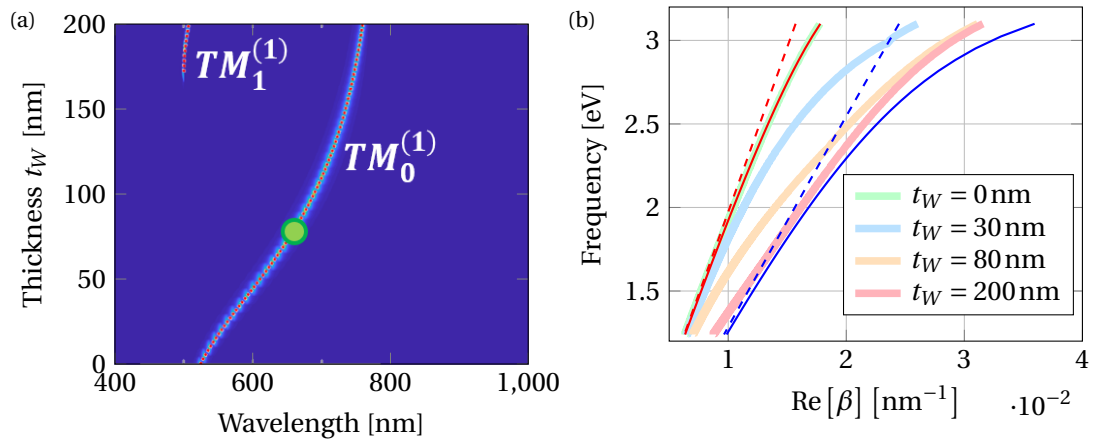
Figure 4.5 – Mode distribution for the hybrid plasmon-waveguides. (a) Simulation (background) and analytical calculation (dashed lines) of the first diffraction order transmission at the resonance peak by varying the waveguide thickness t_W for $\Lambda = 500\,\text{nm}$, $d = 13\,\text{nm}$, $t_M = 50\,\text{nm}$, rectangular grating profile. (b) Dispersion relations for the hybrid modes (pastel lines), for different waveguide thicknesses t_W. Light lines of air (dashed red line) and SiO_2 (dashed blue line). SPP modes for the single air/Ag interface (red line) and SiO_2/Ag interface (blue line).

and 800 nm, for which the coupling conditions in the waveguide mode are optimized. The oscillations of the efficiencies are simulation artifacts related to the layers discretization.

(a) $|\boldsymbol{E}|^2$

(b) S_z at $x = 0\,\mu\mathrm{m}$
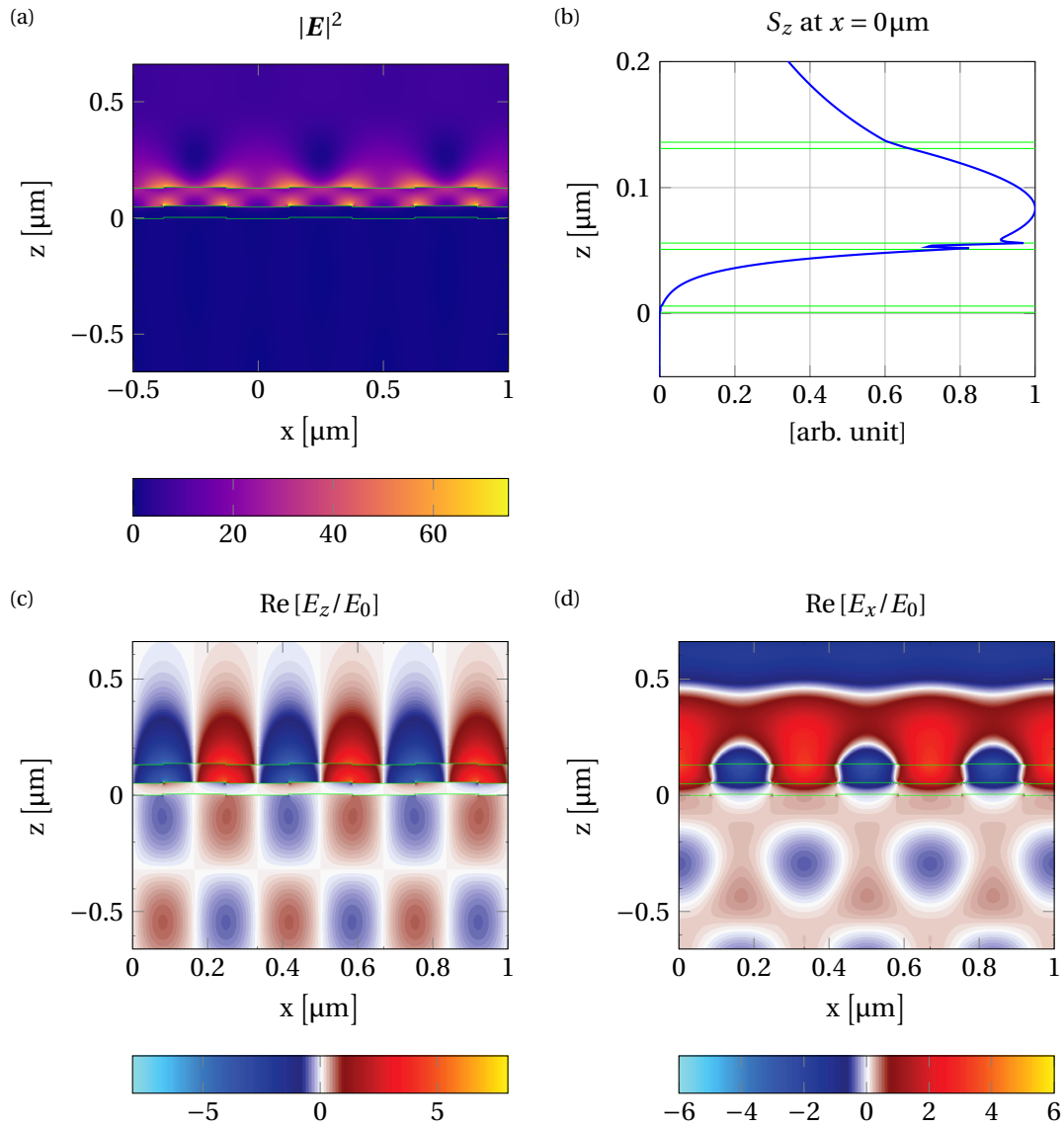
(c) $\mathrm{Re}\,[E_z/E_0]$

(d) $\mathrm{Re}\,[E_x/E_0]$

Figure 4.6 – RCWA simulations at $\lambda = 663\,\mathrm{nm}$, $t_W = 80\,\mathrm{nm}$ of the system in Fig. 4.5a. (a) Electric field intensity $|\boldsymbol{E}|^2$. (b) Section of the energy flux S_z at $x = 0$. (c,d) Steady-state field profiles $\mathrm{Re}\,[E_z/E_0]$ and $\mathrm{Re}\,[E_x/E_0]$, respectively. All the plots have been taken at the same phase (i.e. 75°). The green lines represent the change of the material (a,c,d) and the grating region (b).
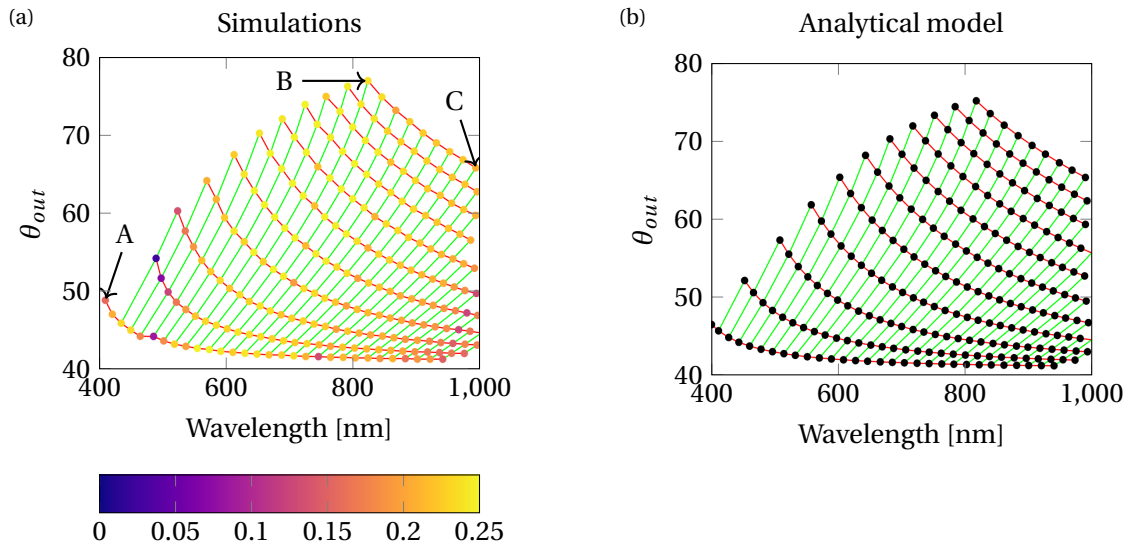
Figure 4.7 – (a) Simulated efficiency T_1 for the first diffraction order transmitted field at its peak, as a function of the grating period Λ and the waveguide thickness t_W. The green and red lines connect geometries with the same grating period Λ and the same waveguide thickness t_W, respectively. The other parameters are: $d = 13\,\mathrm{nm}$, $t_M = 0\,\mathrm{nm}$. Coordinates of the labeled points: A ($\Lambda = 350\,\mathrm{nm}$, $t_W = 0\,\mathrm{nm}$), B ($\Lambda = 550\,\mathrm{nm}$, $t_W = 200\,\mathrm{nm}$), C ($\Lambda = 710\,\mathrm{nm}$, $t_W = 200\,\mathrm{nm}$). (b) Calculated positions of the first order transmitted diffracted field at its peak, for the cases of (a) using the dispersion relation Eq. (4.12).

We fabricated some devices with different grating periods and different grating depths. The fabrication involved the mastering of Si-wafers by electron beam lithography (Raith, EBPG5000ES) with ZEP resist and dry etching (Alcatel, AMS200SE), as detailed in Section 2.4. Each wafer had 8 different patterns of 1D gratings 3 mm × 3 mm, with periods from 300 nm to 1 μm. The wafers were etched at different depths, from 10 nm to 100 nm. Afterwards, the patterns were transferred to SiO_2 substrates by UV-nanoimprint lithography, and then coated with Ag ($t_M = 50$ nm) and SiO_2 ($t_W = 80$ nm) layers by electron beam evaporation (Leybold Optics, LAB600H).

We have then measured the first diffraction order transmission $T1$ for one of those realizations. A broad-spectrum white light covering the whole visible and near-IR spectrum (400 to 1000 nm) was generated with a Halogen Lamp (DL-2000, Ocean Optics) and in-coupled into a fiber with NA = 0.15. The fiber was connected to a parabolic reflective collimator (RC04SMA, Thorlabs) and reduced in diameter with an aperture (3 mm). The system was placed on a motorized rotation stage (CR1-Z7, Thorlabs) to scan the transmission angle. A second motorized rotation stage was placed on top of the previous one. The sample was placed on that second stage with a holder in order to tune the incident angle of the collimated light on the sample. The whole system was then placed on a motorized linear stage (LTS300, Thorlabs) to achieve a higher precision of alignment. A spectroradiometer (Spectrascan PR-730, Photo Research) was used to measure the transmitted light after the sample. A prism was glued with a refractive index matching liquid to the device to outcouple the T_1 scattered light. The transmitted light was recorded from 0° to 90° with steps of 0.5° with the numerical aperture of the spectroradiometer equivalent to 0.5°.The data were then normalized to air and the angular information converted from air to SiO_2 using Snell's law for comparison with simulations, and the efficiency increased with the Fresnel coefficients (by typically 18 %) to take into account the losses at the prism/air interface. The results are shown in Fig. 4.8, with good agreement between simulations and measurements. The lower measured efficiency can be attributed to the scattering during the propagation of the hybrid modes.

Finally, we have studied the behavior of the system under tilted incident light: two different surface modes are excited at different wavelengths and propagating in opposite directions, leading to different contributions to the T_{+1} and T_{-1} diffraction orders. Figure 4.9 shows the energy-momentum dispersion diagram for such a system: it is possible to excite these different modes for a broad variety of incident angles. As example, in Fig. 4.10 we report the distribution of the diffracted peaks for a divergent angle of incidence θ_{in}: a broadband portion of the spectrum is out-coupled from the device into different substrate modes at different angles θ_{out}. In particular, this allows a clear dispersion of the diffracted beam even if the incident polychromatic light is divergent.
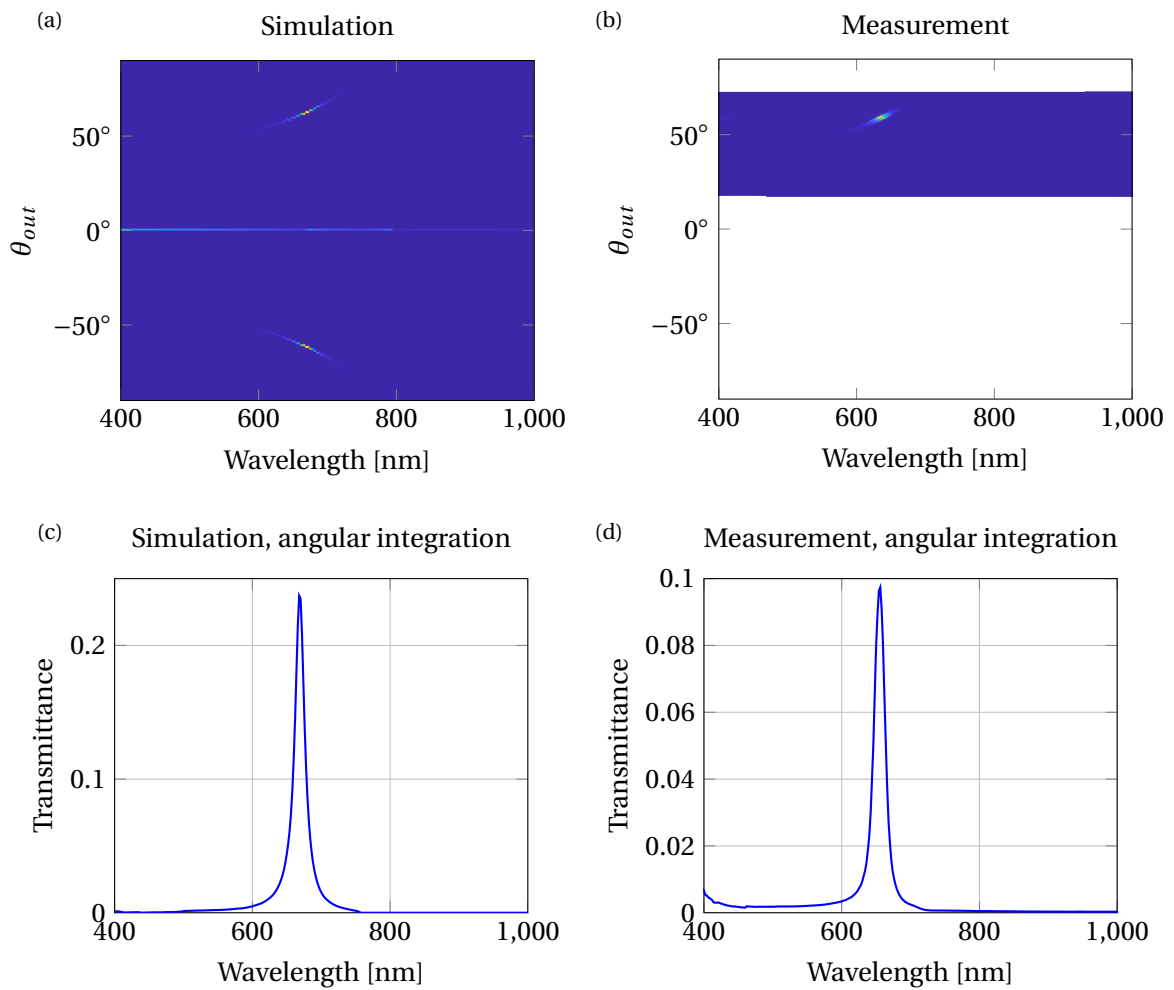
Figure 4.8 – (a,c) Simulations and (b,d) measurements of the first diffraction order transmittance, integrated every 0.5°. The plots in (c,d) show the integrated transmittance around the diffracted peak. The parameters for the fabricated device are: $d = 45\,\text{nm}$, $t_W = 80\,\text{nm}$, $t_M = 50\,\text{nm}$.

(a)

T_{+1}

(b)

T_{-1}
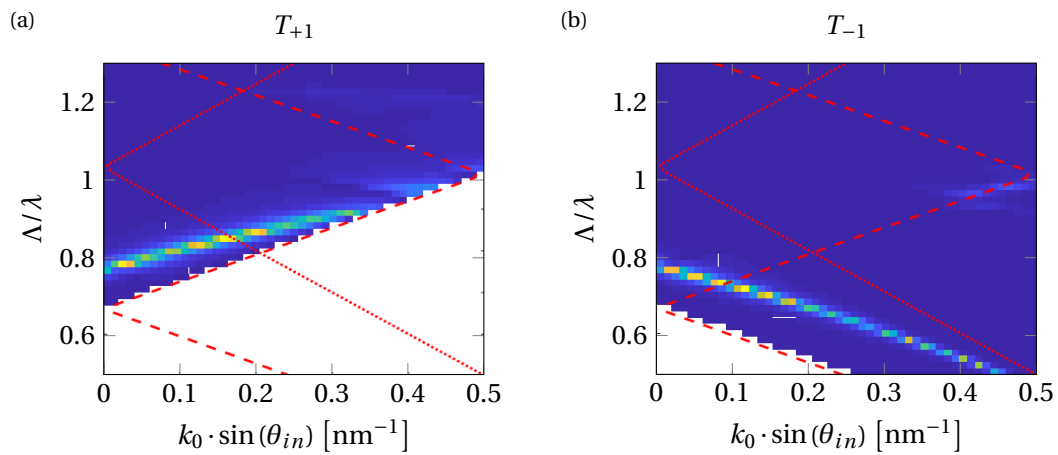
Figure 4.9 – Energy-momentum dispersion diagrams of the device as in Fig. 4.8 for each first diffraction order transmission. The red dashed lines represent the folded light line of the air and of the SiO$_2$ (the finest and the coarsest one, respectively).

(a)

(b)
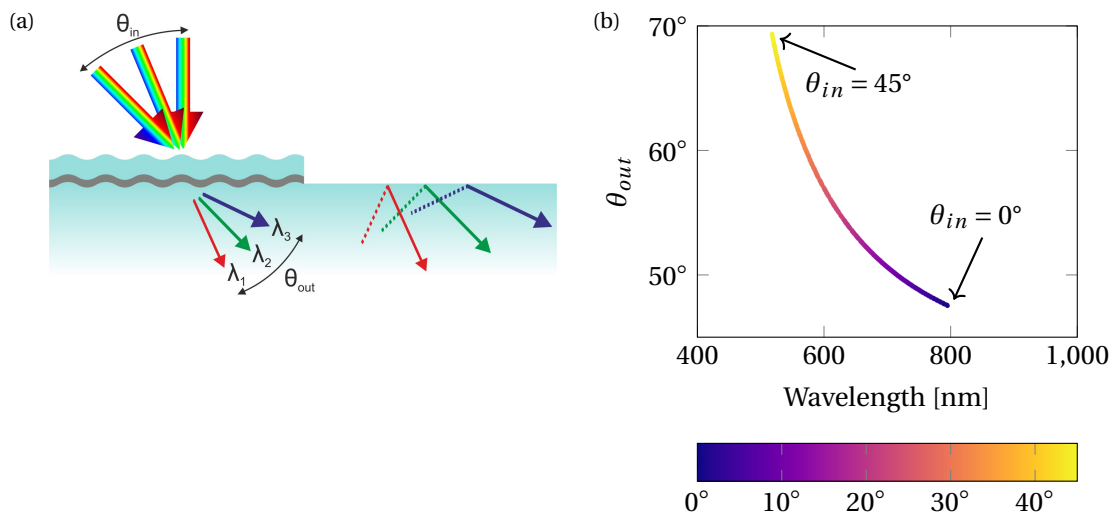
Figure 4.10 – (a) Schematic and (b) calculations of the angular dispersion θ_{out} of the device for different angles of incidence θ_{in} from 0° to 45°. Parameters: $\Lambda = 700$ nm, $t_L = 60$ nm, $t_M = 50$ nm.

4.3 Conclusions

We presented and discussed a color-selective optical coupler, which can be used as dispersive element when the white light source is divergent. Thanks to its ease of fabrication, which requires only one nanoimprint step and two evaporation steps, the coupler is fully compatible with large scale and up-scalable industrial applications. It is further possible to engineer devices that share the same materials and layers thicknesses but have different wavelength incoupled, by having different grating periods. Further developments could rely on 2D gratings or advanced patterns, to improve the efficiency under unpolarized light and achieve higher angular tunability. Furthermore, the efficiency might be increased by having a tilted evaporation of the metallic layer or using blazed gratings [271] or by exploiting long range SPPs with thinner metallic layers. The study of this system under TE polarized light could also be of interest, because the resonance-induced absorption can produce even narrower features for the same geometry without surface plasmon resonances [272]. The device can also be implemented in a reciprocal configuration to outcouple light from a multimode waveguide. Applications are foreseen in many optical devices that require color-selective coupling or dispersive properties, such as optical document security or near-eye displays. Moreover, the dispersion behavior a under divergent light source can be utilized to design inexpensive, compact and robust spectrometers.

5 Conclusion and Outlook

In this thesis, resonant waveguide gratings (RWGs) has been investigated to achieve color-selective diffraction beam redirection. In particular, I have studied two different configurations of RWGs. The first configuration consists of a pair of finite size impedance matched RWGs with different grating periods but sharing the same corrugated substrate and coated waveguide, where the first RWG acts as in-coupler and the second acts as out-coupler. This configuration can selectively filter and redirect spectral portions of the incoming light, either in transmission or in reflection. The second configuration is based on a corrugated substrate with a coated metallic and dielectric layer. Hybridized SPPs and waveguide modes, which lie at the metallic/dielectric interface, can be transferred at the metallic/substrate interface and radiated at the first diffraction order transmission in the thick substrate, where they are coupled in. Both configurations can operate under unpolarized white light and low-coherence source. Moreover, the studied structures exhibit good color tunability and are made by only one NIL replication and one or two thin film layer depositions, such that their fabrication is compatible with up-scalable fabrication processes and are well-suited for industrial applications, where high throughput is required.

The paired RWG of the first configuration can be periodically repeated to create a diffraction pattern that follows the super period; a surface can also be patterned with different paired-RWGs to re-focus a point-like source into another point, viz. the observation point. To create such a pattern, I developed a design method based on confocal prolate spheroids, which can efficiently predict the periods and the orientation angles of the different RWGs. Moreover, I have conceived and fabricated realizations for optical security application based on smartphone authentication. In particular, the flash of the smartphone is filtered and re-focused on the camera of the smartphone, showing a colorful motif, whereas the pattern remains almost invisible by naked eye. The proposed methodology can be applied to realize passive beam redirecting structures for a variety of other applications. When one focal point is set to infinity, multifocal (i.e., different colors focused in specific positions), or monochromatic lenses can be designed with a system of confocal paraboloids. This method could also be implemented in gas sensing, where a pattern appears on the smartphone only when no gas

is detected, in refractive-index sensing [7], or in absorption sensing [87]. Furthermore, see-through optical combiners for near-eye displays could be designed by redirecting the light from a microprojector (in the position of the point source f_s) to the human eye (in the position of the observer f_o) [251]. Further developments include the possibility of using ultrathin metallic waveguides or combined metallic/dielectric waveguides, implementing a 2D grating, or creating the pattern on a non-planar surface.

The second configuration, based on hybridized plasmon waveguide modes, can be used as a dispersive element when the white light source is divergent. It is possible to engineer devices that share the same materials and layers thicknesses but has different wavelength incoupled by having different grating periods. Further developments could rely on 2D gratings or advanced patterns to improve the efficiency under unpolarized light and achieve higher angular tunability. Furthermore, the efficiency might be increased by having a tilted evaporation of the metallic layer or using blazed gratings [271]. The study of the system under TE polarized light can also be of interest, because the resonance-induced absorption can produce even narrower features for the same geometry [272]. The device can also be implemented in a reciprocal configuration to outcouple the light from a multimode waveguide. Applications are foreseen in many optical devices that require color-selective coupling or dispersive properties, such as optical document security, near-eye displays or spectrometers.

The optimization of the electron beam lithography presented in this thesis has been a key step to guarantee a feasible fabrication of these different optical elements. In particular, a pre-fracturing of the grating lines in one or more smaller stripes, depending on the grating period, was first implemented, followed by the fracturing using a beam step size smaller than the beam diameter. This method is beneficial to efficiently fabricate gratings with different periods and oriented at different angles. This fracturing technique enables the exposure of complex surfaces with a larger electron beam than with standard grating fracturing approaches in less than 5 hours per cm^2, while a conventional electron beam writing would have taken more than 20 hours per cm^2 to achieve the same quality. Further improvements in the exposure time could be achieved by means of advanced electron beam configurations, such as a variable shape beam or a multi column beam [237, 238], or by direct laser writing with deep or extreme ultraviolet light [239].

The drive for innovation in many fields, such as optical security, spectroscopy or biosensing is leading scientists and engineers to search for more advanced implementations of RWGs [79, 179]. Moreover, emerging fields such as augmented or mixed reality and wearable electronics are amazing opportunities to develop very sophisticated devices that should be more efficient, less costly and more compact than the current technologies. For that, novel neural network algorithms and machine learning might be required to design the next generation of advanced resonant waveguide structures.

A Matlab scripts

A.1 Lumerical code to perform the far-field extraction and the angular integration

```
1  clear;
2  closeall;
3  wavelength_range=400e-9:2e-9:801e-9;
4  theta=6;
5  name_test="20170405_24nm_15deg_100_50";
6
7  status = layoutmode;
8  if (status == 0) {
9  switchtolayout;
10 }
11 main_dir=pwd;
12 matlabload("ormo_zns_material.mat");
13
14 # get the transmission coefficient
15 f = c/wavelength_range; # frequency vector
16 d = [0; 0]; # layer thickness
17 nf = length(f);
18 nd = length(d);
19 n2 = matrix(nd,nf);
20 n2(1,1:nf) = 1; # air
21 n2(2,1:nf) = getfdtdindex("SiO2 (Glass) - Palik",f,min(f),max(f));
22 air_glass = stackrt(n2,d,f,theta);
23 n2(1,1:nf) = getfdtdindex("SiO2 (Glass) - Palik",f,min(f),max(f));
24 n2(2,1:nf) = n_ormo(find(wave_mat,wavelength_range*1e6));
25 glass_ormo = stackrt(n2,d,f,theta);
26 n2(1,1:nf) = n_ormo(find(wave_mat,wavelength_range*1e6));
27 n2(2,1:nf) = getfdtdindex("SiO2 (Glass) - Palik",f,min(f),max(f));
28 ormo_glass = stackrt(n2,d,f,theta);
29 n2(1,1:nf) = getfdtdindex("SiO2 (Glass) - Palik",f,min(f),max(f));
30 n2(2,1:nf) = 1; # air
31 glass_air = stackrt(n2,d,f,theta);
32 total_stack_Ts=air_glass.Ts*glass_ormo.Ts*ormo_glass.Ts*glass_air.Ts;
33
34 for (periods=1){#[1:10;20:10:100;200:100:1000;2000:1000:10000]){
35 # get the far field
36 n=2000; #number of points in the far field
```

```matlab
37  illumination=2; # 1=Gaussian, 2=plain wave
38  #periods=4; # number of periods to be used
39  index=1; # index of the material in the far field
40  direction=1; # direction of the max power flow
41  ff_transmission=matrix(length(wavelength_range),n);
42  total_transmission=matrix(length(wavelength_range));
43  ff_reflection=matrix(length(wavelength_range),n);
44  total_reflection=matrix(length(wavelength_range));
45  count_tot=1;
46  for (counter_wave=wavelength_range){
47  count_wave_mat=find(wave_mat,counter_wave*1e6);
48  f_name=name_test+"_sim_"+num2str(counter_wave*1e9)+"nm";
49  ?"analysing simulation " + f_name + " for periods="+num2str(periods);
50  load("Simulations\\"+f_name);
51  cd(main_dir);
52  temp_t=farfield2d("transmission_monitor",1,n,illumination,periods,index,direction
        );
53  temp_r=farfield2d("reflection_monitor",1,n,illumination,periods,index,-direction)
        ;
54  #temp_t=sum(abs(temp_t)^2,2); # E2 = |Ex|^2 + |Ey|^2 + |Ez|^2
55  ff_transmission(count_tot,1:n)=transpose(temp_t);
56  ff_reflection(count_tot,1:n)=transpose(temp_r);
57  total_transmission(count_tot)=transmission("transmission_monitor")*total_stack_Ts
        (count_tot);
58  total_reflection(count_tot)=1-transmission("reflection_monitor")*total_stack_Ts(
        count_tot);
59  count_tot=count_tot+1;
60  }
61  angle_t=farfieldangle("transmission_monitor",1,n,index);
62  angle_r=farfieldangle("reflection_monitor",1,n,index);
63  closeall;
64  image(wavelength_range*1e9,angle_t,log10(ff_transmission),"Wavelength (nm)","
        angle (deg)","|E|^2 far field Transmission");
65  image(wavelength_range*1e9,angle_r,log10(ff_reflection),"Wavelength (nm)","angle
        (deg)","|E|^2 far field Reflection");
66  plot(wavelength_range*1e9,total_transmission,"Wavelength (nm)","Transmission");
67  plot(wavelength_range*1e9,total_reflection,"Wavelength (nm)","Reflection");
68  plot(wavelength_range*1e9,total_reflection+total_transmission,"Wavelength (nm)","
        Sum");
69
70  step_angles=0.5; # step angle in deg
71  angle_t_integrated=-90:0.5:90;
72  ff_transmission_integrated=matrix(length(wavelength_range),length(
        angle_t_integrated));
73  temp_angle=1;
74  for (count_angle=angle_t_integrated){
75  temp_wave=1;
76  for (count_wave=1:length(wavelength_range)){
77  ff_transmission_integrated(temp_wave,temp_angle)=farfield2dintegrate(pinch(
        ff_transmission,1,count_wave),angle_t,step_angles/2,count_angle);
78  temp_wave=temp_wave+1;
79  }
80  temp_angle=temp_angle+1;
81  }
82  angle_r_integrated=-90:0.5:90;
83  ff_reflection_integrated=matrix(length(wavelength_range),length(
        angle_r_integrated));
84  temp_angle=1;
85  for (count_angle=angle_r_integrated){
86  temp_wave=1;
```

94

```
87  for (count_wave=1:length(wavelength_range)){
88  ff_reflection_integrated(temp_wave,temp_angle)=farfield2dintegrate(pinch(
       ff_reflection,1,count_wave),angle_t,step_angles/2,count_angle);
89  temp_wave=temp_wave+1;
90  }
91  temp_angle=temp_angle+1;
92  }
93  image(wavelength_range*1e9,angle_t_integrated,log10(ff_transmission_integrated),"
       Wavelength (nm)","angle (deg)","|E|^2 far field Transmission");
94  image(wavelength_range*1e9,angle_r_integrated,log10(ff_reflection_integrated),"
       Wavelength (nm)","angle (deg)","|E|^2 far field Reflection");
95
96  matlabsave("Data Extraction\\"+name_test+"_simulation_output_ffperiods_"+num2str(
       periods),ff_transmission,ff_reflection,total_transmission,total_reflection,
       angle_t,angle_r,wavelength_range,ff_transmission_integrated,
       ff_reflection_integrated,angle_t_integrated,angle_r_integrated);
97  cd(main_dir);
98  ?"Matlab file saved, script ended";
99  }
```

A.2 Matlab code to perform the the angular integration

```
1   function [RT_x2,angles]=angular_integration(scat_field,R,T,delta_angle,wavelength
       )
2   % Angle extraction from wavevectors
3   theta_t=zeros(size(scat_field,2),size(scat_field(1).f1t,1));
4   theta_r=zeros(size(theta_t));
5   for i=1:size(theta_t,1)
6   theta_t(i,:)=atan(scat_field(i).f2./scat_field(i).f1t);
7   theta_r(i,:)=atan(scat_field(i).f2./scat_field(i).f1r);
8   end
9   % Variables initialization
10  theta_r(~~imag(theta_r))=nan;
11  theta_t(~~imag(theta_t))=nan;
12  angles=-90+mod(90,delta_angle):delta_angle:90;
13  Rx2_TE = zeros(length(angles),length(wavelength));
14  Rx2_TM = zeros(size(Rx2_TE));
15  Tx2_TE = zeros(size(Rx2_TE));
16  Tx2_TM = zeros(size(Rx2_TE));
17  % Efficiency counting
18  for i=1:size(theta_t,1)
19  for j=1:size(theta_t,2)
20  if ~isnan(theta_r(i,j))
21  [~,pos]=min(abs(theta_r(i,j)*180/pi-angles));
22  Rx2_TE(pos,j)=Rx2_TE(pos,j)+R(i).eff1(j);
23  Rx2_TM(pos,j)=Rx2_TM(pos,j)+R(i).eff2(j);
24  end
25  if ~isnan(theta_t(i,j))
26  [~,pos]=min(abs(theta_t(i,j)*180/pi-angles));
27  Tx2_TE(pos,j)=Tx2_TE(pos,j)+T(i).eff1(j);
28  Tx2_TM(pos,j)=Tx2_TM(pos,j)+T(i).eff2(j);
29  end
30  end
31  end
32  % Results extraction
33  RT_x2.Rx2_TE=Rx2_TE;
34  RT_x2.Rx2_TM=Rx2_TM;
```

```
35  RT_x2.Tx2_TE=Tx2_TE;
36  RT_x2.Tx2_TM=Tx2_TM;
37  RT_x2.angles=angles;
38  end
```

B Design parameters

Parameter name	Value	Units
Λ_1	380	nm
Λ_2	310	nm
t	24	nm
n_{W}	ZnS	
n_{clad}	Ormocomp	
ϕ_{in}	0	deg

Table B.1 – Design #1 linear array of the same double RWGs with no distance between cells.

Parameter name	Value	Units
Λ_1	410	nm
Λ_2	300	nm
t	30	nm
n_W	ZnS	
n_clad	Ormocomp	
ϕ_in	0	deg

Table B.2 – Design #2 linear array of the same double RWGs with no distance between cells.

Parameter name	Value	Units
$f_s\ (x,y,z)$	(-7.5,0,0)	mm
$f_o\ (x,y,z)$	(7.5,0,0)	mm
λ	655	nm
$\Sigma\ (x,y,z)$	(-80:80,-80:80,-80)	mm
n_W	ZnS	
$n_\text{SUB} = n_\text{SUP}$	Ormocomp	
t	80	nm
Ψ	Tangent to its section of prolate spheroid	

Table B.3 – Design #3: parameters for a test pattern to compare the design method with the analytical model.

Parameter name	Value	Units
$f_s\ (x,y,z)$	(-7.5,0,0)	mm
$f_o\ (x,y,z)$	(7.5,0,0)	mm
λ	655	nm
$\Sigma\ (x,y,z)$	(-80:80,-80:80,-80)	mm
n_W	ZnS	
$n_\text{SUB} = n_\text{SUP}$	Ormocomp	
t	80	nm
Ψ	0	deg

Table B.4 – Design #4: parameters for a test pattern to compare the design method with the analytical model.

Parameter name	Value	Units
f_s (x,y,z)	(-7.5,0,0)	mm
f_o (x,y,z)	(7.5,0,0)	mm
λ	655	nm
Σ (x,y,z)	(-80:80,-80:80,-80)	mm
n_W	ZnS	
$n_{SUB} = n_{SUP}$	Ormocomp	
t	80	nm
Ψ	90	deg

Table B.5 – Design #5: parameters for a test pattern to compare the design method with the analytical model.

Parameter name	Value	Units
f_s (x,y,z)	(-5,0,0)	mm
f_o (x,y,z)	(5,0,0)	mm
λ	#6: 630, #7: 480, #8: 535	nm
Σ (x,y,z)	#6: (-17:-7,10:20,-65), #7: (-5:5,10:20,-65), #8: (7:17,10:20,-65)	mm
n_W	ZnS	
$n_{SUB} = n_{SUP}$	Ormocomp	
t	70	nm
Ψ	Tangent to its section of prolate spheroid	

Table B.6 – Design #6,#7,#8: parameters for the design of three squares with uniform red, blue or green color.

C | Supplementary results of Chapter 4

C.1   Numerical simulations

RCWA simulations similar for those reported in Section 4.1, but with rectangular grating profiles have also been performed and the results are shown in Fig. C.1. In comparison with the sinusoidal profile (reported in Figs. 4.3 and 4.4), the rectangular grating has the same thickness t_M for the first diffraction order transmission maximum. This is because the losses in the metallic layer are barely related to the interfaces profile. Conversely, the best grating depth d has a lower value ($d = 13$ nm compared to $d = 25$ nm for a sinusoidal profile) because the coupling strength strongly depends on the grating profile.

Furthermore, we report in Fig. C.2 the full results of the simulations shown in Fig. 4.4e, i.e. for an extended range of grating depth d and including the whole computed spectrum. The thickness of the discretized layers has been increase every 100 nm to keep a feasible computation time: this explains the horizontal variations in the spectrum every 100 nm. In Figs. C.2a and C.2b the presence of an interference pattern is visible, which influence the efficiency of T_0 and T_1 orders. In Fig. C.2b the Rayleigh anomaly at $\lambda_{Ra} = n_{sub} \cdot \Lambda = 769$ nm prevents any diffraction in the substrate for wavelengths larger than λ_{Ra}. The same anomaly is also visible in Fig. C.2c in the case of the superstrate (air): $\lambda_{Ra} = n_{sub} \cdot \Lambda = 500$ nm. In Fig. C.3 simulations for different metallic layer thickness t_M are shown.

Figure C.1 – Simulated efficiencies T_0, T_1 and absorption at the resonance peak for different (a,b) silver layer thicknesses t_M and (c,d) grating depths d for a rectangular grating profile. Parameters: $\Lambda = 500\,\text{nm}$, $t_W = 0\,\text{nm}$, $t_M = 50\,\text{nm}$, $d = 13\,\text{nm}$.
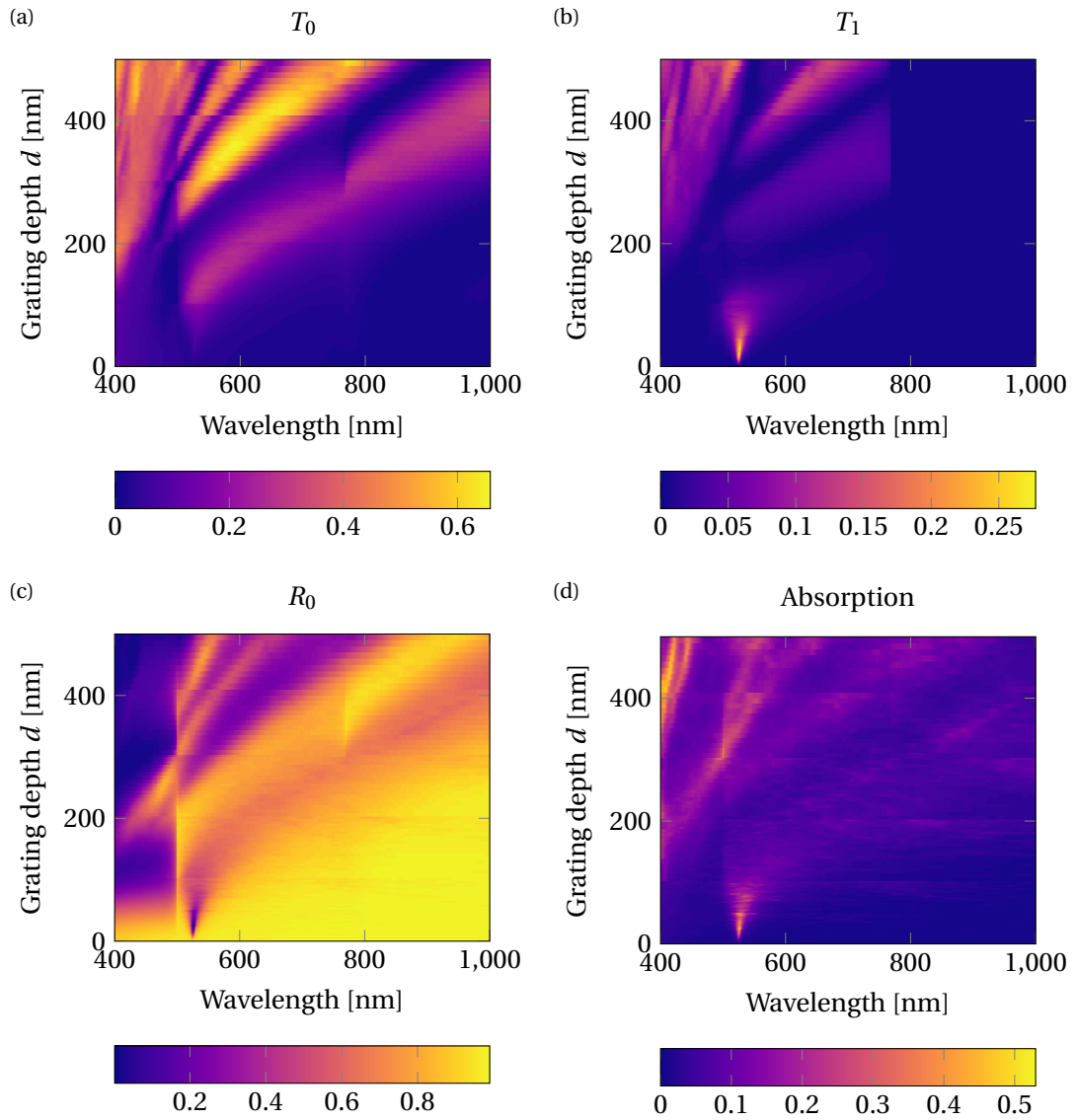
Figure C.2 – Simulated efficiencies T_0, T_1, R_0 and absorption for different grating depths d. Parameters: $\Lambda = 500\,\text{nm}$, $t_W = 0\,\text{nm}$, $t_M = 50\,\text{nm}$, sinusoidal grating profile.
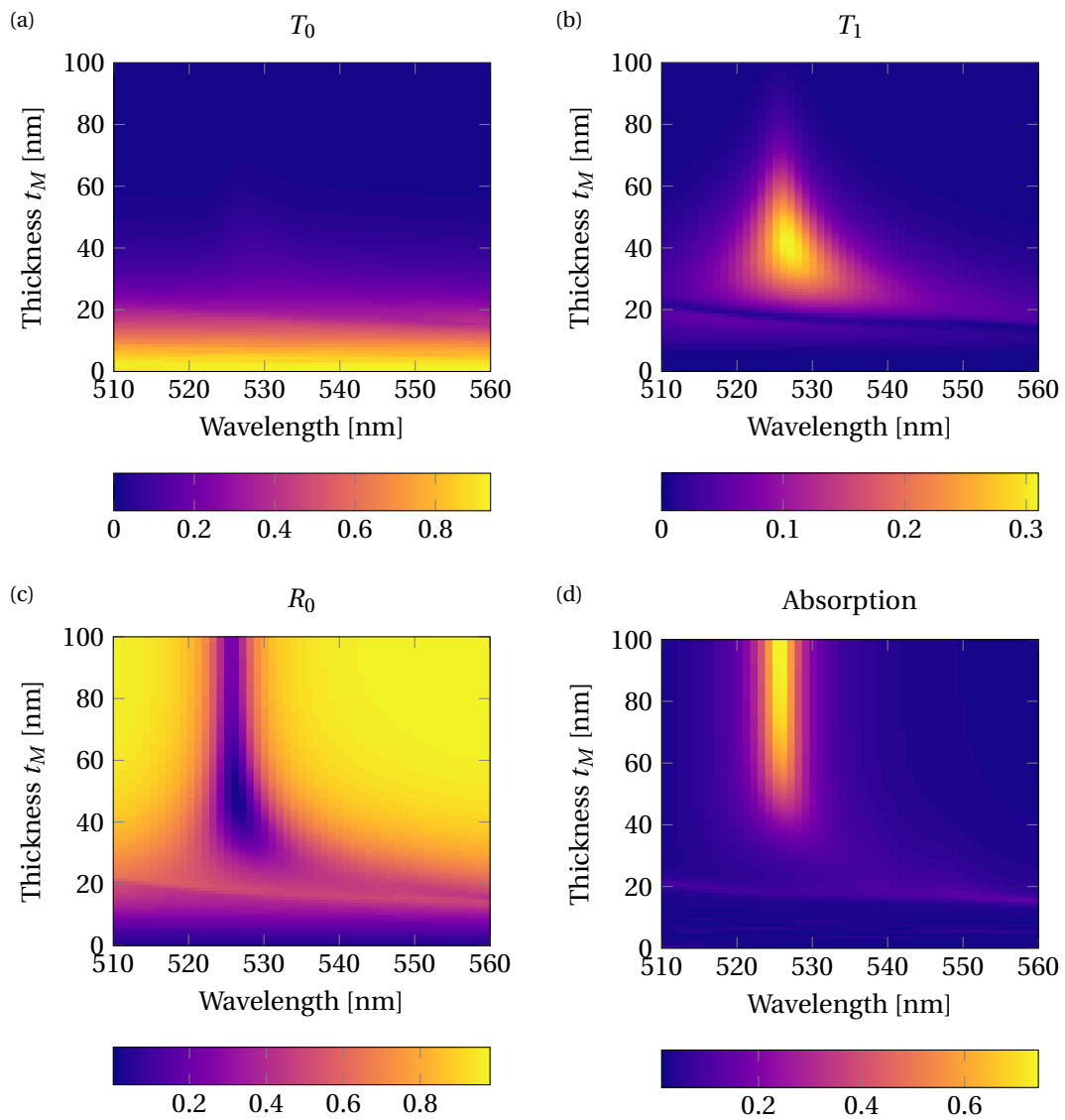
Figure C.3 – Simulated efficiencies T_0, T_1, R_0 and absorption for different metallic layer thickness t_M. Parameters: $\Lambda = 500\,\text{nm}$, $t_W = 0\,\text{nm}$, $d = 25\,\text{nm}$, sinusoidal grating profile.

C.2 Derivation of the dispersion relation of the hybridized plasmon waveguide system
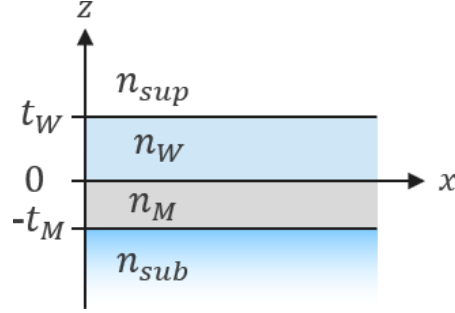

Figure C.4 – Geometry of a four layer system, where two layers have finite thickness and two layers are half space.

In this section the dispersion relation of Eq. (4.11) is derived. We start considering a geometry of a four-layer system as in Fig. C.4. The solution of the propagating wave in TM polarization has the following field components for $z > t_W$ [273]:

$$
\begin{cases}
H_y = A e^{i\beta x} e^{-k_{\text{sup}} z} \\[2mm]
E_x = i A \dfrac{1}{\omega \varepsilon_0 \varepsilon_{\text{sup}}} k_{\text{sup}} e^{i\beta x} e^{-k_{\text{sup}} z} \\[2mm]
E_z = -A \dfrac{\beta}{\omega \varepsilon_0 \varepsilon_{\text{sup}}} e^{i\beta x} e^{-k_{\text{sup}} z}
\end{cases}
,
\qquad (\text{C.1})
$$

for $t_W < z < 0$:

$$
\begin{cases}
H_y = B e^{i\beta x} e^{k_W z} + C e^{i\beta x} e^{-k_W z} \\[2mm]
E_x = -i B \dfrac{1}{\omega \varepsilon_0 \varepsilon_W} k_W e^{i\beta x} e^{k_W z} + i C \dfrac{1}{\omega \varepsilon_0 \varepsilon_W} k_W e^{i\beta x} e^{-k_W z} \\[2mm]
E_z = B \dfrac{\beta}{\omega \varepsilon_0 \varepsilon_W} e^{i\beta x} e^{k_W z} + C \dfrac{\beta}{\omega \varepsilon_0 \varepsilon_W} e^{i\beta x} e^{-k_W z}
\end{cases}
,
\qquad (\text{C.2})
$$

for $0 < z < -t_M$:

$$
\begin{cases}
H_y = D e^{i\beta x} e^{k_M z} + E e^{i\beta x} e^{-k_M z} \\[2mm]
E_x = -i D \dfrac{1}{\omega \varepsilon_0 \varepsilon_M} k_M e^{i\beta x} e^{k_M z} + i E \dfrac{1}{\omega \varepsilon_0 \varepsilon_M} k_M e^{i\beta x} e^{-k_M z} \\[2mm]
E_z = D \dfrac{\beta}{\omega \varepsilon_0 \varepsilon_M} e^{i\beta x} e^{k_M z} + E \dfrac{\beta}{\omega \varepsilon_0 \varepsilon_M} e^{i\beta x} e^{-k_M z}
\end{cases}
,
\qquad (\text{C.3})
$$

105

for $z < -t_M$:

$$\begin{cases} H_y = F e^{i\beta x} e^{k_{sub} z} \\ E_x = -iF \dfrac{1}{\omega \varepsilon_0 \varepsilon_{sub}} k_{sub} e^{i\beta x} e^{k_{sub} z} \\ E_z = -F \dfrac{\beta}{\omega \varepsilon_0 \varepsilon_{sub}} e^{i\beta x} e^{k_{sub} z} \end{cases} , \qquad (C.4)$$

where k_{sup}, k_W, k_M and k_{sub} are the component of the wave vector perpendicular to the interface in the different media and $\varepsilon_{sup} = n_{sup}^2$, $\varepsilon_W = n_W^2$, $\varepsilon_M = n_M^2$, $\varepsilon_{sub} = n_{sub}^2$. The continuity at the three interfaces of H_y and E_x leads to a linear system M of six equations and six variables (i.e. A to F):

$$M \times \begin{pmatrix} A \\ \vdots \\ F \end{pmatrix} = 0. \qquad (C.5)$$

It is possible to find the dispersion equation of the system by imposing $\det M = 0$, so that the solutions are non-trivial:

$$\begin{aligned} k_L^2 \cdot k_{sub} \cdot n_M^4 \cdot n_{sup}^2 \cdot \sinh(k_L \cdot t_L) \cdot \sinh(k_M \cdot t_M) & \\ + k_M^2 \cdot k_{sup} \cdot n_L^4 \cdot n_{sub}^2 \cdot \sinh(k_L \cdot t_L) \cdot \sinh(k_M \cdot t_M) & \\ + k_L \cdot k_M^2 \cdot n_L^2 \cdot n_{sub}^2 \cdot n_{sup}^2 \cdot \cosh(k_L \cdot t_L) \cdot \sinh(k_M \cdot t_M) & \\ + k_L^2 \cdot k_M \cdot n_M^2 \cdot n_{sub}^2 \cdot n_{sup}^2 \cdot \cosh(k_M \cdot t_M) \cdot \sinh(k_L \cdot t_L) & \\ + k_L \cdot k_{sub} \cdot k_{sup} \cdot n_L^2 \cdot n_M^4 \cdot \cosh(k_L \cdot t_L) \cdot \sinh(k_M \cdot t_M) & \\ + k_M \cdot k_{sub} \cdot k_{sup} \cdot n_L^4 \cdot n_M^2 \cdot \cosh(k_M \cdot t_M) \cdot \sinh(k_L \cdot t_L) & \\ + k_L \cdot k_M \cdot k_{sub} \cdot n_L^2 \cdot n_M^2 \cdot n_{sup}^2 \cdot \cosh(k_L \cdot t_L) \cdot \cosh(k_M \cdot t_M) & \\ + k_L \cdot k_M \cdot k_{sup} \cdot n_L^2 \cdot n_M^2 \cdot n_{sub}^2 \cdot \cosh(k_L \cdot t_L) \cdot \cosh(k_M \cdot t_M) = 0 & \end{aligned} , \qquad (C.6)$$

which can be rewritten as:

$$\tanh(k_W t_W) = -\frac{G \tanh(k_M t_M) + H}{I \tanh(k_M t_M) + J}, \qquad (C.7)$$

where:

$$\begin{cases} G = k_W n_W^2 \left(k_M^2 n_{sup}^2 n_{sub}^2 + k_{sup} k_{sub} n_M^4 \right) \\ H = k_W k_M n_W^2 n_M^2 \left(k_{sup} n_{sub}^2 + k_{sub} n_{sup}^2 \right) \\ I = k_{sub} k_W^2 n_M^4 n_{sup}^2 + k_{sup} k_M^2 n_W^4 n_{sub}^2 \\ J = k_M n_M^2 \left(k_W^2 n_{sup}^2 n_{sub}^2 + k_{sub} n_{sup} n_W^4 \right) \end{cases} . \qquad (C.8)$$

Equation (C.7) is the dispersion equation of the system.

Bibliography

[1] G. Quaranta, G. Basset, O. J. F. Martin, and B. Gallinet, "Recent Advances in Resonant Waveguide Gratings", Laser & Photonics Reviews **12**, 1800017 (2018).

[2] R. W. Wood, "On a Remarkable Case of Uneven Distribution of Light in a Diffraction Grating Spectrum", Proceedings of the Physical Society of London **18**, 00439, 269–275 (1902).

[3] L. Rayleigh, "On the Dynamical Theory of Gratings", Proceedings of the Royal Society of London. Series A, Containing Papers of a Mathematical and Physical Character **79**, 399–416 (1907).

[4] U. Fano, "The Theory of Anomalous Diffraction Gratings and of Quasi-Stationary Waves on Metallic Surfaces (Sommerfeld's Waves)", JOSA **31**, 213–222 (1941).

[5] D. Maystre, "Sur la diffraction d'une onde plane par un reseau metallique de conductivite finie", Optics Communications **6**, 50–54 (1972).

[6] M. Neviere, R. Petit, and M. Cadilhac, "About the theory of optical grating coupler-waveguide systems", Optics Communications **8**, 113–117 (1973).

[7] K. Schmitt and C. Hoffmann, "High-Refractive-Index Waveguide Platforms for Chemical and Biosensing", in *Optical Guided-wave Chemical and Biosensors I*, Vol. 7, edited by M. Zourob and A. Lakhtakia (Springer Berlin Heidelberg, Berlin, Heidelberg, 2010), pp. 21–54.

[8] S. Soria, T. Katchalski, E. Teitelbaum, A. A. Friesem, and G. Marowsky, "Enhanced two-photon fluorescence excitation by resonant grating waveguide structures", Optics Letters **29**, 1989–1991 (2004).

[9] Y.-C. Lee, C.-F. Huang, J.-Y. Chang, and M.-L. Wu, "Enhanced light trapping based on guided mode resonance effect for thin-film silicon solar cells with two filling-factor gratings", Optics Express **16**, 7969–7975 (2008).

[10] X. Zhang, Y. Huang, X. Ren, H. Huang, and Q. Wang, "Flat-top steep-edge photodetector with cascaded grating structure", Applied Optics **48**, 6760–6764 (2009).

[11] D. A. Bykov, L. L. Doskolovich, and V. A. Soifer, "On the ability of resonant diffraction gratings to differentiate a pulsed optical signal", Journal of Experimental and Theoretical Physics **114**, 724–730 (2012).

Bibliography

[12] K. J. Lee, R. LaComb, B. Britton, M. Shokooh-Saremi, H. Silva, E. Donkor, Y. Ding, and R. Magnusson, "Silicon-Layer Guided-Mode Resonance Polarizer With 40-nm Bandwidth", IEEE Photonics Technology Letters **20**, 1857–1859 (2008).

[13] R. Magnusson, M. Shokooh-Saremi, and E. G. Johnson, "Guided-mode resonant wave plates", Optics Letters **35**, 2472–2474 (2010).

[14] D. Gallegos, K. D. Long, H. Yu, P. P. Clark, Y. Lin, S. George, P. Nath, and B. T. Cunningham, "Label-free biodetection using a smartphone", Lab on a Chip **13**, 2124–2132 (2013).

[15] K. Y. Lee, J. W. Yoon, S. H. Song, and R. Magnusson, "Multiple *p-n* junction subwavelength gratings for transmission-mode electro-optic modulators", Scientific Reports **7**, srep46508 (2017).

[16] A. N. Enemuo, R. R. Chaudhuri, Y. Song, and S. W. Seo, "Thermo-Optic Sensor Based on Resonance Waveguide Grating for Infrared/Thermal Imaging", IEEE Sensors Journal **15**, 4213–4217 (2015).

[17] S. Giet, C.-L. Lee, S. Calvez, M. D. Dawson, N. Destouches, J.-C. Pommier, and O. Parriaux, "Stabilization of a Semiconductor Disk Laser using an intra-cavity High Reflectivity Grating", Optics Express **15**, 16520–16526 (2007).

[18] K. H. Knop, "Semi-thick transmissive and reflective sinusoidal phase grating structures", US4426130A (Jan. 1984).

[19] Y. Chen, "Nanofabrication by electron beam lithography and its applications: A review", Microelectronic Engineering **135**, 57–72 (2015).

[20] O. Cakmakci and J. Rolland, "Head-worn displays: a review", Journal of Display Technology **2**, 199–216 (2006).

[21] *Surys DID™*, http://surys.com (2017).

[22] J. P. Carmo, R. P. Rocha, M. Bartek, G. de Graaf, R. F. Wolffenbuttel, and J. H. Correia, "A review of visible-range Fabry–Perot microspectrometers in silicon for the industry", Optics & Laser Technology **44**, 2312–2320 (2012).

[23] Y. Chen, R. Halir, Í. Molina-Fernández, P. Cheben, and J.-J. He, "High-efficiency apodized-imaging chip-fiber grating coupler for silicon nitride waveguides", Optics Letters **41**, 5059–5062 (2016).

[24] A. Ricciardi, S. Campopiano, A. Cusano, T. F. Krauss, and L. O'Faolain, "Broadband Mirrors in the Near-Infrared Based on Subwavelength Gratings in SOI", IEEE Photonics Journal **2**, 696–702 (2010).

[25] G. Niederer, H. P. Herzig, J. Shamir, H. Thiele, M. Schnieper, and C. Zschokke, "Tunable, oblique incidence resonant grating filter for telecommunications", Applied optics **43**, 00059, 1683–1694 (2004).

[26] G. Niederer, W. Nakagawa, H. Herzig, and H. Thiele, "Design and characterization of a tunable polarization-independent resonant grating filter", Optics express **13**, 00037, 2196–2200 (2005).

[27] M. Lu, H. Zhai, and R. Magnusson, "Focusing Light with Curved Guided-Mode Resonance Reflectors", Micromachines **2**, 150–156 (2011).

[28] E. A. Bezus, L. L. Doskolovich, and N. L. Kazanskiy, "Evanescent-wave interferometric nanoscale photolithography using guided-mode resonant gratings", Microelectronic Engineering **88**, 170–174 (2011).

[29] A. Saari, G. Genty, M. Siltanen, P. Karvinen, P. Vahimaa, M. Kuittinen, and M. Kauranen, "Giant enhancement of second-harmonic generation in multiple diffraction orders from sub-wavelength resonant waveguide grating", Optics Express **18**, 12298–12303 (2010).

[30] I. S. Maksymov, J. Hutomo, and M. Kostylev, "Transverse magneto-optical Kerr effect in subwavelength dielectric gratings", Optics Express **22**, 8720–8725 (2014).

[31] S.-G. Lee, S.-Y. Jung, H.-S. Kim, S. Lee, and J.-M. Park, "Electromagnetically induced transparency based on guided-mode resonances", Optics Letters **40**, 4241–4244 (2015).

[32] A. Hessel and A. A. Oliner, "A new theory of Wood's anomalies on optical gratings", Applied Optics **4**, 01123, 1275–1297 (1965).

[33] M. Neviere, D. Maystre, and P. Vincent, "Determination of the leaky modes of a corrugated waveguide: application to the study of anomalies of dielectric coated gratings", Journal of Optics **8**, 231–242 (1977).

[34] P. Lalanne, J. P. Hugonin, and P. Chavel, "Optical properties of deep lamellar Gratings: A coupled Bloch-mode insight", Journal of Lightwave Technology **24**, 2442–2449 (2006).

[35] C. J. Chang-Hasnain and W. Yang, "High-contrast gratings for integrated optoelectronics", Advances in Optics and Photonics **4**, 379–440 (2012).

[36] W. Qiao, W. Huang, Y. Liu, X. Li, L.-S. Chen, and J.-X. Tang, "Toward Scalable Flexible Nanomanufacturing for Photonic Structures and Devices", Advanced Materials **28**, 00001, 10353–10380 (2016).

[37] Y. H. Ko and R. Magnusson, "Wideband dielectric metamaterial reflectors: Mie scattering or leaky Bloch mode resonance?", Optica **5**, 289–294 (2018).

[38] Y. Ding and R. Magnusson, "Band gaps and leaky-wave effects in resonant photonic-crystal waveguides", Optics Express **15**, 680–694 (2007).

[39] P. Pottier, L. Shi, and Y.-A. Peter, "Determination of guided-mode resonances in photonic crystal slabs", JOSA B **29**, 109–117 (2012).

[40] K. Knop, "Rigorous diffraction theory for transmission phase gratings with deep rectangular grooves", JOSA **68**, 1206–1210 (1978).

[41] M. L. Dakss, L. Kuhn, P. F. Heidrich, and B. A. Scott, "Grating coupler for efficient excitation of optical guided waves in thin films", Applied Physics Letters **16**, 523–525 (1970).

[42] H. Kogelnik and T. P. Sosnowski, "Holographic Thin Film Couplers", Bell System Technical Journal **49**, 1602–1608 (1970).

[43] H. Kogelnik and C. V. Shank, "Coupled-Wave Theory of Distributed Feedback Lasers", Journal of Applied Physics **43**, 2327–2335 (1972).

[44] S. Wang, "Principles of distributed feedback and distributed Bragg-reflector lasers", IEEE Journal of Quantum Electronics **10**, 413–427 (1974).

[45] D. B. Ostrowsky and A. Jacques, "Formation of optical waveguides in photoresist films", Applied Physics Letters **18**, 556–557 (1971).

[46] M. Neviere, P. Vincent, R. Petit, and M. Cadilhac, "Systematic study of resonances of holographic thin film couplers", Optics Communications **9**, 48–53 (1973).

[47] M. Neviere, P. Vincent, R. Petit, and M. Cadilhac, "Determination of the coupling coefficient of a holographic thin film coupler", Optics Communications **9**, 240–245 (1973).

[48] A. Jacques and D. B. Ostrowsky, "The grating coupler: Comparison of theoretical and experimental results", Optics Communications **13**, 74–77 (1975).

[49] K. Knop and R. Morf, "Diffractive Subtractive Color Filter Responsive to Angle of Incidence of Polychromatic Illuminating Light", WO8300395 (A1) (Feb. 1983), CIB: B42D15/02; B42D15/10; B44F1/12; G02B27/42; G02B27/44; G02B5/18; G03G21/00; G03H1/00; G06K19/16; G06K7/00; G11B23/02; G11B23/40; (IPC1-7): G02B27/44.

[50] V. A. Sychugov and A. V. Tishchenko, "Light emission from a corrugated dielectric waveguide", Soviet Journal of Quantum Electronics **10**, 186 (1980).

[51] V. A. Sychugov and A. V. Tishchenko, "Propagation and conversion of light waves in corrugated waveguide structures", Soviet Journal of Quantum Electronics **12**, 923 (1982).

[52] G. A. Golubenko, A. S. Svakhin, V. A. Sychugov, and A. V. Tishchenko, "Total reflection of light from a corrugated surface of a dielectric waveguide", Soviet Journal of Quantum Electronics **15**, 886 (1985).

[53] I. D. Avrutskii, G. A. Golubenko, V. A. Sychugov, and A. V. Tishchenko, "Light reflection from the surface of a corrugated waveguide", Technical Physics Letters **11**, 971–976 (1985).

[54] L. Mashev and E. Popov, "Diffraction efficiency anomalies of multicoated dielectric gratings", Optics Communications **51**, 131–136 (1984).

[55] L. Mashev and E. Popov, "Zero order anomaly of dielectric coated gratings", Optics Communications **55**, 377–380 (1985).

[56] I. A. Avrutskiı, G. A. Golubenko, V. A. Sychugov, and A. V. Tishchenko, "Spectral and laser characteristics of a mirror with a corrugated waveguide on its surface", Soviet Journal of Quantum Electronics **16**, 1063 (1986).

[57] G. A. Golubenko, A. S. Svakhin, V. A. Sychugov, A. V. Tischenko, E. Popov, and L. Mashev, "Diffraction characteristics of planar corrugated waveguides", Optical and Quantum Electronics **18**, 123–128 (1986).

[58] I. A. Avrutsky and V. A. Sychugov, "Reflection of a Beam of Finite Size from a Corrugated Waveguide", Journal of Modern Optics **36**, 1527–1539 (1989).

[59] T. Tamir, ed., *Integrated Optics*, Vol. 7, Topics in Applied Physics (Springer Berlin Heidelberg, Berlin, Heidelberg, 1975).

[60] R. Petit, ed., *Electromagnetic Theory of Gratings*, Vol. 22, Topics in Current Physics (Springer Berlin Heidelberg, Berlin, Heidelberg, 1980).

[61] D. Rosenblatt, A. Sharon, and A. A. Friesem, "Resonant grating waveguide structures", IEEE Journal of Quantum Electronics **33**, 2038–2059 (1997).

[62] R. Magnusson, Y. Ding, K. J. Lee, D. Shin, P. S. Priambodo, P. P. Young, and T. A. Maldonado, "Photonic devices enabled by waveguide-mode resonance effects in periodically modulated films", in Nano- and Micro-Optics for Information Systems, Vol. 5225 (Oct. 2003), pp. 20–35.

[63] R. Magnusson, M. Shokooh-Saremi, K. J. Lee, J. Curzan, D. Wawro, S. Zimmerman, W. Wu, J. Yoon, H. G. Svavarsson, and S. H. Song, "Leaky-mode resonance photonics: an applications platform", in , edited by E. A. Dobisz and L. A. Eldada, 00000 (Sept. 2011), p. 810202.

[64] R. Magnusson, J. W. Yoon, M. S. Amin, T. Khaleque, and M. J. Uddin, "Extraordinary capabilities of optical devices incorporating guided-mode resonance gratings: application summary and recent examples", in , edited by J. E. Broquin and G. Nunzi Conti, 00000 (Mar. 2014), p. 89880I.

[65] R. Magnusson and Y. H. Ko, "Guided-mode resonance nanophotonics: fundamentals and applications", in , edited by E. M. Campo, E. A. Dobisz, and L. A. Eldada, 00000 (Sept. 2016), p. 992702.

[66] R. Magnusson, M. Niraula, J. W. Yoon, Y. H. Ko, and K. J. Lee, "Guided-mode resonance nanophotonics in materially sparse architectures", in , edited by C. J. Chang-Hasnain, D. Fattal, F. Koyama, and W. Zhou, 00000 (Mar. 2016), p. 975705.

[67] M. A. Cooper, "Optical biosensors: where next and how soon?", Drug Discovery Today **11**, 1061–1067 (2006).

[68] Y. Fang, "Label-Free Cell-Based Assays with Optical Biosensors in Drug Discovery", ASSAY and Drug Development Technologies **4**, 583–595 (2006).

[69] D. Wawro, S. Tibuleac, and R. Magnusson, "Optical Waveguide-mode Resonant Biosensors", in *Optical Imaging Sensors and Systems for Homeland Security Applications*, Advanced Sciences and Technologies for Security Applications (Springer, New York, NY, 2006), pp. 367–384.

[70] I. Abdulhalim, "Biosensing Configurations Using Guided Wave Resonant Structures", in *Optical Waveguide Sensing and Imaging*, NATO Science for Peace and Security Series (Springer, Dordrecht, 2008), pp. 211–228.

[71] K. Erdélyi, A. G. Frutos, J. J. Ramsden, I. Szendro, and G. Voirin, "Grating-Based Optical Biosensors", in *Handbook of Biosensors and Biochips* (John Wiley & Sons, Ltd, 2008).

Bibliography

[72] Y. Fang, A. G. Frutos, and R. Verkleren, "Label-Free Cell-Based Assays for GPCR Screening", Combinatorial Chemistry & High Throughput Screening **11**, 357–369 (2008).

[73] Y. Fang, A. M. Ferrie, and E. Tran, "Resonant Waveguide Grating Biosensor for Whole-Cell GPCR Assays", in *G Protein-Coupled Receptors in Drug Discovery*, Methods in Molecular Biology (Humana Press, Totowa, NJ, 2009), pp. 239–252.

[74] F. Pröll, P. Fechner, and G. Proll, "Direct optical detection in fragment-based screening", Analytical and Bioanalytical Chemistry **393**, 1557–1562 (2009).

[75] H. N. Daghestani and B. W. Day, "Theory and Applications of Surface Plasmon Resonance, Resonant Mirror, Resonant Waveguide Grating, and Dual Polarization Interferometry Biosensors", Sensors **10**, 9630–9646 (2010).

[76] S. Geschwindner, J. F. Carlsson, and W. Knecht, "Application of Optical Biosensors in Small-Molecule Screening Activities", Sensors **12**, 4311–4323 (2012).

[77] R. Halai and M. A. Cooper, "Using label-free screening technology to improve efficiency in drug discovery", Expert Opinion on Drug Discovery **7**, 123–131 (2012).

[78] A. Fernández Gavela, D. Grajales García, J. Ramirez, and L. Lechuga, "Last Advances in Silicon-Based Optical Biosensors", Sensors **16**, 00000, 285 (2016).

[79] M. Paulsen, S. Jahns, and M. Gerken, "Intensity-based readout of resonant-waveguide grating biosensors: Systems and nanostructures", Photonics and Nanostructures - Fundamentals and Applications **26**, 69–79 (2017).

[80] A.-L. Fehrembach, A. Talneau, O. Boyko, F. Lemarchand, and A. Sentenac, "Experimental demonstration of a narrowband, angular tolerant, polarization independent, doubly periodic resonant grating filter", Optics Letters **32**, 2269–2271 (2007).

[81] M. T. Gale, K. Knop, and R. H. Morf, "Zero-order diffractive microstructures for security applications", in Optical Security and Anticounterfeiting Systems, Vol. 1210 (Apr. 1990), pp. 83–90.

[82] S. Tibuleac and R. Magnusson, "Reflection and transmission guided-mode resonance filters", JOSA A **14**, 1617–1626 (1997).

[83] N. Destouches, A. V. Tishchenko, J. C. Pommier, S. Reynaud, O. Parriaux, S. Tonchev, and M. A. Ahmed, "99% efficiency measured in the -1st order of a resonant grating", Optics Express **13**, 3230–3235 (2005).

[84] M. Rumpel, B. Dannecker, A. Voss, M. Moeller, C. Moormann, T. Graf, and M. A. Ahmed, "Thermal behavior of resonant waveguide-grating mirrors in Yb:YAG thin-disk lasers", Optics Letters **38**, 00003, 4766 (2013).

[85] S. Kroker, T. Käsebier, F. Brückner, F. Fuchs, E.-B. Kley, and A. Tünnermann, "Reflective cavity couplers based on resonant waveguide gratings", Optics Express **19**, 16466–16479 (2011).

[86] N. V. Golovastikov, D. A. Bykov, and L. L. Doskolovich, "Resonant diffraction gratings for spatial differentiation of optical beams", Quantum Electronics **44**, 984 (2014).

[87] L. Davoine, V. Paeder, G. Basset, M. Schnieper, and H. P. Herzig, "Resonant absorption of a chemically sensitive layer based on waveguide gratings", Applied optics **52**, 00005, 340–349 (2013).

[88] T. Ning, O. Hyvärinen, H. Pietarinen, T. Kaplas, M. Kauranen, and G. Genty, "Third-harmonic UV generation in silicon nitride nanostructures", Optics Express **21**, 2012–2017 (2013).

[89] S. S. Wang and R. Magnusson, "Theory and applications of guided-mode resonance filters", Applied Optics **32**, 2606–2613 (1993).

[90] P. Lalanne and D. Lemercier-lalanne, "On the effective medium theory of subwavelength periodic structures", Journal of Modern Optics **43**, 2063–2085 (1996).

[91] D. L. Brundrett, E. N. Glytsis, T. K. Gaylord, and J. M. Bendickson, "Effects of modulation strength in guided-mode resonant subwavelength gratings at normal incidence", JOSA A **17**, 1221–1230 (2000).

[92] K. Han and C.-H. Chang, "Numerical Modeling of Sub-Wavelength Anti-Reflective Structures for Solar Module Applications", Nanomaterials **4**, 00000, 87–128 (2014).

[93] F. Träger, ed., *Springer Handbook of Lasers and Optics*, 2nd ed., Springer Handbooks (Springer-Verlag, Berlin Heidelberg, 2012).

[94] R. Brunner, O. Sandfuchs, C. Pacholski, C. Morhard, and J. Spatz, "Lessons from nature: biomimetic subwavelength structures for high-performance optics", Laser & Photonics Reviews **6**, 00037, 641–659 (2012).

[95] D. a. G. Bruggeman, "Berechnung verschiedener physikalischer Konstanten von heterogenen Substanzen. I. Dielektrizitätskonstanten und Leitfähigkeiten der Mischkörper aus isotropen Substanzen", Annalen der Physik **416**, 636–664 (1935).

[96] O. Parriaux, V. A. Sychugov, and A. V. Tishchenko, "Coupling gratings as waveguide functional elements", Pure and Applied Optics: Journal of the European Optical Society Part A **5**, 453–469 (1996).

[97] V. A. Sychugov and A. V. Tishchenko, "Light emission from a corrugated dielectric waveguide", Soviet Journal of Quantum Electronics **10**, 186 (1980).

[98] M. Neviere, E. Popov, R. Reinisch, G. Vitrant, E. Popov, R. Reinisch, and G. Vitrant, *Electromagnetic Resonances in Nonlinear Optics* (CRC Press, Sept. 2000).

[99] V. A. Sychugov, A. V. Tishchenko, M. S. Klimov, and O. Parriaux, "CAD-Tool for Integrated Optic Coupling Gratings", in *Micro System Technologies 90*, edited by H. Reichl (Springer Berlin Heidelberg, 1990), pp. 44–51.

[100] K. Bougot-Robin, W. Wen, and H. Benisty, "Resonant waveguide sensing made robust by on-chip peak tracking through image correlation", Biomedical Optics Express **3**, 2436–2451 (2012).

[101] G. Zheng, L. Zhao, L. Qian, F. Xian, and L. Xu, "Fano resonance and tunability of optical response in double-sided dielectric gratings", Optics Communications **358**, 140–146 (2016).

[102] D. A. Bykov, L. L. Doskolovich, and V. A. Soifer, "Coupled-mode theory and Fano resonances in guided-mode resonant gratings: the conical diffraction mounting", Optics Express **25**, 1151–1164 (2017).

[103] E. Popov, L. Mashev, and D. Maystre, "Theoretical Study of the Anomalies of Coated Dielectric Gratings", Optica Acta: International Journal of Optics **33**, 607–619 (1986).

[104] A.-L. Fehrembach, K. Sharshavina, F. Lemarchand, E. Popov, A. Monmayrant, P. Arguel, and O. Gauthier-Lafaye, "2 × 1D crossed strongly modulated gratings for polarization independent tunable narrowband transmission filters", JOSA A **34**, 234–240 (2017).

[105] M. Niraula, J. W. Yoon, and R. Magnusson, "Mode-coupling mechanisms of resonant transmission filters", Optics Express **22**, 25817–25829 (2014).

[106] M. Niraula, J. W. Yoon, and R. Magnusson, "Concurrent spatial and spectral filtering by resonant nanogratings", Optics Express **23**, 23428 (2015).

[107] C. F. R. Mateus, M. C. Y. Huang, Y. Deng, A. R. Neureuther, and C. J. Chang-Hasnain, "Ultrabroadband mirror using low-index cladded subwavelength grating", IEEE Photonics Technology Letters **16**, 518–520 (2004).

[108] T. Khaleque, M. J. Uddin, and R. Magnusson, "Design and fabrication of broadband guided-mode resonant reflectors in TE polarization", Optics Express **22**, 00000, 12349 (2014).

[109] R. Magnusson, "Wideband reflectors with zero-contrast gratings", Optics Letters **39**, 4337–4340 (2014).

[110] W. Yu, D. Wu, X. Duan, and Y. Yi, "Subwavelength grating wideband reflectors with tapered sidewall profile", MRS Advances **1**, 1683–1691 (2016).

[111] R. Magnusson, "Flat-top resonant reflectors with sharply delimited angular spectra: an application of the Rayleigh anomaly", Optics Letters **38**, 989–991 (2013).

[112] M. Shyiq Amin, J. Woong Yoon, and R. Magnusson, "Optical transmission filters with coexisting guided-mode resonance and Rayleigh anomaly", Applied Physics Letters **103**, 131106 (2013).

[113] D. Maystre, "Theory of Wood's Anomalies", in *Plasmonics: From Basics to Advanced Topics*, edited by S. Enoch and N. Bonod, Springer Series in Optical Sciences (Springer Berlin Heidelberg, Berlin, Heidelberg, 2012), pp. 39–83.

[114] A. T. M. A. Rahman, P. Majewski, and K. Vasilev, "Extraordinary optical transmission: coupling of the Wood–Rayleigh anomaly and the Fabry–Perot resonance", Optics Letters **37**, 1742–1744 (2012).

[115] L. Qian, D. Zhang, C. Tao, R. Hong, and S. Zhuang, "Tunable guided-mode resonant filter with wedged waveguide layer fabricated by masked ion beam etching", Optics Letters **41**, 982–985 (2016).

[116] M.-L. Wu, C.-L. Hsu, Y.-C. Liu, C.-M. Wang, and J.-Y. Chang, "Silicon-based and suspended-membrane-type guided-mode resonance filters with a spectrum-modifying layer design", Optics Letters **31**, 3333–3335 (2006).

[117] Y.-L. Tsai, J.-Y. Chang, M.-L. Wu, Z.-R. Tu, C.-C. Lee, C.-M. Wang, and C.-L. Hsu, "Enhancing the resonance quality factor in membrane-type resonant grating waveguides", Optics Letters **35**, 4199–4201 (2010).

[118] C.-C. Chang, H.-C. Lan, H.-L. Hsiao, J.-W. Jheng, I.-C. Lu, Y.-C. Lee, and M.-L. Wu, "Narrow Bandstop Filters with Wide and Flattened Sidebands Using Silicon-Based and Suspended Membrane Type of Guided-Mode Resonance Structures", Japanese Journal of Applied Physics **49**, 052202 (2010).

[119] N. Matsuyama, Y. Kanamori, J.-S. Ye, and K. Hane, "Micromachined surface emitting dye laser with a self-suspended guided mode resonant grating", Journal of Optics A: Pure and Applied Optics **9**, 940 (2007).

[120] A. T. Cannistra, M. K. Poutous, E. G. Johnson, and T. J. Suleski, "Performance of conformal guided mode resonance filters", Optics Letters **36**, 1155–1157 (2011).

[121] J. Ma, S. Liu, D. Zhang, J. Yao, C. Xu, J. Shao, Y. Jin, and Z. Fan, "Guided-mode resonant grating filter with an antireflective surface for the multiple channels", Journal of Optics A: Pure and Applied Optics **10**, 025302 (2008).

[122] O. Stenzel, S. Wilbrandt, X. Chen, R. Schlegel, L. Coriand, A. Duparré, U. Zeitner, T. Benkenstein, and C. Wächter, "Observation of the waveguide resonance in a periodically patterned high refractive index broadband antireflection coating", Applied Optics **53**, 3147–3156 (2014).

[123] J. P. Kottmann, O. J. F. Martin, D. R. Smith, and S. Schultz, "Plasmon resonances of silver nanowires with a nonregular cross section", Physical Review B **64**, 235402 (2001).

[124] O. Parriaux and G. Voirin, "Plasmon wave versus dielectric waveguiding for surface wave sensing", Sensors and Actuators A: Physical **23**, 00000, 1137–1141 (1990).

[125] T. Siegfried, L. Wang, Y. Ekinci, O. J. Martin, and H. Sigg, "Metal Double Layers with Sub-10 nm Channels", ACS Nano **8**, 3700–3706 (2014).

[126] D. B. Mazulquim, K. J. Lee, J. W. Yoon, L. V. Muniz, B.-H. V. Borges, L. G. Neto, and R. Magnusson, "Efficient band-pass color filters enabled by resonant modes and plasmons near the Rayleigh anomaly", Optics Express **22**, 30843–30851 (2014).

[127] D. Mazulquim, K. J. Lee, L. V. Muniz, B.-H. V. Borges, L. G. Neto, and R. Magnusson, "High Selectivity Plasmonic Color Filter Using a Single Dielectric Film Layer", in Frontiers in Optics 2014 (2014), paper FTh3D.7 (Oct. 2014), FTh3D.7.

[128] I. Koirala, V. R. Shrestha, C.-S. Park, S.-S. Lee, and D.-Y. Choi, "Polarization-Controlled Broad Color Palette Based on an Ultrathin One-Dimensional Resonant Grating Structure", Scientific Reports **7**, srep40073 (2017).

[129] G. Albrecht, M. Ubl, S. Kaiser, H. Giessen, and M. Hentschel, "Comprehensive Study of Plasmonic Materials in the Visible and Near-Infrared: Linear, Refractory, and Nonlinear Optical Properties", ACS Photonics **5**, 1058–1067 (2018).

[130] N. Nguyen-Huu, Y.-L. Lo, and Y.-B. Chen, "Color filters featuring high transmission efficiency and broad bandwidth based on resonant waveguide-metallic grating", Optics Communications **284**, 00025, 2473–2479 (2011).

[131] J. Wang, Q. Fan, S. Zhang, Z. Zhang, H. Zhang, Y. Liang, X. Cao, and T. Xu, "Ultra-thin plasmonic color filters incorporating free-standing resonant membrane waveguides with high transmission efficiency", Applied Physics Letters **110**, 031110 (2017).

[132] H.-T. Chen, A. J. Taylor, and N. Yu, "A review of metasurfaces: physics and applications", Reports on Progress in Physics **79**, 076401 (2016).

[133] Z. Li, M.-H. Kim, C. Wang, Z. Han, S. Shrestha, A. C. Overvig, M. Lu, A. Stein, A. M. Agarwal, M. Lončar, and N. Yu, "Controlling propagation and coupling of waveguide modes using phase-gradient metasurfaces", Nature Nanotechnology **12**, 675–683 (2017).

[134] C.-H. Park, Y.-T. Yoon, V. R. Shrestha, C.-S. Park, S.-S. Lee, and E.-S. Kim, "Electrically tunable color filter based on a polarization-tailored nano-photonic dichroic resonator featuring an asymmetric subwavelength grating", Optics Express **21**, 28783–28793 (2013).

[135] J. Homola, "Present and future of surface plasmon resonance biosensors", Analytical and Bioanalytical Chemistry **377**, 528–539 (2003).

[136] R. Magnusson, J. Yoon, and D. Wawro, "Properties of resonant modal-plasmonic multiparametric biosensors", in , edited by B. L. Miller and P. M. Fauchet (Mar. 2013), 85700K.

[137] F. .-.-C. Chien, C. .-.-Y. Lin, J. .-.-N. Yih, K. .-.-L. Lee, C. .-.-W. Chang, P. .-.-K. Wei, C. .-.-C. Sun, and S. .-.-J. Chen, "Coupled waveguide–surface plasmon resonance biosensor with subwavelength grating", Biosensors and Bioelectronics **22**, 2737–2742 (2007).

[138] P. Zeng, J. Cadusch, D. Chakraborty, T. A. Smith, A. Roberts, J. E. Sader, T. J. Davis, and D. E. Gómez, "Photoinduced Electron Transfer in the Strong Coupling Regime: Waveguide–Plasmon Polaritons", Nano Letters **16**, 00000, 2651–2656 (2016).

[139] W. L. Barnes, A. Dereux, and T. W. Ebbesen, "Surface plasmon subwavelength optics", Nature **424**, 824–830 (2003).

[140] F. López-Tejeira, S. G. Rodrigo, L. Martín-Moreno, F. J. García-Vidal, E. Devaux, T. W. Ebbesen, J. R. Krenn, I. P. Radko, S. I. Bozhevolnyi, M. U. González, J. C. Weeber, and A. Dereux, "Efficient unidirectional nanoslit couplers for surface plasmons", Nature Physics **3**, 324 (2007).

[141] E. Devaux, T. W. Ebbesen, J.-C. Weeber, and A. Dereux, "Launching and decoupling surface plasmons via micro-gratings", Applied Physics Letters **83**, 4936–4938 (2003).

[142] Y. Ohtera, S. Iijima, and H. Yamada, "Guided-mode resonance in curved grating structures", Optics Letters **36**, 1689–1691 (2011).

[143] P. K. Tien, "Method of forming novel curved-line gratings and their use as reflectors and resonators in integrated optics", Optics Letters **1**, 64–66 (1977).

[144] D. Heitmann and C. Ortiz, "Calculation and experimental verification of two-dimensional focusing grating couplers", IEEE Journal of Quantum Electronics **17**, 1257–1263 (1981).

[145] S. Nishiwaki, J.-i. Asada, and S. Uchida, "Optical head employing a concentric-circular focusing grating coupler", Applied Optics **33**, 1819–1827 (1994).

[146] K. Kintaka, J. Nishii, Y. Imaoka, J. Ohmori, S. Ura, R. Satoh, and H. Nishihara, "A guided-mode-selective focusing grating coupler", IEEE Photonics Technology Letters **16**, 512–514 (2004).

[147] K. Kintaka, J. Nishii, J. Ohmori, Y. Imaoka, M. Nishihara, S. Ura, R. Satoh, and H. Nishihara, "Integrated waveguide gratings for wavelength-demultiplexing of free space waves from guided waves", Optics Express **12**, 3072–3078 (2004).

[148] K. Hatanaka, T. Majima, K. Kintaka, J. Inoue, K. Nishio, Y. Awatsuji, and S. Ura, "Cavity-resonator-integrated guided-mode resonance filter consisting of curved gratings", Electronics Letters **48**, 717–718 (2012).

[149] M. Rumpel, M. Haefner, T. Schoder, C. Pruss, A. Voss, W. Osten, M. A. Ahmed, and T. Graf, "Circular grating waveguide structures for intracavity generation of azimuthal polarization in a thin-disk laser", Optics Letters **37**, 1763–1765 (2012).

[150] C. D. Bruzewicz, J. M. Sage, J. Chiaverini, K. K. Mehta, R. J. Ram, and R. McConnell, "Integrated optical addressing of an ion qubit", Nature Nanotechnology **11**, 1066 (2016).

[151] K. K. Mehta and R. J. Ram, "Precise and diffraction-limited waveguide-to-free-space focusing gratings", Scientific Reports **7**, 2019 (2017).

[152] W. Wang, Q. Liu, G. Zhu, X. Li, S. He, T. Sa, X. Gao, and Y. Wang, "Polarization-Insensitive Concentric Circular Grating Filters Featuring a Couple of Resonant Peaks", IEEE Photonics Journal **7**, 1–10 (2015).

[153] C. J. Oton, "Long-Working-Distance Grating Coupler for Integrated Optical Devices", IEEE Photonics Journal **8**, 1–8 (2016).

[154] Y. Ohtera, S. Iijima, and H. Yamada, "Cylindrical Resonator Utilizing a Curved Resonant Grating as a Cavity Wall", Micromachines **3**, 101–113 (2012).

[155] Y. Ohtera, H. Hirose, and H. Yamada, "Characteristics of Resonantly-Guided Modes in Microstructured Optical Fibers", Photonics **1**, 432–441 (2014).

[156] D. Fattal, J. Li, Z. Peng, M. Fiorentino, and R. G. Beausoleil, "Flat dielectric grating reflectors with focusing abilities", Nature Photonics **4**, 466–470 (2010).

[157] L. Chrostowski, "Optical gratings: Nano-engineered lenses", Nature Photonics **4**, 413–415 (2010).

[158] X. Duan, M. Zhang, Y. Huang, K. Liu, Y. Shang, and X. Ren, "Polarization-Independent Focusing Reflectors Using Two-Dimensional SWG", IEEE Photonics Technology Letters **29**, 209–212 (2017).

[159] R. L. Renesse, *Optical Document Security, Third Edition*, 3rd edition (Artech House, Boston, Mass., Dec. 2004).

[160] M.-L. Wu, C.-L. Hsu, H.-C. Lan, H.-I. Huang, Y.-C. Liu, Z.-R. Tu, C.-C. Lee, J.-S. Lin, C.-C. Su, and J.-Y. Chang, "Authentication labels based on guided-mode resonant filters", Optics Letters **32**, 1614–1616 (2007).

[161] H.-A. Lin and C.-S. Huang, "Linear variable filter based on a gradient grating period guided-mode resonance filter", IEEE Photonics Technology Letters, 00000, 1–1 (2016).

[162] K. Chaganti, I. Salakhutdinov, I. Avrutsky, and G. W. Auner, "A simple miniature optical spectrometer with a planar waveguide grating coupler in combination with a plano-convex lens", Optics Express **14**, 4064–4072 (2006).

[163] I. Avrutsky, K. Chaganti, I. Salakhutdinov, and G. Auner, "Concept of a miniature optical spectrometer using integrated optical and micro-optical components", Applied Optics **45**, 7811–7817 (2006).

[164] M. Ramuz, L. Bürgi, R. Stanley, and C. Winnewisser, "Coupling light from an organic light emitting diode (OLED) into a single-mode waveguide: Toward monolithically integrated optical sensors", Journal of Applied Physics **105**, 084508 (2009).

[165] M. Ramuz, D. Leuenberger, and L. Bürgi, "Optical biosensors based on integrated polymer light source and polymer photodiode", Journal of Polymer Science Part B: Polymer Physics **49**, 80–87 (2010).

[166] N. Ganesh, A. Xiang, N. B. Beltran, D. W. Dobbs, and B. T. Cunningham, "Compact wavelength detection system incorporating a guided-mode resonance filter", Applied Physics Letters **90**, 081103 (2007).

[167] H.-A. Lin, H.-Y. Hsu, C.-W. Chang, and C.-S. Huang, "Compact spectrometer system based on a gradient grating period guided-mode resonance filter", Optics Express **24**, 00001, 10972 (2016).

[168] R. Bhargava, "Infrared Spectroscopic Imaging: The Next Generation", Applied Spectroscopy **66**, 1091–1120 (2012).

[169] A. K. Kodali, M. Schulmerich, J. Ip, G. Yen, B. T. Cunningham, and R. Bhargava, "Narrowband Midinfrared Reflectance Filters Using Guided Mode Resonance", Analytical Chemistry **82**, 5697–5706 (2010).

[170] J.-N. Liu, M. V. Schulmerich, R. Bhargava, and B. T. Cunningham, "Optimally designed narrowband guided-mode resonance reflectance filters for mid-infrared spectroscopy", Optics Express **19**, 24182–24197 (2011).

[171] A. L. Fannin, J. W. Yoon, B. R. Wenner, J. W. Allen, M. S. Allen, and R. Magnusson, "Experimental Evidence for Coherent Perfect Absorption in Guided-Mode Resonant Silicon Films", IEEE Photonics Journal **8**, 1–7 (2016).

[172] Y. Horie, A. Arbabi, S. Han, and A. Faraon, "High resolution on-chip optical filter array based on double subwavelength grating reflectors", Optics Express **23**, 29848–29854 (2015).

[173] A. M. Ferrie, Q. Wu, and Y. Fang, "Resonant waveguide grating imager for live cell sensing", Applied Physics Letters **97**, 223704 (2010).

[174] P. G. Hermannsson, C. Vannahme, C. L. C. Smith, and A. Kristensen, "Absolute analytical prediction of photonic crystal guided mode resonance wavelengths", Applied Physics Letters **105**, 071103 (2014).

[175] L. U. Kempen and R. E. Kunz, "Replicated Mach-Zehnder interferometers with focusing grating couplers for sensing applications", Sensors and Actuators B: Chemical **39**, 00029, 295–299 (1997).

[176] P. K. Sahoo, S. Sarkar, and J. Joseph, "High sensitivity guided-mode-resonance optical sensor employing phase detection", Scientific Reports **7**, 7607 (2017).

[177] M. A. Cooper, "Optical biosensors in drug discovery", Nature Reviews Drug Discovery **1**, nrd838 (2002).

[178] Y. Fang, J. Fang, E. Tran, X. Xie, M. Hallstrom, and A. G. Frutos, "High-throughput analysis of biomolecular interactions and cellular responses with resonant waveguide grating biosensors", in *Label-Free Biosensors*, edited by M. A. Cooper (Cambridge University Press, Cambridge, 2009), pp. 206–222.

[179] G. Quaranta, G. Basset, O. J. F. Martin, and B. Gallinet, "Color-Selective and Versatile Light Steering with up-Scalable Subwavelength Planar Optics", ACS Photonics **4**, 1060–1066 (2017).

[180] G. Quaranta, G. Basset, Z. Benes, O. J. F. Martin, and B. Gallinet, "Light refocusing with up-scalable resonant waveguide gratings in confocal prolate spheroid arrangements", Journal of Nanophotonics **12**, 016004 (2018).

[181] G. Quaranta, G. Basset, O. J. F. Martin, and B. Gallinet, "Steering and filtering white light with resonant waveguide gratings", Proc. of the SPIE **10354**, 1035408 (2017).

[182] A. Taflove and S. C. Hagness, *Computational Electrodynamics: The Finite-difference Time-domain Method* (Artech House, 2005).

[183] D. J. Klotzkin, *Introduction to Semiconductor Lasers for Optical Communications: An Applied Approach* (Springer-Verlag, New York, 2014).

[184] B. Liang, M. Bai, H. Ma, N. Ou, and J. Miao, "Wideband Analysis of Periodic Structures at Oblique Incidence by Material Independent FDTD Algorithm", IEEE Transactions on Antennas and Propagation **62**, 354–360 (2014).

[185] J.-P. Bérenger, "Perfectly Matched Layer (PML) for Computational Electromagnetics", Synthesis Lectures on Computational Electromagnetics **2**, 1–117 (2007).

[186] J. Jin, *The Finite Element Method in Electromagnetics*, 3rd (Wiley-IEEE Press, 2014).

[187] M. V. Shuba and A. Lakhtakia, "Splitting of absorptance peaks in absorbing multilayer backed by a periodically corrugated metallic reflector", JOSA A **33**, 779–784 (2016).

[188] B. Liang, M. Bai, H. Ma, N. Ou, and J. Miao, "Wideband Analysis of Periodic Structures at Oblique Incidence by Material Independent FDTD Algorithm", IEEE Transactions on Antennas and Propagation **62**, 354–360 (2014).

[189]   L. D. Landau, J. S. Bell, M. J. Kearsley, L. P. Pitaevskii, E. M. Lifshitz, and J. B. Sykes, *Electrodynamics of Continuous Media* (Elsevier, Oct. 2013).

[190]   S. Tokumaru, "Energy flux densities of electromagnetic waves", Electronics and Communications in Japan (Part I: Communications) **74**, 82–88 (1991).

[191]   H. P. Herzig, *Micro-Optics: Elements, Systems And Applications* (CRC Press, Apr. 1997).

[192]   M. J. Madou, *Manufacturing Techniques for Microfabrication and Nanotechnology* (CRC Press, June 2011).

[193]   K. J. Gåsvik, *Optical Metrology* (John Wiley & Sons, Apr. 2003).

[194]   T. Yoshizawa, *Handbook of Optical Metrology: Principles and Applications* (CRC Press, Feb. 2009).

[195]   A. J. Wolf, H. Hauser, V. Kübler, C. Walk, O. Höhn, and B. Bläsi, "Origination of nano- and microstructures on large areas by interference lithography", Microelectronic Engineering, Special Issue MNE 2011 - Part II **98**, 293–296 (2012).

[196]   C. Lu and R. Lipson, "Interference lithography: a powerful tool for fabricating periodic structures", Laser & Photonics Reviews **4**, 568–580 (2010).

[197]   H. H. Solak, C. David, J. Gobrecht, V. Golovkina, F. Cerrina, S. O. Kim, and P. F. Nealey, "Sub-50 nm period patterns with EUV interference lithography", Microelectronic Engineering, Proceedings of the 28th International Conference on Micro- and Nano-Engineering **67-68**, 56–62 (2003).

[198]   C. Vieu, F. Carcenac, A. Pépin, Y. Chen, M. Mejias, A. Lebib, L. Manin-Ferlazzo, L. Couraud, and H. Launois, "Electron beam lithography: resolution limits and applications", Applied Surface Science, Surface Science in Micro & Nanotechnology **164**, 111–117 (2000).

[199]   M. Paulsen, L. T. Neustock, S. Jahns, J. Adam, and M. Gerken, "Simulation methods for multiperiodic and aperiodic nanostructured dielectric waveguides", Optical and Quantum Electronics **49**, 00000 (2017) 10.1007/s11082-017-0918-6.

[200]   N. Eriksson, M. Hagberg, and A. Larsson, "Electron beam defined surface gratings in AlGaAs with precisely controlled duty cycle using a multiple line exposure technique", Journal of Vacuum Science & Technology B: Microelectronics and Nanometer Structures Processing, Measurement, and Phenomena **14**, 184–186 (1996).

[201]   W. (Hu, K. Sarveswaran, M. Lieberman, and G. H. Bernstein, "Sub-10 nm electron beam lithography using cold development of poly(methylmethacrylate)", Journal of Vacuum Science & Technology B: Microelectronics and Nanometer Structures Processing, Measurement, and Phenomena **22**, 1711–1716 (2004).

[202]   A. E. Grigorescu and C. W. Hagen, "Resists for sub-20-nm electron beam lithography with a focus on HSQ: state of the art", Nanotechnology **20**, 292001 (2009).

[203]   A. Talneau, F. Lemarchand, A.-L. Fehrembach, and A. Sentenac, "Impact of electron-beam lithography irregularities across millimeter-scale resonant grating filter performances", Applied Optics **49**, 658–662 (2010).

[204]   K. Li, J. Li, C. Reardon, C. S. Schuster, Y. Wang, G. J. Triggs, N. Damnik, J. Müenchen-berger, X. Wang, E. R. Martins, and T. F. Krauss, "High speed e-beam writing for large area photonic nanostructures — a choice of parameters", Scientific Reports **6**, srep32945 (2016).

[205]   H. O. Pierson, *Handbook of Chemical Vapor Deposition: Principles, Technology and Applications* (William Andrew, Sept. 1999).

[206]   "Physical Vapor Deposition", in *The Materials Science of Semiconductors*, edited by A. Rockett (Springer US, Boston, MA, 2008), pp. 505–572.

[207]   R. F. Bunshah and C. V. Deshpandey, "Plasma assisted physical vapor deposition processes: A review", Journal of Vacuum Science & Technology A **3**, 553–560 (1985).

[208]   M. R. Saleem, R. Ali, M. B. Khan, S. Honkanen, and J. Turunen, "Impact of Atomic Layer Deposition to Nanophotonic Structures and Devices", Frontiers in Materials **1** (2014) 10.3389/fmats.2014.00018.

[209]   P. J. Kelly and R. D. Arnell, "Magnetron sputtering: a review of recent developments and applications", Vacuum **56**, 159–172 (2000).

[210]   D. W. Dobbs, I. Gershkovich, and B. T. Cunningham, "Fabrication of a graded-wavelength guided-mode resonance filter photonic crystal", Applied Physics Letters **89**, 123113 (2006).

[211]   Y. Nazirizadeh, F. von Oertzen, T. Karrock, J. Greve, and M. Gerken, "Enhanced sensitivity of photonic crystal slab transducers by oblique-angle layer deposition", Optics Express **21**, 18661–18670 (2013).

[212]   R. C. Rumpf and E. G. Johnson, "Modeling fabrication to accurately place GMR resonances", Optics Express **15**, 3452–3464 (2007).

[213]   S. Y. Chou, P. R. Krauss, and P. J. Renstrom, "Imprint of sub-25 nm vias and trenches in polymers", Applied Physics Letters **67**, 3114–3116 (1995).

[214]   H. Schift, P. Urwyler, P. M. Kristiansen, and J. Gobrecht, "Nanoimprint lithography process chains for the fabrication of micro- and nanodevices", Journal of Micro/Nano-lithography, MEMS, and MOEMS **13**, 031303 (2014).

[215]   M. T. Gale, "Replication techniques for diffractive optical elements", Microelectronic Engineering **34**, 321–339 (1997).

[216]   P. Reader-Harris, A. Ricciardi, T. Krauss, and A. D. Falco, "Optical guided mode resonance filter on a flexible substrate", Optics Express **21**, 1002–1007 (2013).

[217]   V. K. Parashar, A. Sayah, M. Pfeffer, F. Schoch, J. Gobrecht, and M. A. M. Gijs, "Nano-replication of diffractive optical elements in sol–gel derived glasses", Microelectronic Engineering, Proceedings of the 28th International Conference on Micro- and Nano-Engineering **67-68**, 710–719 (2003).

[218]   K. J. Lee, J. Jin, B.-S. Bae, and R. Magnusson, "Optical filters fabricated in hybrimer media with soft lithography", Optics Letters **34**, 2510–2512 (2009).

Bibliography

[219] L. Peng, Y. Deng, P. Yi, and X. Lai, "Micro hot embossing of thermoplastic polymers: a review", Journal of Micromechanics and Microengineering **24**, 013001 (2013).

[220] Y. Nazirizadeh, F. von Oertzen, K. Plewa, N. Barié, P.-J. Jakobs, M. Guttmann, H. Leiste, and M. Gerken, "Sensitivity optimization of injection-molded photonic crystal slabs for biosensing applications", Optical Materials Express **3**, 556–565 (2013).

[221] M. D. Fagan, B. H. Kim, and D. Yao, "A novel process for continuous thermal embossing of large-area nanopatterns onto polymer films", Advances in Polymer Technology **28**, 246–256 (2009).

[222] T. Khaleque, H. G. Svavarsson, and R. Magnusson, "Fabrication of resonant patterns using thermal nano-imprint lithography for thin-film photovoltaic applications", Optics Express **21**, A631 (2013).

[223] L. Liu, J. Zhang, M. A. Badshah, L. Dong, J. Li, S.-m. Kim, and M. Lu, "A programmable nanoreplica molding for the fabrication of nanophotonic devices", Scientific Reports **6**, srep22445 (2016).

[224] M. Qian, W. Zhang, D. Trefilov, M. Ji, Y. Cui, C. Yuan, W. Li, H. Ge, and Y. Chen, "Tuning the period of nanogratings using mechanical stretching and nanoimprint lithography", Applied Physics A **122**, 577 (2016).

[225] W.-K. Kuo and Y.-M. Chang, "Implementation of a narrowband guided-mode resonance optical filter using the multiple-mold replica method in the nanoimprinting process", Applied Optics **56**, 99–104 (2017).

[226] Y. Huang, L. Liu, M. Johnson, A. C Hillier, and M. Lu, "One-step sol–gel imprint lithography for guided-mode resonance structures", Nanotechnology **27**, 00000, 095302 (2016).

[227] T. Iwayanagi, T. Ueno, S. Nonogaki, H. Ito, and C. G. Willson, "Materials and Processes for Deep-UV Lithography", in *Electronic and Photonic Applications of Polymers*, Vol. 218, Advances in Chemistry 218 (American Chemical Society, Oct. 1988), pp. 109–224.

[228] S. Ogata, M. Tada, and M. Yoneda, "Electron-beam writing system and its application to large and high-density diffractive optic elements", Applied Optics **33**, 2032–2038 (1994).

[229] *WieWeb software – The makers of CleWin.*

[230] U. GRIESMANN, *Octave and MATLAB toolbox for GDSII stream format. Contribute to ulfgri/gdsii-toolbox development by creating an account on GitHub*, https://github.com/ulfgri/gdsii-toolbox, Sept. 2018.

[231] *The GDSII Stream Format.*

[232] *CMI - Center of MicroNanoTechnology*, https://cmi.epfl.ch/ebeam/Electron_beam_lithography_tool.php.

[233] *JEOL JBX-6300FS E-Beam Lithography at the Washington Nanofabrication Facility.*

[234] J. Trasobares, F. Vaurette, M. François, H. Romijn, J.-L. Codron, D. Vuillaume, D. Théron, and N. Clément, "High speed e-beam lithography for gold nanoarray fabrication and use in nanotechnology", Beilstein Journal of Nanotechnology **5**, 1918–1925 (2014).

[235] *GeniSys GmbH - Beamer.*

[236] R. Fallica, D. Kazazis, R. Kirchner, A. Voigt, I. Mochi, H. Schift, and Y. Ekinci, "Lithographic performance of ZEP520A and mr-PosEBR resists exposed by electron beam and extreme ultraviolet lithography", Journal of Vacuum Science & Technology B **35**, 061603 (2017).

[237] E. Platzgummer, C. Klein, and H. Loeschner, "Electron multibeam technology for mask and wafer writing at 0.1 nm address grid", Journal of Micro/Nanolithography, MEMS, and MOEMS **12**, 031108 (2013).

[238] S. Okazaki, "High resolution optical lithography or high throughput electron beam lithography: The technical struggle from the micro to the nano-fabrication evolution", Microelectronic Engineering **133**, 23–35 (2015).

[239] B. Wu and A. Kumar, "Extreme ultraviolet lithography: A review", Journal of Vacuum Science & Technology B: Microelectronics and Nanometer Structures Processing, Measurement, and Phenomena **25**, 1743–1761 (2007).

[240] D. M. Pozar, *Microwave Engineering, 4th Edition* (Wiley, Nov. 2011).

[241] R. R. Boye and R. K. Kostuk, "Investigation of the effect of finite grating size on the performance of guided-mode resonance filters", Applied Optics **39**, 3649–3653 (2000).

[242] K. Okamoto, *Fundamentals of Optical Waveguides* (Academic Press, 2006).

[243] M. Debenham, "Refractive indices of zinc sulfide in the 0.405–13-Mm wavelength range", Applied optics **23**, 00046, 2238–2239 (1984).

[244] *OrmoComp® | micro resist technology GmbH*, http://www.microresist.de/en/products/hybrid-polymers/uv-imprint-uv-moulding/ormocomp%C2%AE.

[245] C. A. Palmer and E. G. Loewen, *Diffraction grating handbook*, 00226 (Newport Corporation Springfield, Ohio, USA, 2005).

[246] A. M. Prokhorov, A. A. Spikhal'skiı, and V. A. Sychugov, "Emission of E and H waves from a corrugated section of a diffused waveguide", Soviet Journal of Quantum Electronics **6**, 1211 (1976).

[247] A. A. Zlenko, A. M. Prokhorov, A. A. Spikhal'skiı, and V. A. Sychugov, "Emission of E waves from a corrugated section of a waveguide", Soviet Journal of Quantum Electronics **6**, 00003, 565 (1976).

[248] M. S. Scholl, "Recursive exact ray trace equations through the foci of the tilted off-axis confocal prolate spheroids", Journal of Modern Optics **43**, 1583–1588 (1996).

[249] G. Quaranta and G. Basset, "Optical security device", EP3205512 (June 2018).

[250] L. Davoine and G. Basset, "Guided Mode Resonance Device", EP3087421 ().

Bibliography

[251] G. Basset and G. Quaranta, "Optical Combiner And Applications Thereof", WO2016EP82041 ().

[252] B. E. A. Saleh and M. C. Teich, *Fundamentals of Photonics*, edited by J. W. Goodman, Wiley Series in Pure and Applied Optics (John Wiley & Sons, Inc., New York, USA, Aug. 1991).

[253] R. G. Hunsperger, *Integrated Optics*, 00025 (Springer New York, New York, NY, 2009).

[254] "Chapter 5 Characterization of thin films by prism coupling of leaky modes", in *Thin Films and Nanostructures*, Vol. 33, edited by A. V. Khomchenko, Waveguide Spectroscopy of Thin Films (Academic Press, Jan. 2005), pp. 97–112.

[255] N. Destouches, D. Blanc, J. Franc, S. Tonchev, N. Hendrickx, P. V. Daele, and O. Parriaux, "Efficient and tolerant resonant grating coupler for multimode optical interconnections", Optics Express **15**, 16870–16879 (2007).

[256] C. Yan, K.-Y. Yang, and O. J. F. Martin, "Fano-resonance-assisted metasurface for color routing", Light: Science & Applications **6**, e17017 (2017).

[257] M. Faraji-Dana, E. Arbabi, A. Arbabi, S. M. Kamali, H. Kwon, and A. Faraon, "Compact folded metasurface spectrometer", Nature Communications **9**, 4196 (2018).

[258] J. J. Burke, G. I. Stegeman, and T. Tamir, "Surface-polariton-like waves guided by thin, lossy metal films", Physical Review B **33**, 5186–5201 (1986).

[259] D. G. Sannikov and D. I. Sementsov, "The surface mode of a dielectric waveguide with metal substrate", Technical Physics Letters **29**, 353–356 (2003).

[260] I. H. Malitson, "Interspecimen Comparison of the Refractive Index of Fused Silica", JOSA **55**, 1205–1209 (1965).

[261] H. U. Yang, J. D'Archangel, M. L. Sundheimer, E. Tucker, G. D. Boreman, and M. B. Raschke, "Optical dielectric function of silver", Physical Review B **91**, 235137 (2015).

[262] P. Berini, "Long-range surface plasmon polaritons", Advances in Optics and Photonics **1**, 484–588 (2009).

[263] H. Raether, "Surface plasmons on smooth surfaces", in *Surface Plasmons on Smooth and Rough Surfaces and on Gratings*, edited by H. Raether, Springer Tracts in Modern Physics (Springer Berlin Heidelberg, Berlin, Heidelberg, 1988), pp. 4–39.

[264] I. R. Hooper and J. R. Sambles, "Surface plasmon polaritons on thin-slab metal gratings", Physical Review B **67**, 235404 (2003).

[265] B. Gallinet and O. J. F. Martin, "Ab initio theory of Fano resonances in plasmonic nanostructures and metamaterials", Physical Review B **83**, 235427 (2011).

[266] B. Gallinet and O. J. F. Martin, "Influence of Electromagnetic Interactions on the Line Shape of Plasmonic Fano Resonances", ACS Nano **5**, 8999–9008 (2011).

[267] B. Gallinet, T. Siegfried, H. Sigg, P. Nordlander, and O. J. F. Martin, "Plasmonic Radiance: Probing Structure at the Ångström Scale with Visible Light", Nano Letters **13**, 497–503 (2013).

124

[268] D. F. Swinehart, "The Beer-Lambert Law", Journal of Chemical Education **39**, 333 (1962).

[269] N. Fang, Z. Liu, T.-J. Yen, and X. Zhang, "Regenerating evanescent waves from a silver superlens", Optics Express **11**, 682–687 (2003).

[270] A. Giannattasio, I. R. Hooper, and W. L. Barnes, "Transmission of light through thin silver films via surface plasmon-polaritons", Optics Express **12**, 5881–5886 (2004).

[271] F. Lütolf, O. J. F. Martin, and B. Gallinet, "Fano-resonant aluminum and gold nanostructures created with a tunable, up-scalable process", Nanoscale **7**, 18179–18187 (2015).

[272] W. Chen, L. Guo, and Z. Sun, "Resonant Absorption of TE-Polarized Light at the Surface of a Dielectric-Coated Metal Grating", IEEE Photonics Journal **6**, 1–6 (2014).

[273] S. A. Maier, *Plasmonics: fundamentals and applications*, 06022 (Springer, New York, 2007).

Giorgio Quaranta

13 Rue du Rhin, 68300 Saint Louis, France

+41779553413

giorgio.quaranta@protonmail.com

linkedin.com/in/giorgioquaranta

researchgate.net/profile/Giorgio_Quaranta

giorgio.quaranta_1

Objective: to contribute my expertise in diffraction gratings and waveguides by means of analytical and numerical modeling, algorithm development, upscalable fabrications, characterizations, with my hands-on, team-working, project management and problem-solver skills.

CORE EXPERIENCE

Doctoral Thesis in Color-Selective Diffraction for Industrial Applications
Swiss Center for Electronics and Microtechnology, Switzerland
Swiss Federal Institute of Technology in Lausanne, Switzerland

NOV 2015 – PRESENT

Research and development of arrays of resonant waveguide gratings to achieve color-selective diffraction and light-refocusing in a readily high-volume, up-scalable process. Realization of demonstrators for optical document security, optical combiners for near-eye displays, and multispectral imaging. Development of analytical models and numerical simulations. Optimization of electron beam lithography for large area fabrications.

Engineering project support for several internal R&D and industrial projects, being also the principal investigator of some of them, in thin film optics, diffractive optics, nanophotonics, micro-optics. Presentation of demonstrators to customers. Provided training to engineers and supervised students. Contribution in writing patent applications and invention reports. Responsible for the electron beam lithography.

EDUCATION

Ph.D. in Photonics
Swiss Center for Electronics and Microtechnology, Switzerland
Swiss Federal Institute of Technology in Lausanne, Switzerland

NOV 2015 – PRESENT

International M.Sc. in Micro & Nano Technologies for ICTs
(Laurea Magistrale and Diplôme d'Ingenieur)
Swiss Center for Electronics and Microtechnology, Switzerland
Swiss Federal Institute of Technology in Lausanne, Switzerland
Grenoble Institute of Technology, France
Polytechnic University of Turin, Italy

SEPT 2013 – SEPT 2015

B.Sc. in Physical Engineering
Polytechnic University of Turin, Italy

SEPT 2010 – SEPT 2013

PATENTS and PATENT APPLICATIONS

G. Quaranta and G. Basset, "Optical security device", EP3205512 (B1).

G. Basset and G. Quaranta, "Optical Combiner and Applications Thereof", EP3414617 (A1).

CSEM: 2 other patent applications in 2017 - 2018. Can not disclose at this time.

SKILLS

Cleanroom Facilities	Cleanrooms ISO-9001, electron beam lithography, UV nanoimprint lithography, AFM, SEM.
Optical Skills	Optical simulators (RCWA, FDTD, FETD, SIE), optical metrology, nanophotonic theory, DOE, resonant waveguide gratings, diffraction gratings, near-eye displays, plasmonic, metasurfaces.
IT Skills	Matlab, Lumerical, OmniSim, Latex, Blender, data analysis.
IP Skills	Courses on IPs and patents, contributed to write patent applications and invention reports.
Soft Skills	Problem solving, presentation skills, project management, results oriented, challenge driven.

ADDITIONAL EXPERIENCE

Team Member for 2018 Hyperloop SpaceX Competition (3rd position)
Swiss Federal Institute of Technology in Lausanne, Switzerland
SEPT 2017 – JUL 2018

Master Thesis in Optimization of Waveguide Gratings for Optical Security
Swiss Center for Electronics and Microtechnology, Switzerland
MAR 2015 – AUG 2015

Internship in Near-Field Optical Simulations in a RCWA Matlab Platform
Swiss Center for Electronics and Microtechnology, Switzerland
JUN 2014 – AUG 2014

University Project in Head Up Display (HUD) for Dangerous Environments
Grenoble Institute of Technology, France
FEB 2014 – MAY 2014

LANGUAGES

English	Fluent	**Italian**	Native
German	Elementary	**French**	Elementary

EXTRA-CURRICULAR ACTIVITIES

Personal Achievements	School-leaving certificate in Music Theory and "Solfeggio" First Aid Course (Red Cross)
Hobbies	Swimming Playing guitar (acoustic and classic guitar)
Other Experiences	1 month of au pair experience in a British family (gardening, babysitting, house maintenance) 6 years of volunteer experience as teacher of guitar and solfeggio at a recreation center

PUBLICATIONS

Peer-reviewed Publications:

- G. Quaranta, G. Basset, O. J. F. Martin, and B. Gallinet, "Color-Selective and Versatile Light Steering withup-Scalable Subwavelength Planar Optics", ACS Photonics 4(5), 1060–1066 (2017).

- G. Quaranta, G. Basset, Z. Benes, O. J. F. Martin, and B. Gallinet, "Light refocusing with up-scalable resonant waveguide gratings in confocal prolate spheroid arrangements", JNP, JNOACQ 12(1), 016004 (2018).

- G. Quaranta, G. Basset, O. J. F. Martin, and B. Gallinet, "Recent Advances in Resonant Waveguide Gratings", Laser & Photonics Reviews 12(9), 1800017 (2018).

- S. Perrin, H. Li, K. Badu, T. Comparon, G. Quaranta, N. Messaddeq, N. Lemercier, P. Montgomery, J. L. Vonesch, and S. Lecler, "Transmission Microsphere-Assisted Dark-Field Microscopy", physica status solidi RRL, (2018).

Conference Proceedings and Technical Reports:

- G. Basset, G. Quaranta, F. Lütolf, L. Davoine, and M. Schnieper, "Subwavelength gratings for OVDs-From local interactions to using light-transport", arXiv preprint arXiv:1511.05543 (2015).

- G. Quaranta, G. Basset, O. J. F. Martin, and B. Gallinet, "Steering and filtering white light with resonant waveguide gratings", in (SPIE, 2017), 10354, p. 1035408.

- G. Quaranta, F. Geister, F. Lütolf, L. Dümperlmann, M. Stalder, B. Gallinet, and R. Ferrini, "Nanostructured Thin Films for Spectroscopy and Imaging", in (CSEM Scientific and Technical Report, 2017), p. 49.

- G. Quaranta, G. Basset, Z. Benes, O. J. F. Martin, and B. Gallinet, "Large Area Fabrication of Patterns of Resonant Waveguide Gratings by Electron Beam Lithography for Up-scalable Applications", in (PIERS, 2018), p.323.

- G. Quaranta, G. Basset, B. Gallinet, and M. Schnieper, "Smartphone-based authentication with a new color-selective DOVID", in (ODS Proceedings, 2018), p. 162-168.

Basel, Switzerland – April 2019 (v27)